

INFORMATION TO USERS

This manuscript has been reproduced from the microfilm master. UMI films the text directly from the original or copy submitted. Thus, some thesis and dissertation copies are in typewriter face, while others may be from any type of computer printer.

The quality of this reproduction is dependent upon the quality of the copy submitted. Broken or indistinct print, colored or poor quality illustrations and photographs, print bleedthrough, substandard margins, and improper alignment can adversely affect reproduction.

In the unlikely event that the author did not send UMI a complete manuscript and there are missing pages, these will be noted. Also, if unauthorized copyright material had to be removed, a note will indicate the deletion.

Oversize materials (e.g., maps, drawings, charts) are reproduced by sectioning the original, beginning at the upper left-hand corner and continuing from left to right in equal sections with small overlaps. Each original is also photographed in one exposure and is included in reduced form at the back of the book.

Photographs included in the original manuscript have been reproduced xerographically in this copy. Higher quality 6" x 9" black and white photographic prints are available for any photographs or illustrations appearing in this copy for an additional charge. Contact UMI directly to order.

UMI

A Bell & Howell Information Company
300 North Zeeb Road, Ann Arbor MI 48106-1346 USA
313/761-4700 800/521-0600

**CHARACTERIZATION OF MAGNETIC NANOCOMPOSITES
BASED ON CELLULOSIC MEMBRANES**

by

Erwan SOURTY

**A thesis submitted to the Faculty of Graduate Studies and Research in
partial fulfilment of the requirements of the degree of Master of Science**

Department of Physics

McGill University

Montreal, Quebec, Canada

July 1997

©Erwan SOURTY, 1997



**National Library
of Canada**

**Acquisitions and
Bibliographic Services**

395 Wellington Street
Ottawa ON K1A 0N4
Canada

**Bibliothèque nationale
du Canada**

**Acquisitions et
services bibliographiques**

395, rue Wellington
Ottawa ON K1A 0N4
Canada

Your file Votre référence

Our file Notre référence

The author has granted a non-exclusive licence allowing the National Library of Canada to reproduce, loan, distribute or sell copies of this thesis in microform, paper or electronic formats.

The author retains ownership of the copyright in this thesis. Neither the thesis nor substantial extracts from it may be printed or otherwise reproduced without the author's permission.

L'auteur a accordé une licence non exclusive permettant à la Bibliothèque nationale du Canada de reproduire, prêter, distribuer ou vendre des copies de cette thèse sous la forme de microfiche/film, de reproduction sur papier ou sur format électronique.

L'auteur conserve la propriété du droit d'auteur qui protège cette thèse. Ni la thèse ni des extraits substantiels de celle-ci ne doivent être imprimés ou autrement reproduits sans son autorisation.

0-612-37168-9

Canada

ABSTRACT

This thesis is dedicated to understanding the mechanism of the *in situ* synthesis of magnetic nanocomposites based on cellulosic substrates and characterizing the products of this synthesis. The preparation of uniform membranes containing large quantities of magnetite particles (Fe_2O_3) of defined size was our specific objective. For that purpose, cellulosic substrates of two different kinds: one of bacterial origin (bacterial cellulose - BC), the other (Lyocell) derived from dissolving-grade wood-pulp through a dissolution / coagulation process (film-casting) were used as never-dried gel membranes. BC has also been used in the form of a suspension of open fibrillar pellets which were dried to a parchment after the *in situ* treatment. Characterization of the resulting magnetic materials was performed using transmission electron microscopy (TEM) in imaging and diffraction mode, X-ray diffraction (XRD), vibrating sample magnetometry (VSM) and Mössbauer spectroscopy. In BC membranes, needle-like lepidocrocite ($\gamma\text{-FeOOH}$) formed along the cellulose fibrils, using the crystalline surface as a nucleation site. Spherical magnetite particles subsequently formed around the needles. The less swollen Lyocell substrates produced needle-like feroxyhite ($\delta\text{-FeOOH}$) concentrated at the membrane surface while spherical magnetite particles formed within the membrane after several cycles of treatment. The treated BC and Lyocell membranes were both superparamagnetic at room temperature. The BC suspensions had no space constraint hence the treatment conditions were more critical for controlling the morphology of synthesized ferrites. These conditions could be defined to yield homogeneous membranes containing magnetite particles uniform in size, too large however to behave superparamagnetically at room temperature.

RESUME

Cette thèse est consacrée à la compréhension du mécanisme de synthèse in situ de nanocomposites magnétiques basés sur des substrats celluloses et la caractérisation du produit de cette synthèse. La préparation de membranes chargées abondamment en particules de magnétite (Fe_3O_4) de taille uniforme était notre objectif spécifique. Dans cette optique, des substrats celluloses de deux sortes: l'un d'origine bactérienne (cellulose bactérienne - CB), l'autre (Lyocell) dérivé de pâte à rayonne par le biais d'un procédé de dissolution / coagulation étaient utilisés sous la forme de membranes à l'état gel. La CB était également utilisée sous la forme d'une suspension de pelotes fibrillaires poreuses, ultérieurement séchée en parchemin après le traitement in situ. Les matériaux magnétiques résultants étaient caractérisés par microscopie électronique à transmission en mode image et diffraction, diffraction aux rayons X, magnétométrie à vibration et spectroscopie Mössbauer. Dans les membranes de CB, des aiguilles de lepidocrocite (γ -FeOOH) se formaient le long des fibrilles de cellulose, utilisant la surface cristalline comme site de nucléation. Des particules sphériques de magnétite apparaissaient ultérieurement autour des aiguilles. Les substrats de Lyocell, moins gonflés que ceux de CB, produisaient des aiguilles de feroxyhite (δ -FeOOH) concentrées à la surface de la membrane, tandis que des particules sphériques de magnétite se formaient à l'intérieur de la membrane après plusieurs cycles de traitement. Les membranes de CB et de Lyocell traitées étaient toutes deux superparamagnétiques à température ambiante. L'absence de contrainte d'espace dans les suspensions de CB impliquait un contrôle plus critique sur la morphologie des ferrites synthétisés par les conditions de traitement. Ces conditions purent être définies pour la

*synthèse de membranes contenant des particules de magnétite de taille uniforme, excessive
cependant pour conserver un caractère superparamagnétiques à température ambiante.*

ACKNOWLEDGEMENTS

I would like to both thank and acknowledge the following individuals and groups:

- Dr. R.H. Marchessault, for offering me the privilege to be part of his group, and the opportunity to complete this thesis. I am particularly grateful for his confidence and patience, and his precious teaching.

- Dr. D. Ryan, for accepting to supervise this work. The shrewdness and rigour of his direction were beneficial to my erudition and the quality of this thesis.

- Dr. J.-F. Revol and L. Godbout for their kindness and the experience they shared with me.

- the members of my group and my friends in both the Pulp and Paper Research centre and the Department of Physics, especially Karim, David, Sandra, Patrick, Mohammed and Michael.

- my family by which everything started.

TABLE OF CONTENTS

ABSTRACT	- i -
RESUME	- ii -
ACKNOWLEDGEMENTS	- iv -
TABLE OF CONTENTS	- v -
LIST OF TABLES	- x -
LIST OF FIGURES	- xi -

CHAPTER I - IRON OXIDE AND HYDROXIDE NANOPARTICLES

PROPERTIES AND SYNTHESIS

1. 1. Magnetic properties of nanostructured materials	1
1. 1. 1. Theoretical background	2
1. 1. 1. 1. Magnetization loop	2
1. 1. 1. 2. Anisotropy	3
1. 1. 1. 3. Critical lengths	4
1. 1. 1. 4. Single domain particles	4
1. 1. 1. 5. Superparamagnetism	6
1. 1. 2. Classification of morphologies	8
1. 2. Iron oxides and hydroxides	9
1. 2. 1. Properties	9

1. 2. 1. 1. Ferrous hydroxide - $\text{Fe}(\text{OH})_2$	11
1. 2. 1. 2. Green rust	12
1. 2. 1. 3. Hydrated iron oxides	13
<i>Goethite - $\alpha\text{-FeOOH}$</i>	14
<i>Akaganeite - $\beta\text{-FeOOH}$</i>	15
<i>Lepidocrocite - $\gamma\text{-FeOOH}$</i>	15
<i>Feroxyhite - $\delta\text{-FeOOH}$</i>	16
<i>Ferrihydrite - $5\text{Fe}_2\text{O}_3 \cdot 9\text{H}_2\text{O}$</i>	17
1. 2. 1. 4. Iron oxides	18
<i>Haematite</i>	18
<i>Ferrospinels - magnetite (Fe_3O_4) and maghemite ($\gamma\text{-Fe}_2\text{O}_3$)</i>	18
1. 2. 2. Synthesis	25
1. 3. References	40

**CHAPTER II - MATERIALS AND CHARACTERIZATION METHODS: GENERAL
DESCRIPTION**

2. 1. Materials	42
2. 1. 1. Bacterial cellulose	42
2. 1. 2. Lyocell	45
2. 2. Characterization methods	47

2. 2. 1. Transmission electron microscope (TEM)	47
2. 2. 1. 1. Electron optic elements	49
<i>Magnetic lenses</i>	49
<i>Deflection coils</i>	50
<i>Stigmators</i>	51
2. 2. 1. 2. The optics of a TEM	52
<i>Illumination system</i>	52
<i>Objective lens</i>	53
<i>Imaging lens system</i>	55
2. 2. 1. 3. TEM modes	56
<i>Bright field imaging</i>	56
<i>Diffraction</i>	57
<i>Dark field imaging</i>	58
<i>Low dose mode</i>	59
2. 2. 1. 4. Sample preparation	59
<i>Embedding</i>	59
2. 2. 2. Vibrating sample magnetometry	60
2. 2. 3. Mössbauer spectroscopy	64
2. 2. 3. 1. Theory of Mössbauer spectroscopy	65
<i>The Mössbauer effect</i>	65
<i>Mössbauer spectrometer</i>	66
<i>Interpretation of the Mössbauer data</i>	67

2. 2. 3. 2. Application of Mössbauer spectroscopy to superparamagnetism	72
2. 3. References	75

CHAPTER III - MAGNETIC MEMBRANES BASED ON BACTERIAL AND MAN- MADE CELLULOSE

3. 1. Introduction	77
3. 2. Experimental section	80
3. 2. 1. Materials	80
3. 2. 2. <i>In situ</i> synthesis	81
3. 2. 3. Transmission electron microscopy	82
3. 2. 4. Magnetic characterisation	82
3. 3. Results and discussion	83
3. 3. 1. Transmission electron microscopy	83
3. 3. 2. Vibrating sample magnetometry	94
3. 3. 3. Mössbauer spectroscopy	99
3. 4. Conclusion	104
3. 5. References	105

**CHAPTER IV - MAGNETIC MEMBRANES MADE FROM BACTERIAL CELLULOSE
FIBRILLAR SUSPENSIONS**

4. 1. introduction	107
4. 2. Experimental section	108
4. 2. 1. Materials	108
4. 2. 2. <i>In situ</i> synthesis	108
4. 2. 3. X-ray diffraction	112
4. 2. 4. Transmission electron microscopy	112
4. 2. 5. Magnetic characterisation	112
4. 3. Results and discussion	113
4. 3. 1. Macroscopic aspect	113
4. 3. 2. X-ray diffraction	116
4. 3. 3. Transmission electron microscopy	121
4. 3. 4. Vibrating sample magnetometry	138
4. 4. Conclusion	142
CONCLUSION	144

LIST OF TABLES

Table 1. 1. estimated single-domain sizes for spherical particles with no shape anisotropy.

Table 1. 2. Summary of the crystal structures of oxides and hydroxides of iron.

Table 1. 3. Magnetic properties of materials.

Table 1. 4. Mössbauer data at room temperature.

Table 2. 1. Structure and physico-chemical properties of bacterial cellulose under static or stirred culture conditions.

Table 2. 2. Lens and aperture functions in HM and LM.

Table 3. 1. Percentage of the sample weight attributable to iron. The first column was deduced from the fit of the magnetisation curves, assuming that the iron was entirely present as magnetite. The iron composition on the last column was determined by digesting a weighed sample in an acid mixture and analysing using atomic absorption.

Table 3. 2. Hyperfine fields measured on the Mössbauer spectra for the sextet related to magnetite.

Table 4. 1. Colours observed during *in situ* process.

LIST OF FIGURES

Figure 1. 1. Important parameters obtained from a magnetic hysteresis loop.

Figure 1. 2. Qualitative illustration of the behaviour of the coercivity in ultrafine particle systems as the particle size changes.

Figure 1. 3. Schematic representation of the different types of magnetic nanostructures.

Figure 1. 4. Structural transformations in the iron oxide/hydroxide system.

Figure 1. 5. The cubic close-packed oxygen lattice.

Figure 1. 6. Transmission electron micrographs of a system consisting of ferrous hydroxide and excess concentration of FeSO_4 aged at 90°C .

Figure 1. 7. Time variation of the amounts of products Fe_3O_4 and Fe^{3+} oxides and of $\text{Fe}(\text{OH})_2$ and Fe^{2+} in the reaction suspension during the course of the air oxidation of $\text{Fe}(\text{OH})_2$ suspensions at pH 11.0 and 65°C .

Figure 2. 1. N-methylmorpholine-N-oxide (NMMO).

Figure 2. 2. Direct dissolution: Courtaulds Tencel process.

Figure 2. 3. Cross section of the electron optical column.

Figure 2. 4. Schematic cross section of an electromagnetic lens.

Figure 2. 5. (a) general principle of a beam deflector; (b) actual design of the microscope's deflection system.

Figure 2. 6. The triode electron-source.

Figure 2. 7. The TWIN lens (a) microprobe and (b) nanoprobe modes.

Figure 2. 8. Graph showing the change in the currents through the lenses of the magnification system of a CM20 as a function of magnification.

Figure 2. 9. first model of vibrating sample magnetometer.

Figure 2. 10. functional diagram of the complete FM-1 system.

Figure 2. 11. vibrating capacitor assembly.

Figure 2. 12. nuclear decay of ^{57}Co showing the transition giving the 14.4 KeV Mössbauer gamma ray.

Figure 2. 13. A block diagram of a typical Mössbauer spectrometer.

Figure 2. 14. The effects on the nuclear energy levels of ^{57}Fe of (a) the isomer shift, (b) the quadrupole splitting and (c) the magnetic splitting.

Figure 3. 1a. Electron micrograph of Lyocell membrane after one cycle of the *in situ* process.

Figure 3. 1b. Electron micrograph of Lyocell membrane after three cycles of the *in situ* process. The equiaxial particles not observed after one cycle, are present here.

Figure 3. 2. XRD pattern of Lyocell (7.5%) membranes *in situ* treated over one cycle (upper most), two cycles and three cycles (lower most). (a) ground membrane; (b) membrane “as prepared”.

Figure 3. 3. Transmission electron micrograph of ultrathin section of a neverdried Lyocell membrane. The ferrites were oxidized by contact with atmospheric air (slow oxidation).

Figure 3. 4. Electron micrograph of a never-dried BCR membrane section after three

cycles of the *in situ* process. Acicular particles are surrounded by equiaxial particles in a very open texture.

Figure 3. 5a. Electron micrograph of a dried BCS membrane section after one cycles of the *in situ* process. Rodlike particles are visible on the surface.

Figure 3. 5b. Electron micrograph of a dried BCS membrane section after three cycles of the *in situ* process. Equiaxial particles are larger on the surface than inside the membrane.

Figure 3. 6. Magnetisation curves measured by VSM for Lyocell (above) and BCR (below) membranes. The fit using equation (1) is represented as a solid line.

Figure 3. 7. Magnetisation moment distribution deduced from the fit of the magnetisation curves. Top is Lyocell, bottom is bacterial cellulose membrane.

Figure 3. 8. Mössbauer spectra for Lyocell at room temperature. The membranes were *in situ* treated over 1 cycle (uppermost spectrum), 2 cycles and 3 cycles (lowermost spectrum).

Figure 4. 1. Colour taken by the different samples after the whole *in situ* process (second set).

Figure 4. 2. XRD patterns for the first set; (i) non-centrifuged, (ii) centrifuged.

Figure 4. 3. XRD pattern for the second set.

Figure 4. 4. Transmission electron micrograph for the first set, sample (i).

Figure 4. 5. Transmission electron micrograph for the first set, sample (ii).

Figure 4. 6. Transmission electron micrograph for the second set, low $[\text{Fe}^{2+}]$.

Figure 4. 7. Transmission electron micrograph for the second set; intermediate $[\text{Fe}^{2+}]$.

Figure 4. 8. Transmission electron micrograph for the second set; high $[\text{Fe}^{2+}]$.

Figure 4. 9. Transmission electron micrograph for the second set; intermediate $[\text{Fe}^{2+}]$, treaded in ferrous chloride extended from two to four hours.

Figure 4. 10. Transmission electron micrograph for the second set; low $[\text{NaOH}]$.

Figure 4. 11. Transmission electron micrograph for the second set; intermediate $[\text{NaOH}]$.

Figure 4. 12. Transmission electron micrograph for the second set, high $[\text{NaOH}]$.

Figure 4. 13. Transmission electron micrograph for the second set, two hours treatment in NaOH , oxidation at 80°C .

Figure 4. 14. Transmission electron micrograph for the second set; five minutes treatment in NaOH , oxidation at 80°C .

Figure 4. 15. Transmission electron micrograph for the second set; two hours treatment in NaOH , oxidation at room temperature.

Figure 4. 16. Transmission electron micrograph of a treated suspension. The grown ferrites are clearly localized along the cellulose fibrils.

Figure 4. 17. Magnetisation curves measured by VSM.

CHAPTER I - IRON OXIDE AND HYDROXIDE NANOPARTICLES

PROPERTIES AND SYNTHESIS

1. 1. Magnetic properties of nanostructured materials

Nanosized magnetic particles have properties quite different from those of corresponding bulk materials. Due to their nanoscopic size (usually between 1 to 100 nm), they have unique electrical, chemical, structural and magnetic properties. Above a certain temperature (blocking temperature) their magnetic behaviour is essentially similar to paramagnetism, featuring no remanence or coercivity, although keeping very high susceptibility. This behaviour is known as superparamagnetism and can be viewed as intermediate between paramagnetism and ferromagnetism.

Applications of superparamagnetism can be found in many domains, such as ferrofluids (Pankhurst and Pollard, 1993), colour imaging (Ziolo *et al.*, 1992) (high magnetization combined with weak optical absorption), biotechnology (efficient aggregation in presence of a field but uniform stable suspension without) (Pankhurst and Pollard, 1993; Whiteside *et al.*, 1983) - magnetic separation (cell fractionation, immunoassay, water purification...) or drug delivery -, magnetic refrigeration (Zachariah *et al.*, 1995) (combining the large magnetisation at moderate temperature of ferrimagnetism to the large magneto caloric effect of paramagnetism).

1. 1. 1. Theoretical background

1. 1. 1. 1. Magnetization loop

When exposed to an applied magnetic field, the spins present inside a magnetic material will tend to align with the field. The phenomenon increases the global magnetization of the material (figure 1.1) which reaches a maximum (the saturation magnetization, usually noted M_s) when all its spins are aligned. Once the material has reached this state, decreasing the field results in a decreasing of the magnetization, until, in zero applied field, reaching the remanent magnetization (M_r). The ratio of the remanent magnetization to the saturation magnetization, M_r/M_s is called the remanent ratio and changes according to the material considered; for paramagnetic material, this ratio is null resulting from the thermal fluctuation of non-interacting spins whereas for ferro-, ferri- and antiferromagnetic material the remanent ratio ranges from zero to one resulting from the ordering between interacting spins. The field that it is necessary to apply in order to set the magnetization to zero is called the coercive field, H_c .

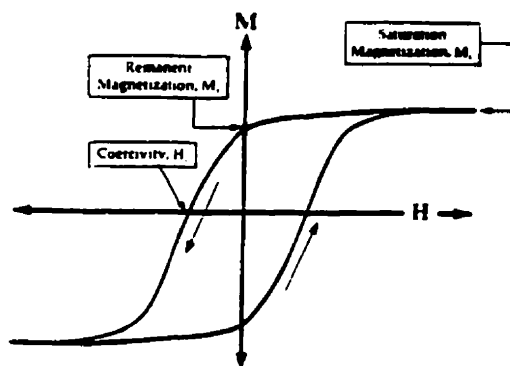


Figure 1.1. Important parameters obtained from a magnetic hysteresis loop (Leslie-Pelecky and Rieke, 1996).

1. 1. 1. 2. Anisotropy

The behaviour of the magnetization can be affected by many kinds of anisotropies, the most common types being (i) crystal anisotropy, (ii) shape anisotropy, (iii) stress anisotropy, (iv) externally induced anisotropy, and (v) exchange anisotropy.

Magneto-crystalline anisotropy (i) arises from spin-orbit coupling and energetically favours alignment of the magnetization along a specific crystallographic direction called the easy axis of the material. Only non-spherical particles will have a shape anisotropy (ii): they are easier to magnetize along longer than shorter directions.

These two anisotropies are the most common for nanostructured materials. Other anisotropies can be present such as stress anisotropy (iii), resulting from external or internal stresses due to rapid cooling, application of external pressure, externally induced anisotropy (iv), induced by annealing in a magnetic field, plastic deformation, or ion beam irradiation, and exchange anisotropy (v) occurring when a ferromagnet is in close proximity to an antiferromagnet or a ferrimagnet.

The anisotropy can often be modelled as uniaxial in character and represented by

$$E = K_{\text{eff}}V \sin^2\theta,$$

where K_{eff} is the effective uniaxial energy per unit volume, θ is the angle between the moment and the easy axis, and V is the particle volume.

1. 1. 1. 3. Critical lengths

Change in the magnetization of a material occurs *via* activation over an energy barrier associated with different fundamental magnetic lengths: the crystal anisotropy length, $l_K = \sqrt{J/K}$, the applied field length, $l_H = \sqrt{2J/HM_s}$ and the magnetostatic length, $l_s = \sqrt{J/2\pi M_s^2}$. K stands for the anisotropy constant of the bulk material due to the dominant anisotropy, J is the exchange within a grain, M_s is the saturation magnetization and H the applied field. The magnetic properties are dominated by the shortest characteristic length which for most materials ranges from 1 to 100 nm.

The fundamental motivation for studying magnetic nanostructured materials comes from the dramatic changes in magnetic properties occurring when these critical lengths are comparable to the nanoparticle or nanocrystal size. Furthermore, effects due to the surfaces or the interfaces become very important.

1. 1. 1. 4. Single domain particles

Within a bulk magnetic material there exist an interaction field between the atomic moments which causes their alignment. The breakup of the magnetization into localized regions (domains), providing for flux closure at the end of the specimen, reduces the magnetostatic energy. Providing that the decrease in magnetostatic energy is greater than the energy needed to form magnetic domain walls, multidomain specimen will arise. Magnetization reversal occurs then through the nucleation and motion of the domain walls.

Below a critical size (D_c) however, the formation of domain walls becomes energetically unfavourable and the material forms single domain particles: changes in the magnetization can no longer occur through domain wall motion and instead require the coherent rotation of spins, resulting in larger coercivities (figure 1.2). An estimate of D_c is given in table 1.1 for a spherical particles (*i.e.* with no shape anisotropy) of different materials.

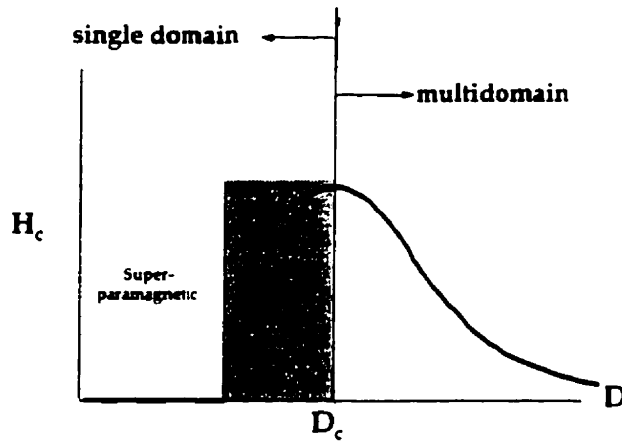


Figure 1. 2. Qualitative illustration of the behaviour of the coercivity in ultrafine particle systems as the particle size changes (Leslie-Pelecky and Rieke, 1996).

Material	D_c (nm)
Co	70
Fe	14
Ni	55
Fe_3O_4	128
$\gamma-Fe_2O_3$	166

Table 1. 1. estimated single-domain sizes for spherical particles with no shape anisotropy (Leslie-Pelecky and Rieke, 1996).

1. 1. 1. 5. Superparamagnetism

The anisotropy energy being proportional to the particle volume, for a small particle (≤ 10 nm) it may become comparable to the thermal energy, even at temperature below room temperature, causing the magnetization to fluctuate in a random way. Small fluctuations around an easy direction are called *collective magnetization excitations*, whereas one talks about *superparamagnetic relaxation* when the magnetization fluctuates among the various easy directions. When the superparamagnetic relaxation time is short compared with the time scale of the experimental method used for the study of the magnetic properties, the sample resembles a paramagnet.

The experimental criteria for superparamagnetism are that the magnetization curve (i) exhibits no hysteresis and (ii) at different temperatures must superpose in a plot of the magnetization versus the applied field divided by the temperature (M vs H/T). Imperfect superposition can result from a broad distribution of particle sizes, changes in the spontaneous magnetization of the particles as a function of temperature, or anisotropy effects.

Intrinsic magnetisation and Curie temperature were experimentally found independent of the particle size, and a uniform magnetisation is indeed conserved inside the particle (Crangle, 1977).

For a particle with a uniaxial anisotropy corresponding to the energy barrier $\Delta E = KV$, a blocking temperature T_B can be defined as

$$T_B = \Delta E / \ln(\tau_m f_0) k_B,$$

where τ_m corresponds to the measuring time while f_0 is usually taken as 10^{12} s^{-1} (Dickson *et al.*, 1993).

The particles are blocked for temperatures below T_B : they do not relax during the time of the measurement. Above T_B , the particles are free to align with applied field during the measuring time. This state is called superparamagnetic, because the particles behave similarly to paramagnetic spins, although featuring a magnetic moment 10^5 times larger (resulting from the magnetic coupling of $\sim 10^5$ atoms) along with larger relaxation times (Bean and Livingston, 1959).

The magnetization of a system of superparamagnetic particles, follows Langevin's law:

$$M_s / M_s = \coth (\mu H_0 / k_B T) - k_B T / \mu H_0$$

with M_s , the apparent magnetisation; $M_s = \mu/V$, the particle magnetic moment divided by its volume, and H_0 , the applied magnetic field.

At low fields ($\mu H_0 \ll kT$), the magnetization behaves as $\mu H_0 / 3kT$ and at high fields ($\mu H_0 \gg kT$) as $1 - kT / \mu H_0$. If a distribution of particle sizes is present, the initial susceptibility is sensitive to the larger particles present, and the approach to saturation is more sensitive to the smaller particles present.

Integration of the Langevin function over a size distribution gives the total magnetization. Assuming a form for the distribution, the width and mean particle size can be determined from the magnetization as a function of the field. This determination does not account for any interparticle interaction and can thus only be used in systems that can be treated as weakly interacting.

1. 1. 2. Classification of nanostructured morphologies

The following classification (Leslie-Pelecky and Rieke, 1996) has been designed for nanostructured materials in order to emphasize the physical mechanism responsible for their magnetic behaviour (figure 1.3).

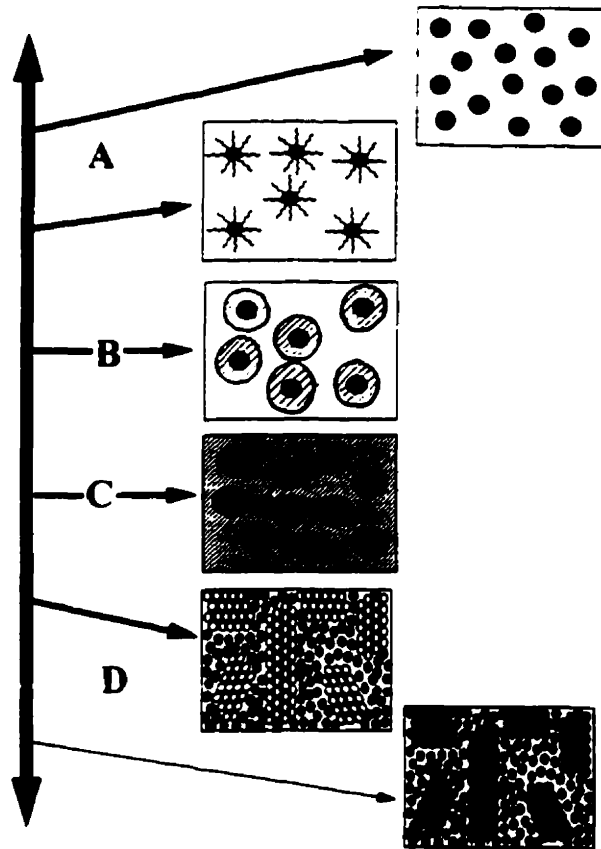


Figure 1. 3. Schematic representation of the different types of magnetic nanostructures (Leslie-Pelecky and Rieke, 1996).

The first group (A) includes non-interacting isolated particles deriving their unique magnetic properties strictly from their reduced size. In the second group (B) are ultra fine

particles with core-shell morphology. The presence of a shell (*eg.* caused by oxidation) can prevent interaction between particles, usually however at the cost of a core-shell interaction. The third group (C) consists of nanocomposite materials in which magnetic particles are dispersed throughout a chemically dissimilar matrix, the magnetic interactions being determined by the volume fraction of the magnetic particles and the character of the matrix. The last group (D) concerns bulk materials with nanoscale structure of crystallites dispersed in a non-crystalline matrix of different or identical phase.

1. 2. Iron oxides and hydroxides

1. 2. 1. Properties

Iron in aqueous solution can precipitate or crystallise in the form of iron oxides or oxihydroxides with different degree of oxidation or hydration. The different crystalline phases are related by either topotactic transformations - *i.e.* the atoms are rearranged in a way that the two phases have a definite relationship to each other - or non topotactic (figure 1.4) (Bernal *et al.*, 1959).

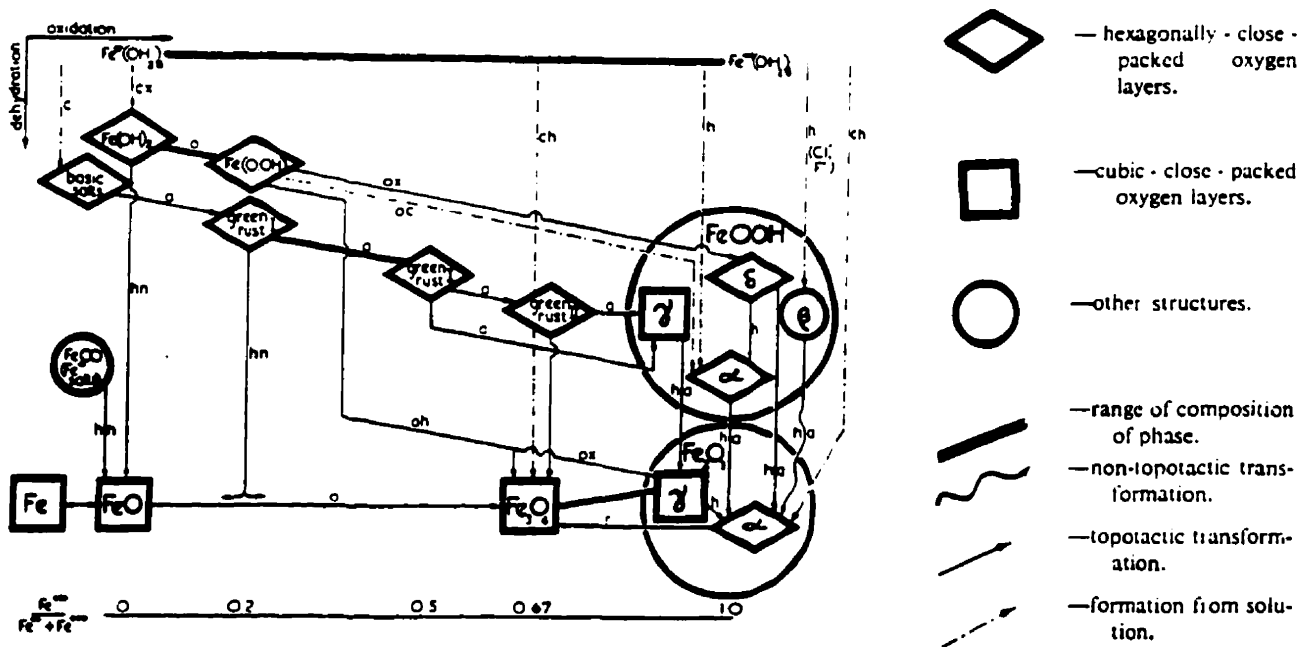


Figure 1. 4. Structural transformations in the iron oxide/hydroxide system. *a*: on exposure to air; *c*: in alkali; *h*: on heating; *n*: in nitrogen or *in vacuo*; *o*: on oxidation; *r*: on reduction; *x*: in excess (Bernal *et al.*, 1959).

The crystalline phases have in common a stacking of close-packed oxygen / hydroxyl sheets with various arrangements of the iron in the octahedral or tetrahedral interstices (figure 1.5). A regular stacking will give good crystals with intense characteristic diffraction lines. However, these phases can appear in amorphous form or in states where the layers may be largely intact but disordered.

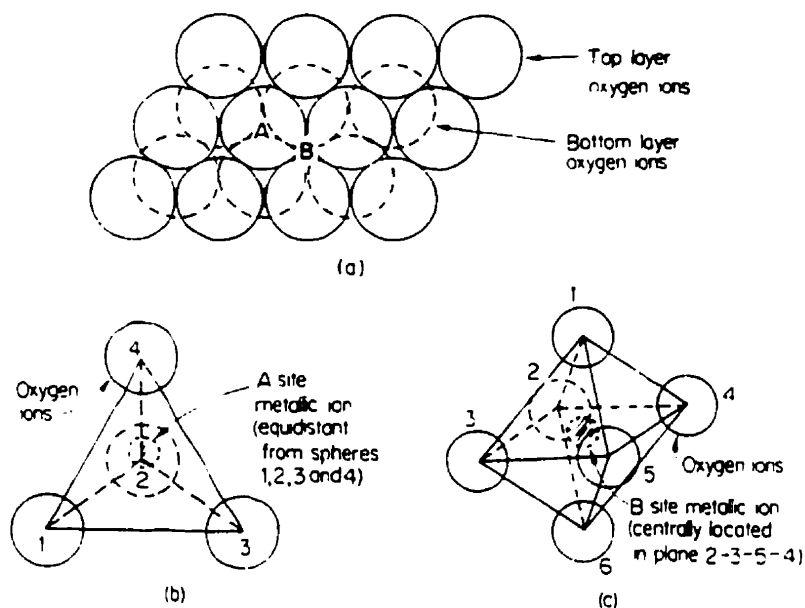


Figure 1. 5. The cubic close-packed oxygen lattice, (a) A and B sites for metallic ions; (b) tetrahedral coordination: spheres 1, 2, 3 corresponds to top layer oxygen ion in (a); (c) octahedral coordination; spheres 1, 2, 3 correspond to bottom layer and spheres 4, 5, 6 correspond to top layer oxygen ions in (a) (Sohoo, 1960).

1. 2. 1. 1. Ferrous hydroxide - $Fe(OH)_2$

When a solution of ferrous ions is added to excess alkali with the strict exclusion of oxygen, a white precipitate of ferrous hydroxide appears, giving sharp X-Ray diffraction peaks

corresponding to a hexagonal cell with $a = 3.258 \text{ \AA}$ and $c = 4.605 \text{ \AA}$. Although very sensitive to the presence of oxygen, this precipitate can maintain its structure until the ferric ion content resulting from the oxidation of ferrous ions is 10 % of the total iron (Bernal *et al.*, 1959).

When a very dilute solution of hydrogen peroxide is added very slowly to a hot suspension of ferrous hydroxide, $\gamma\text{-Fe}_2\text{O}_3$ (maghemite) can be formed. If the suspension is highly alkaline, addition of a strong solution of hydrogen peroxide would yield $\delta\text{-FeOOH}$ (feroxyhite), whereas bubbling with oxygen would yield $\alpha\text{-FeOOH}$ (goethite) (Powers, 1975).

1. 2. 1. 2. "Green rust"

If insufficient alkali is added to precipitate all the ferrous ions as ferrous hydroxide (oxygen free conditions) and air is subsequently bubbled through the suspension, a blue-green compound will result. If aerial oxidation is continued, $\gamma\text{-FeOOH}$ (lepidocrocite) is formed as final product (Bernal *et al.*, 1959). The compounds described below were distinguished from their X-Ray diffraction pattern.

Green rust I can be produced by aerial oxidation of FeCl_2 solution partially precipitated with sodium hydroxide. The product has a structure built from close-packed oxygen layers stacked ABC BCA CAB. The composition calculated to $9(\text{O},\text{OH},\text{Cl})$ per cell would then range between $\text{Fe}^{2+}_{3.6} \text{Fe}^{3+}_{0.9} (\text{O},\text{OH},\text{Cl})_9$ at 20% oxidation and $\text{Fe}^{2+}_{1.95} \text{Fe}^{3+}_{2.55} (\text{O},\text{OH},\text{Cl})_9$ at 57% oxidation. It has a dark-green colour.

Green rust II has a hexagonal cell with $a = 3.17 \text{ \AA}$ and $c = 10.9 \text{ \AA}$, presumably built on a four close-packed oxygen / hydroxyl layer, in a ABAC sequence. It has a dark-green colour.

Aerial oxidation, gave γ -FeOOH as the end product in all instances. On violent oxidation with a strong solution of hydrogen peroxide, both complexes gave disordered δ -FeOOH. The product of green rust II oxidation gave the four main X-ray powder diffraction peaks of δ -FeOOH ((100), (101), (102) and (110)) plus a peak at 10.9 Å, while that of green rust I gave only the (100) and (110) peaks plus one at 7.3 Å. On heating to dryness, the green rusts break down, principally to Fe₂O₃ (magnetite) and some FeO (wüstite).

Compounds obtained by partial precipitation of chloride solutions were also reported as basic chloride, with compositions Fe(OH)₂ - FeCl₂ (a rhombohedral CdCl₂ structure with a=3.40 Å and c = 16.92 Å), 2 Fe(OH)₂ - FeCl₂ (a CdI₂ - type structure with a = 3.32 Å and c = 5.52 Å) and 3 Fe(OH)₂ - FeCl₂.

1. 2. 1. 3. Hydrated iron oxides

Hydrated iron oxides include the ferric oxihydroxydes of stoichiometry FeOOH (or Fe₂O₃.H₂O, although these may contain additional absorbed water) and the poorly crystalline 5Fe₂O₃.9H₂O (ferrihydrite). Five different crystalline phases are known for FeOOH, amongst which α -FeOOH (goethite) and γ -FeOOH (lepidocrocite) are the most common. β -FeOOH (akaganeite) is less frequently encountered being stable only in chloride environment. δ -FeOOH (feroxyhite) is a completely synthetic allotrope, the poorly crystalline δ' -FeOOH being its counterpart in soils. They are the only ferrimagnetic oxihydroxides (the others being antiferromagnetic).

The oxihydroxide structure is based on octahedral coordinated ferric ions surrounded by

oxygen with different spacial arrangements of the octahedra, and hydrogen bonds between some oxygens.

Goethite - α -FeOOH

Goethite is by far the most common compound in Fe-bearing soil sediments and clays. It can be formed if oxygen is passed through a strongly alkaline suspension of $\text{Fe}(\text{OH})_2$. It is used in the form of a commercial yellow pigment as the starting material from which acicular maghemite particles used for recording are prepared.

In its most ideal form, it is antiferromagnetic with the Fe moments lying along the c axis of its hexagonal close-packed crystalline structure. The Néel temperature has been measured to be 393.3 K and the anisotropy constant K, is of the order of $10^3 \text{ J}\cdot\text{m}^{-3}$.

The Mössbauer spectrum shows magnetic hyperfine fields of 38.1 T at RT, 50.0 T at 80 K and 57.7 T at 4 K and quadrupole shifts of $2\epsilon = -0.28 \text{ mm/s}$ at RT and -0.26 mm/s at 80 K. For small superparamagnetic particles, at room temperature, the quadrupole splitting ($\Delta (T > T_B) \sim 0.55 \text{ mm/s}$) is typical of Fe(III) ions in octahedral sites.

Akaganeite - β -FeOOH

Akaganeite is formed as a light brown deposit when a ferric solution is hydrolysed by boiling in presence of Cl^- ion (Bernal *et al.*, 1959). It was reported to form only at high temperature ($> 100^\circ\text{C}$) (Mann and Hannington, 1988) and to require the presence of chloride or fluoride ions to stabilise a crystal structure based on a body centred tetragonal cell with $a = 10.48 \text{ \AA}$ and $c = 3.023 \text{ \AA}$. It is antiferromagnetic with a Néel temperature $T_N = 295 \text{ K}$ (Bowen *et al.*, 1993).

At low temperatures, the Mössbauer spectrum requires three sextets for fitting: one attributed to the Fe(III) ions in $\text{O}_2(\text{OH})_3$ configuration, another in $\text{O}_2(\text{OH})_4$, the last caused by a spin hopping between the two sites which have different canting angles. The room temperature spectrum (*ie.* above T_N) is clearly composed of two doublets: $\Delta (\text{O}_2(\text{OH})_3) \sim 0.55 \text{ mm/s}$ and $\Delta (\text{O}_2(\text{OH})_4) \sim 0.95 \text{ mm/s}$ (Vanderberghe *et al.*, 1990).

Lepidocrocite - γ -FeOOH

Lepidocrocite was reported as the aerial oxidation product of green rust I and II while it has never been produced directly from ferrous hydroxide. Its structure differs from that of goethite in that it is based on a cubic rather than an hexagonal close-packing of the oxygen atoms. It appears typically as an orange compound with the morphology of small, very thin raggedly structured platelets. It is antiferromagnetic, showing a broad magnetic transition over a wide temperature range around 65 K.

The room temperature Mössbauer spectrum is a broadened doublet with an average quadrupole splitting between .55 and .7 mm/s that was analysed as a distribution with two maxima, $\Delta \sim 0.52$ mm/s attached to the bulk particle and $\Delta \sim 1.1$ mm/s resulting from the surface species.

At 4 K, the magnetic hyperfine field lays between 44 T to 46 T (45.8 T for well crystallised samples - Bowen *et al.*, 1993) with $2\epsilon \sim 0.02$ mm/s, much lower than that of the other iron oxides and hydroxides, except ferrihydrite.

Feroxyhite - δ -FeOOH

δ -FeOOH can be obtained by oxidation of a strongly alkaline suspension of ferrous hydroxide with excess hydrogen peroxide, as a brown magnetic material. Its crystallographic structure was first described by the "80/20" model, where ferric ions would be distributed for 80% in the octahedral and 20% in the tetrahedral interstices of a hexagonal close-packing of oxygen atoms (Francombe and Rooksby, 1959). This model however, was not able to describe the magnetic behaviour and feroxyhite was later rather described as a disordered arrangement of oxygen and hydroxyl ions with ferric ions randomly occupying octahedral and possibly tetrahedral sites (Powers, 1975; Pankhurst and Pollard, 1993). δ -FeOOH is found to have a very high magnetic susceptibility, together with a small remanence and very narrow hysteresis loop, the saturation magnetisation, not reached until about 0.3 T, has been reported as being up to 19 J/T/Kg by Bernal *et al.* (1959), and up to 25 J/T/kg by Bate (1975). The Curie temperature is $T_c = 400$ K.

Three magnetic hyperfine fields were associated with the two sublattices to model the effect of the crystalline disorder, but the anisotropy and exchange field were taken to be single valued.

Ferrihydrite - $5\text{Fe}_2\text{O}_3 \cdot 9\text{H}_2\text{O}$

Ferrihydrite has been reported as “colloidal hydrous ferric oxide” by Towe and Bradley (1967). It was found in poorly crystalline preparations formed by the precipitation of a solute base on a ferric salt solution, as a precipitate made up of extremely fine particles of dimensions averaging less than 5 nm (Towe and Bradley, 1967; Vandenberghe *et al.*, 1990). It occurs naturally in ferritin shells. It has been described as an iron oxihydroxide with a high surface water content which composition ranges between $\text{Fe}_4(\text{OH})_{12}$ and $\text{Fe}_5\text{O}_3(\text{OH})_9$.

X-ray diffraction (XRD) patterns of ferrihydrite consist of two to six broad peaks which are not always discernable due to the presence of broad lines of poorly crystalline goethite which often accompanies ferrihydrite. These diffraction patterns suggested an arrangement based on the hexagonal close-packing of oxygens with Fe^{3+} ions located on some octahedral sites. Electron diffraction from very fine material resulting from ferric salt base precipitation techniques invariably showed the presence of two broad bands, one in the vicinity of 2.55 Å and the other near 1.47 Å.

Its poor crystallinity results in a superparamagnetic behaviour at room temperature, with a relative large anisotropy constant $K \sim 10^5 \text{ J.m}^{-3}$. For well crystallised sample with six line XRD patterns, the blocking temperature T_B ranges between 34 and 110 K. The RT Mössbauer spectra

features a doublet with quadratic splitting $\Delta \sim 0.7\text{-}0.9$ mm/s and isomer shift characteristic of iron (III) in octahedral oxygen coordination. Either a two doublet fit or preferably fitting with a distribution of quadratic splitting is required.

1. 2. 1. 4. Iron Oxides

Haematite - $\alpha\text{-Fe}_2\text{O}_3$

Haematite is the most stable ferric oxide. It crystallises in an rhombohedral system group (R3C) made up of distorted hexagonal closed-packed layers of oxygen ions. Ferric ions fill 2/3 of the octahedral interstices.

Haematite is a weak canted antiferromagnet ($T_c = 955$ K) above the Morin temperature ($T_M = 260$ K) featuring a magnetization up to 0.5 J/T/kg. Below that temperature, it is a purely antiferromagnet. The anisotropy constant is $\sim 10^4$ J.m⁻³ (Vandenberghe *et al.*, 1990)

Ferrospinel - magnetite (Fe_3O_4) and maghemite ($\gamma\text{-Fe}_2\text{O}_3$)

The general formula for ferrospinel is MeFe_2O_4 , where Me is usually a divalent cation (Me^{2+}), although it can denote trivalent (Me^{3+}) or monovalent (Me^+) cations.

It has a cubic face-centred crystallographic structure of the space group Fm3d similar to the mineral spinel MgAl_2O_4 with a unit cell containing eight formula units. The structure is determined by the lattice of oxygen ions, with two kinds of interstitial sites: tetrahedral or A-sites

and octahedral or B-sites. The vacant interstitial sites are distributed following a geometrical law that determines a large multiple cubic lattice with $a_0 \sim 8 \text{ \AA}$, containing 32 octahedral sites, half being vacant, and 64 tetrahedral sites, 7/8 being vacant.

The distribution of metallic ions in the interstices is dependent of the ion size and electronic configuration, the ones of small size and a strong electrostatic field prefer tetrahedral sites, whereas the ones of large size and weak electrostatic field prefer octahedral sites. Divalent ions are generally larger than trivalent and tetravalent ions thus locate preferentially in octahedral sites.

Most ferros spinels are inverse: $\text{Fe}^{3+}_A \downarrow [\text{Me}^{2+} \uparrow \text{Fe}^{3+} \uparrow]_B \text{O}_4$, the unbalance in the spin orientation being responsible for their ferrimagnetic behaviour (approximately, the spontaneous magnetization per unit η_β - or per gram: $\sigma = N_A \eta_\beta \beta / \text{molecular weight}$ - corresponds simply to the number of unpaired spins for the Me^{2+} ion - for Fe_3O_4 , $\eta_\beta = 4.55$ and for $\gamma\text{-Fe}_2\text{O}_3$, $\eta_\beta = 2.3$ - Craik, 1975).

Stoichiometric magnetite, $\text{Fe}^{3+}_{\text{tet}} [\text{Fe}^{2+} \text{Fe}^{3+}]_{\text{oct}} \text{O}_4$, is the only pure iron oxide of mixed valence. The size of the cubic cell is $a_0 = 8.39 \text{ \AA}$.

A metal-insulator transition (Verwey transition) identified by an abnormal specific heat and a drastic decrease of the electrical conductivity measurements, occurs at $T_w = 119 \text{ K}$. A high conductivity results above T_w from the electron hopping between Fe ions of different valence in octahedral sites. T_w is depressed by impurities and non-stoichiometry.

Magnetite has the highest saturation magnetization of all oxide and hydroxide compounds with $M_s \sim 92 \text{ J/T/kg}$; its anisotropy constant is $K \sim 10^5 \text{ J.m}^{-3}$.

If a proportion of the ferrous ions contained in magnetite are oxidized to ferric ions, the introduction of vacancies will result in order to preserve the electro-neutrality, schematically: $3\text{Fe}^{2+} \rightarrow 2\text{Fe}^{3+} + \text{Vacancy}$. The formula for magnetite might then be changed to the general formula $\text{Fe}_{3-x}\text{O}_4$, stoichiometric magnetite corresponding to the case $x = 0$ and maghemite, the completely oxidized form, $x = 1/3$. Some authors suggest the existence of a continuous solid series between Fe_3O_4 and $\gamma\text{-Fe}_2\text{O}_3$ with proportional change in cell size with $\text{Fe}^{2+} / \text{Fe}^{3+}$ composition.

Maghemite, the extreme oxidation state of magnetite, can be expressed as $\text{Fe}^{3+}_{\text{tet}} [\text{Fe}^{3+}_{5/3} \square_{1/3}]_{\text{oct}} \text{O}_4$, where \square stands for the vacancies. This may lead to a crystallographic ordering on the octahedral sites giving rise to additional super-structure lines in the X-ray pattern. Bernal *et al.* (1959) report four different varieties of maghemite: (I) a completely ordered variety, commercially produced as acicular pseudomorphic polycrystal following the sequence: $\alpha\text{-FeOOH} \rightarrow \alpha\text{-Fe}_2\text{O}_3 \rightarrow \text{Fe}_3\text{O}_4 \rightarrow \gamma\text{-Fe}_2\text{O}_3$, (ii) a cubic variety, produced by the oxidation of $\text{Fe}(\text{OH})_2$ by dilute H_2O_2 , or from magnetite heated in air, (iii) a variety of formula ranging between $\text{Fe}_8 [\text{Fe}_{12}\text{H}_4] \text{O}_{32}$ and $\text{Fe}_8 [(\text{Fe}_{1.33} \square_{2.67}) \text{Fe}_{12}] \text{O}_{32}$, according to the amount of H present, and finally (iv) a variety with $a_0 = 8.35 \text{ \AA}$, obtained by dehydrating $\gamma\text{-FeOOH}$ as $\text{Fe}_8 [\text{Fe}_{1.33} \square_{2.67}] \text{O}_{32}$.

Maghemite has a lower saturation magnetization than magnetite, $M_s \sim 74 \text{ emu/g}$, and an anisotropy constant $K \sim 10^5 \text{ J.m}^{-3}$.

Mössbauer spectra for maghemite feature two six-line hyperfine pattern corresponding to the tetrahedral (A-) sites and the octahedral (B-) sites. The intensity ratio of the two lines

comprising each doublet (3-4, 2-5 and 1-6) was estimated to a value close to .60, giving evidence that the vacancies were entirely located at the B-sites. On the other hand, the isomer shift associated with the A-sites appears to be smaller than for the B-sites suggesting that covalent binding of the tetrahedral ions is larger than that of the octahedral ions, a result expected theoretically since the cation-oxygen distance is less for A-sites than for B-sites (Armstrong *et al.*, 1966).

On Mössbauer spectra for Fe_3O_4 , two superimposed sextets are also observable, however now a striking asymmetry appears between the shapes of the lines 1 and 6, and 2 and 5. This effect can be attributed to the presence in some B-sites (1:2 in stoichiometric magnetite) of Fe^{2+} ions affecting both the chemical shift and the hyperfine field. The A-sites line-width is temperature independent, whereas the B-sites line-width becomes temperature dependant above the Verwey temperature ($T_v \sim 120$ K). This phenomena which has been attributed to an electron exchange (referred as electron hopping) between Fe^{2+} and Fe^{3+} ions in the B-sites, has an associated relaxation time that can be estimated from the measured broadening and appears to be comparable at T_v to the Mössbauer characteristic time ($\tau \sim 10^{-8}$ s) (Sawatsky *et al.*, 1969; Kündig and Hargrove, 1969). Above this temperature, the measurement does not distinguish the Fe^{2+} from the Fe^{3+} ions located at the B-sites and both contributions average in a single broad peak.

For temperatures well above the blocking temperature, i.e. at which the particles are superparamagnetic, the maghemite spectrum resolves to a doublet, characteristic of a quadrupole splitting, while magnetite spectra show a single line with no apparent quadrupole splitting (Mørup *et al.*, 1976).

Composition	Mineral Name	Space Group	Dimensions (Å)	Z	Notes
Fe(OH) ₂		P3m1 hex.	a = 3.26 c = 4.596	1	CdI ₂ structure
variable	green rust I	R... hex.	a = 3.22, c = 24 (Cl) a = 3.18 c = 24.4-27.4 (SO ₄ ²⁻) c = 22.8 (Br)		9 layers of O
variable	green rust II	P... hex.	a = 3.17 c = 10.9		4 layers of O
α-FeOOH	Goethite	Pbnm orth.	a = 4.587 b = 9.937 c = 3.015	4	based on hcp. oxygen
β-FeOOH	Akaganeite	I4/m(?) tetra.	a = 10.48 c = 3.06	8	F or Cl necessary for formation α-MnO ₂ structure likely
γ-FeOOH	Lepidocrocite	Cmcm orth.	a = 3.87 b = 12.51 c = 3.06	4	based on ccp. oxygen
δ-FeOOH	Feroxyhite	P312 (?) hex.	a = 2.94 c = 4.58	1	hcp. oxygen disordered CdI ₂ structure
5Fe ₂ O ₃ ·9H ₂ O	Ferrihydrite	hex.	a = 5.08 ^(a) c = 9.4		
α-Fe ₂ O ₃	Haematite	R3c hex.	a = 5.0345 c = 13.749	6	hcp. oxygen with Fe ³⁺ in octahedral positions
Fe ₃ O ₄	Magnetite	Fm3d fcc	a = 8.3963	8	inverse spinel
γ-Fe ₂ O ₃	Maghemite	P4 ₃ 2 ₁ tetra.	a = 8.338 c = 3a	32	spinel - various degrees of ordering
FeO	Wüstite	Fm3m cub. tetra.	a = 4.302 (high Fe) a = 4.275 (low Fe) a = 6.04, c = 4.58	4 4 16	NaCl type " Martensitic transformation

Table 1. 2. Summary of the crystal structures of oxides and hydroxides of iron. ccp.: cubic close-packed; hcp.: hexagonally close-packed; hex.: hexagonal; orth.: orthogonal; tetr.: tetrahedral (Bernal *et al.*, 1959; (a) Towe and Bradley, 1967).

Compound	T _{NC} (°K)	ρ (g/cm ³)	K (J/m ³)	M _s (J/T/kg)	M _r /M _s	H _c (mT)	shape of particles	size (μm)
α-FeOOH	393.3		10 ^{3(a)}					
β-FeOOH	295							
γ-FeOOH	< 77							
δ-FeOOH	400	3.95 (bulk)		25 22		50	hexagonal platelets	~ .6 ~ .007
5Fe ₂ O ₃ ·9H ₂ O	< 77		10 ^{5(a)}					
α-Fe ₂ O ₃	956		10 ^{4(a)}					
Fe ₃ O ₄ - bulk - particles	858	5.197 4.9-5.1	10 ⁴ -10 ⁵	92 84	0.52 0.70 0.70	~ 30 30-34 35-45	equiaxial acicular platelets	1 .5x.1 1x.1x.02
γ-Fe ₂ O ₃ - bulk - particles	> 750	5.07 4.60	10 ⁴ -10 ⁵	74	0.46 0.80 0.75	7-15 25-37 32-38	equiaxial acicular platelets	.05-.3 .5x.1 1x.1x.02
FeO	198							

Table 1. 3. Magnetic properties of materials. T_{NC}: Néel/Curie temperature; ρ: density; K: typical anisotropy constant; M_s: saturation magnetization; M_r: remanence; H_c: coercivity (Bate, 1975; (a) Vandenberghe *et al.*, 1990).

Compound (-magnetic)	Site	Temperature (°K)	H (Tesla)	2ε (mm/s)	Δ (mm/s)	δ _{Fe} (mm/s)
Fe(OH) ₂	-	298	-		2.92	+1.18
α-FeOOH (antiferro-)	-	RT	38.1 ^(b)	-0.28	~0.55 fine particles	+0.61
β-FeOOH (antiferro-)	O ₃ (OH) ₃ coord. O ₂ (OH) ₄ coord.	RT	-	-	~0.95 ^(a) ~0.55	+0.39
γ-FeOOH (antiferro-)	-	295	-	-	0.55-0.7	+0.38
δ-FeOOH (ferri-)	-	RT	42.0	~1.0	~0.5	~+0.5 ^(c)
5Fe ₂ O ₃ ·9H ₂ O (spero-)	-		-	-	0.7-0.9 ^(a)	+0.38
α-Fe ₂ O ₃ (weakly ferri-)	-	296	51.7 ^(b)	-0.19	0.5-1.1 sizes < 8 nm	+0.39
Fe ₃ O ₄ (ferri-)	Fe ³⁺ (A) Fe ^{2+,3+} (B)	298	49.1 ^(b) 46.0	0 0	- -	+0.28 ^(b) +0.66
γ-Fe ₂ O ₃ (ferri-)	A B	300	50.2 50.3	- -	- -	
FeO	-	RT	-	-	0.8	+0.93

Table 1. 4. Mössbauer data at room temperature. H: hyperfine splitting; 2ε: quadrupole shift; Δ: quadrupole splitting; δ: isomer shift - (a) Bowen *et al.*, 1993; (b) Vandenberghe *et al.*, 1990; (c) Simmons and Leidheiser, 1976.

1. 2. 2. Synthesis

Sugimoto *et al.* (1980) report three basic different methods of magnetite preparation. First come the dry methods consisting of the oxidation of metallic iron by oxygen or other oxidizing agents, the disproportion of ferrous oxides, the reduction of ferric oxides or finally the decomposition of different ferric or ferrous salts. These processes usually require temperatures above 200°C. Second, magnetite can be prepared from stoichiometric mixtures of ferrous and ferric hydroxides in aqueous media. Finally, an aqueous suspension of ferrous hydroxide can be partially oxidized with different oxidizing agents.

This last method was investigated by Sugimoto *et al.* (1980): amorphous ferrous hydroxide was precipitated by aging in oxygen-free distilled water (DW) a solution of FeSO_4 with a mixture of KOH and KNO_3 as an oxidant. The mixture was then heated to 90°C and kept thermostatic and undisturbed for up to four hours. Ferrous hydroxide, originally a white precipitate, formed as a dark green precipitate in excess of FeSO_4 and light green in excess of KOH . This precipitate is assumed to be a mixture of $\text{Fe}(\text{OH})_2$ (eventually containing adsorbed oxygen) and green rust, which is the usual intermediate product in the formation of various iron oxides. Upon oxidation, this precipitate yielded magnetite particles whose size and shape depended on the experimental conditions.

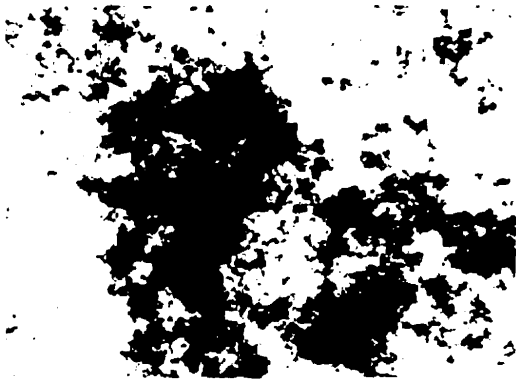
The ferrous ion concentration ($[\text{Fe}^{2+}]_{\text{xs}} = [\text{FeSO}_4] - \frac{1}{2}[\text{KOH}]$) was varied from zero to 0.3 mol/l. As it was increased, the particle at first became larger ($> 1 \mu\text{m}$) having a smooth spherical morphology, then for $[\text{Fe}^{2+}]_{\text{xs}}$ above ~ 0.1 mol/l, of smaller size ($\sim 0.4 \mu\text{m}$) with rougher spherical shapes. The excess hydroxide concentration ($[\text{OH}^-]_{\text{xs}} = [\text{KOH}] - 2[\text{FeSO}_4]$) ranged from 0 to 0.2

mol/l. The particle became of very small size (~ 10 nm) to increase slightly (~ 100 nm) with increasing $[\text{OH}^-]_{\text{ex}}$, assuming cubic shape.

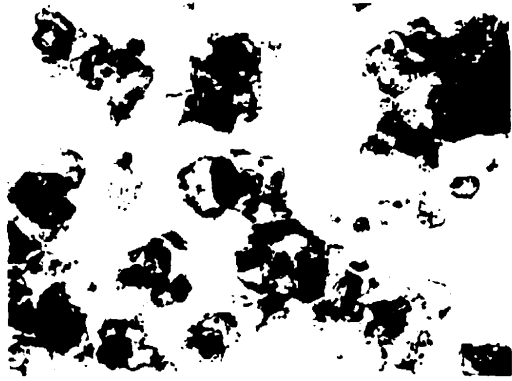
In order to determine the influence of the different anions or cations in solution, FeCl_2 , $\text{Fe}(\text{CH}_3\text{CO}_2)_2$ and $\text{Fe}(\text{NH}_4)_2(\text{SO}_4)_2$ salts were used instead of FeSO_4 . Precipitates formed from FeCl_2 solutions yielded magnetite particles with dimensions below 20 nm, regardless of $[\text{Fe}^{2+}]_{\text{ex}}$, while $\text{Fe}(\text{CH}_3\text{CO}_2)_2$ gave no discernible amounts of magnetite. When $\text{Fe}(\text{NH}_4)_2(\text{SO}_4)_2$ was used, particles of magnetite were obtained over a broad range of particle diameters. Setting the temperature to 80°C instead of 90°C gave crystals of approximately the same average diameter but of broader size distribution. Finally, increasing the amount of $\text{Fe}(\text{OH})_2$, although of little effect on the mean size of the particles, caused a broadening of the distribution.

On figure 1.6, transmission electron micrographs of the system were taken for increasing aging times. The $\text{Fe}(\text{OH})_2$, initially amorphous (a), starts to form hexagonal platelets after 15 minutes of aging at 90°C, while some rather small primary particles of magnetite can be detected mostly accumulated around these platelets (b). These primary particles of magnetite can be detected mostly accumulated around these platelets. These primary units then aggregate into larger magnetite particulate (c, arrow α) with subsequent growth by incorporation of these small particles into the larger ones (arrow β). After 45 minutes, only few platelets remain while the system consist essentially of very small and large magnetite particles (d). After two hours, only rather uniform, nearly spherical particles are present (e).

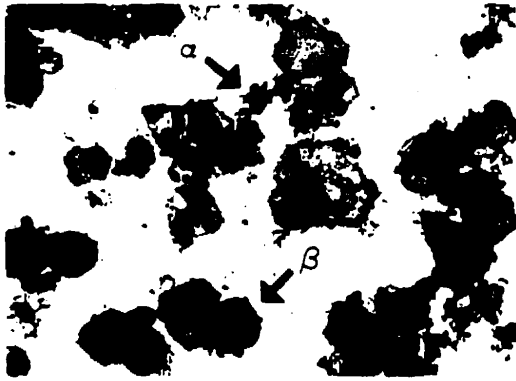
Figure 1. 6. Transmission electron micrographs of a system consisting of ferrous hydroxide and excess concentration of FeSO_4 aged at 90°C for (a) 0, (b) 15, (c) 30, (d) 45 and (e) 120 minutes (Sugimoto *et al.*, 1980).



a



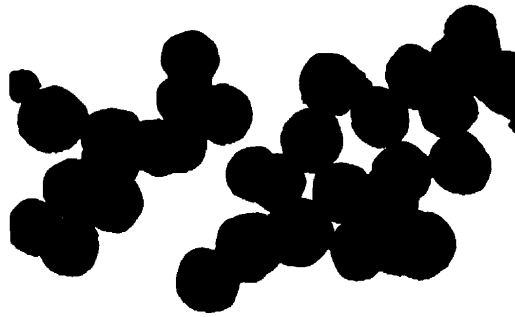
b



c



d



e

2 μ m

Kinetic measurements indicated the rate the rate of conversion of $\text{Fe}(\text{OH})_2$ into magnetite and the rate of growth of magnetite were significantly slower for high $[\text{Fe}^{2+}]_{\text{ex}}$ (0,3 mol/l) than for low $[\text{Fe}^{2+}]_{\text{ex}}$ (0.01 mol/l). When all $\text{Fe}(\text{OH})_2$ was converts, the pH dropped from 6 (high $[\text{Fe}^{2+}]_{\text{ex}}$) and 7 (low $[\text{Fe}^{2+}]_{\text{ex}}$) to 5. In high $[\text{OH}^-]_{\text{ex}}$ (0.2 mol/l), the pH stayed constant (~ 12) all through the experiment.

When air was present in addition to KNO_3 , two type of particles appeared: spheres of magnetite and rods, identified by X-ray analysis as goethite. The content of goethite was dependant on the excess concentration of Fe^{2+} species; it became smaller as the amount of free Fe^{2+} decreases while it was absent from systems having an excess of OH^- .

Two distinct mechanisms for the formation of magnetite are proposed by Sugimoto *et al.* (1980). The first, a direct crystallisation mechanism, takes place in excess OH^- solution, forming magnetite particles of cubic morphology. The second, a coagulation mechanism, is responsible for the formation of the large spheres: very small particles nucleated in the $\text{Fe}(\text{OH})_2$ gel, first aggregate resulting from Van der Waals and magnetic forces under the condition of weak repulsion and then the larger particles are formed by the contact-recrystallisation mechanism. Further growth occurs by adhesion of the additional primary particles to the already recrystallized spheres.

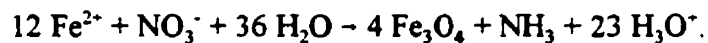
In the coagulation mechanism, there is a competition between the particle growth caused by adhesion of primary particles to already formed aggregates and the aggregation of the grown particles. When $[\text{Fe}^{2+}]_{\text{ex}}$ is increased, the rate of magnetite formation is reduced - probably due to complexation with sulfate ions - and simultaneous adhesion and coagulation of the smaller clusters into large particles may take place causing the broadening of the size distribution and the

roughness of the final magnetite particles. The aggregation is also affected by agitation, which causes a broadening of the size distribution.

The oxidation of $\text{Fe}(\text{OH})_2$ to magnetite by interaction with NO_3^- can be summarized as follows:



and for the corresponding oxidation of Fe^{2+} to magnetite in solution:



As a consequence, the pH remains unchanged or increases in the process involving $\text{Fe}(\text{OH})_2$, but always decreases in the reaction with Fe^{2+} solute species. In a first stage, the iron constituting the magnetite crystals must be mainly generated from the ferrous hydroxide gels. The pH then remains essentially constant or is slightly lowered while the amount of $\text{Fe}(\text{OH})_2$ keeps decreasing. Once most of the ferrous hydroxide has dissolved, the iron for the remaining increase in magnetite content must be supplied by solute complexes, resulting in decrease of pH.

The anions present in the solution have a dramatic effect on the size shape and composition of the products of ageing $\text{Fe}(\text{OH})_2$ gels. The decrease in the rate of magnetite formation as the excess of FeSO_4 in a given system increases is an example. As a general statement since ferrous and ferric ions form complexes with different ions, it is expected that the precipitation of iron containing oxides is affected by each of them in different ways.

Tamura *et al.* (1981) have also investigated the formation of magnetite and ferric oxides (goethite and lepidocrocite) from $\text{Fe}(\text{OH})_2$ suspensions (obtained from mixture of FeSO_4 and KOH) at pH 11.0 and 65°C . Figure 1.7 shows the time variation of the amount of Fe^{2+} (A), $\text{Fe}(\text{OH})_2$ (B), Fe_3O_4 (C) and ferric oxides (D) in the reaction suspension during the course of the air oxidation. In the early stage of the oxidation (region A-B), ferric oxides are formed while the rate of formation of magnetite is low. In the region B-C, magnetite formation increases rapidly simultaneously with a rapid decrease of ferric oxides and $\text{Fe}(\text{OH})_2$ phase suggesting that both are rapidly reacting to form magnetite phase. Following this phase (region C-D), the rate of magnetite formation becomes constant while the rate of oxidation of Fe^{2+} and that of the $\text{Fe}(\text{OH})_2$ consumption are both decreasing steadily in ratio 2/3 indicating the interaction to form a stoichiometric magnetite. At this stage, the amount of ferric oxide stays constant.

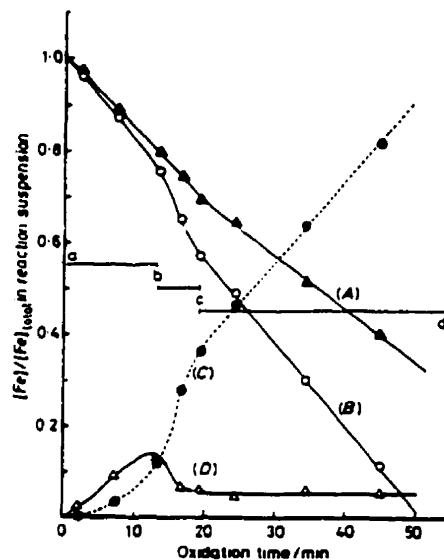


Figure 1. 7. Time variation of the amounts of products Fe_3O_4 (C) and Fe^{3+} oxides (D) and of $\text{Fe}(\text{OH})_2$ (B) and Fe^{2+} (A) in the reaction suspension during the course of the air oxidation (Tamura *et al.*, 1981).

Presence in the early stage (region a-b) of amorphous lepidocrocite, apparently soon transformed to goethite and magnetite, was established from IR spectra. In region b-c, the goethite bands intensities remained constant while the one corresponding to amorphous lepidocrocite decreased to completely disappear at the transition region c-d, suggesting that it was rapidly and preferentially transformed to magnetite in the reaction with Fe^{2+} derived from $\text{Fe}(\text{OH})_2$.

The measured oxidation rate in the stationary state (region c-d), could not be explained by the oxidation of Fe^{2+} dissolved in the reaction solution and was found to be determined by the oxidation of Fe^{2+} adsorbed on the solid phase and to be proportional to the fraction of the surface covered with oxygen. The resulting ferric precipitates have a high adsorption capacity for ferrous ions; they are thus assumed to combine as magnetite, the particles of which will hence grow in size.

Conditions for the formation of magnetite by air oxidation of $\text{Fe}(\text{OH})_2$ suspensions has also been studied by Kiyama (1974). The $\text{Fe}(\text{OH})_2$ suspension were obtained by adding various amounts of NaOH to FeSO_4 (0.72 mol/l). They were then quickly heated while N_2 was passed through the suspension, until the desired temperature was reached, and compressed air was substituted to N_2 . The R ($= 2[\text{NaOH}] / [\text{FeSO}_4]$) molar ratio and the temperature were kept respectively at 0.1 - 4.0 and at 5 - 85°C.

The mixing of FeSO_4 and NaOH solution resulted either as a neutral whitish suspension, for $R < 1$ (crystallising as ferrous basic sulfate for $R < 0.6$, otherwise amorphous) or an alkaline white precipitate consisting of fine crystal particles of $\text{Fe}(\text{OH})_2$ which size increased with

increasing R.

When R was below 0.6, oxidation of the whitish precipitate resulted in hexagonal particles of crystalline green rust II, irrespective of the oxidation temperature, leading further to the formation of spherical magnetite and a small amount of needle-like goethite particles at a pH 6.0 ± 0.5 . For R between 0.6 - 1.0, colloidal $\text{Fe}(\text{OH})_2$ would be present beside green rust II, the transformation to magnetite and goethite taking place at pH 7 - 9. The pH suddenly dropped below 4.5 at complete oxidation. On the other hand, alkaline $\text{Fe}(\text{OH})_2$ (for $R > 1$) resulted in octahedral and cubic particles.

For long oxidation times, magnetite was gradually oxidized to maghemite at 70 and 85°C, the black colour remaining until the ferrous ion content decreased to about 10% of the total iron ions. The oxidation in the suspension was found to proceed in proportion to the time indicating that the formation of magnetite took place in liquid phases of alkaline and neutral suspensions.

Ferrous ions supplied by the dissolution of the precipitates of $\text{Fe}(\text{OH})_2$ and green rust II react with the dissolved oxygen giving rise to the formation of a ferric hydroxo complex (polynuclear complex). Each particle of $\text{Fe}(\text{OH})_2$ or green rust II in the suspension might be surrounded by a thick dense layer of $\text{Fe}(\text{OH})^+$ ions that would coprecipitate with the ferric hydroxo complexes, forming magnetite. On the other hand, FeOOH may be formed outside the layer by the hydrolysis of the ferric hydroxo complexes.

Favourable conditions for the formation of magnetite include an increase in the surface area and volume of the layer. The rate of movement of green rust and $\text{Fe}(\text{OH})_2$ particles in suspension induced by the air flow was assumed to affect the surface area in the following way: too small flow rates (< 100 l/h) would encourage coagulation, while too great flow rates (> 400

l/h) would decrease the layer thickness, both effects leading to the decrease in the surface area.

Higher temperatures are believed to increase the layer thickness, promoting magnetite formation.

When FeCl_2 , FeBr_2 or FeI_2 were used instead of FeSO_4 , magnetite and lepidocrocite were formed *via* green rust I.

Taylor *et al.* (1974) have studied maghemite synthesis for a pH maintained either to 6 or 7, a temperature of 20, 30, occasionally 60°C, the $[\text{Fe}^{2+}]$ to $[\text{Fe}^{3+}]$ ratio, the total Fe concentration and the air flow being set to different values.

A mixture of Fe^{2+} and Fe^{3+} chloride in definite ratio, was dissolved in N_2 saturated DW, then oxidized with a measured air flow rate, the pH being maintained constant. The oxide was then centrifuged, washed, half of the sample being refluxed in boiling for about 16 hours before drying from acetone at 70°C, the second half dried without refluxing.

The colour of the initial precipitate varied from yellow-brown to green depending on the composition of the initial solution. The precipitate gave on oxidation an orange or dark brown product, respectively identified as lepidocrocite and maghemite.

The time curve of base consumption was used as a measure of the oxidation rate. On fast oxidation, usually leading at complete oxidation to lepidocrocite, the rate was constant, flattening off at the end. On slow oxidation, the rate became slower at first until an inflexion point was reached, the rate becoming constant. The product at the inflexion point was identified as green rust I.

These results lead to the conclusion that maghemite formation was favoured by lower oxidation rates, higher total iron concentrations, higher pH (7 against 6) and within certain limits

by the presence of some Fe^{3+} in the original solution.

Green rust appears to be a necessary precursor of maghemite, and must undergo dehydration before further oxidation if maghemite is to form. This topotactic two phase reaction leads to a cubic lattice and is the more favoured the slower the oxidation proceeds because then a green rust with a low Fe^{3+} content is being formed as the precursor of the cubic phase. This cubic phase probably occurs first as magnetite, the further oxidation of which yields maghemite by a topotactic reaction. The complete oxidation appears to be extremely difficult at room temperature, and was favoured here by the low pH used and small particle size.

On fast oxidation, the proportion of Fe^{3+} in green rust will increase rapidly leading to complete oxidation before a dehydrated cubic phase can be formed. The final product is lepidocrocite.

Ferrihydrite eventually occurs as a Fe^{3+} phase formed by direct precipitation when Fe^{2+} ions are in too low concentration to exceed the solubility product of green rust. Goethite is assumed to form simultaneously with lepidocrocite due to the presence of CO_2 from the ageing of ferrihydrite.

Shermann *et al.* (1976) investigated the influence of $[\text{Fe}^{2+}]$ and pH on the formation of magnetite, lepidocrocite and ferrihydrite from oxidation of $\text{Fe}(\text{OH})_2$ solutions. Crystals of $\text{FeCl}_2 \cdot 4\text{H}_2\text{O}$ were dissolved in different proportions into N_2 saturated DW, the pH was adjusted and oxidation commenced by bubbling O_2 freed from CO_2 through the solution. During the oxidation, the pH was kept constant with a NH_3 solution, using an automatic titrimeter; once the oxidation complete (no further drop of pH), the oxide was centrifuged, washed with water and

acetone until free of chloride and dried at 40°C.

At a pH of 7.0, lepidocrocite was the only crystalline compound formed for $[\text{Fe}^{2+}]$ concentrations below 0.15 mol/l, while up to about 40% magnetite was formed at higher concentrations.

Lepidocrocite was formed as lath-shaped crystals, whose morphology and particle size were found pH dependant through its effect on the oxidation rate. At pH 6.5 and 7.0, faster oxidation led to finger-like thin bendable extensions in the c direction of the lath, while for lower pH, smaller sized crystals appeared, along with very small spherical particles at pH 4.5 about 4 nm in size partly linked to linear arrays, probably consisting of ferrihydrite.

It is generally agreed that lepidocrocite formation requires presence of Fe^{2+} as it almost exclusively occurs in soils in which anaerobic conditions lead to the formation of Fe^{2+} . In similar systems as the one used here, the necessary precursor of lepidocrocite is not $\text{Fe}(\text{OH})_2$, but the blue-green mixed Fe(II,III) hydroxide, green rust, believed to form through the reaction of Fe^{2+} ions with ferrihydrite or its precursor and stable at much lower pH than $\text{Fe}(\text{OH})_2$. On oxidation, green rust leads to lepidocrocite or maghemite depending on whether the oxidation rate is high or low respectively. As the oxidation rate depends on the O_2 supplied in relation to the amount of green rust formed in the system, at the relative large supply used here, maghemite can only be formed if a relatively large amount of green rust is precipitated, *i.e.* $[\text{Fe}^{2+}]$ and pH are relatively high. Inversely, at a particularly low ratio oxygen supplied to green rust formed, *i.e.* at low $[\text{Fe}^{2+}]$ and low pH, ferrihydrite replaces lepidocrocite: the solubility product of green rust is no longer exceeded but only that of ferrihydrite, thus Fe^{2+} oxidizes in solution rather than after precipitation as green rust, and precipitate immediately as ferrihydrite.

The solubility products of iron hydroxides are reported by Bernal *et al.* (1959) as $[\text{Fe}^{2+}][\text{OH}^-] = 1.6 \times 10^{-14}$ and $[\text{Fe}^{3+}][\text{OH}^-] = 1.1 \times 10^{-36}$. Thus in strong alkali, the concentration of both Fe^{2+} and Fe^{3+} are extremely small (respectively $\sim 10^{-14}$ g-ions/l and 10^{-36} g-ions/l). Solid $\text{Fe}(\text{OH})_2$ is stable and on rapid oxidation is first oxidized up to about 20% Fe^{3+} content, then its structure becoming unstable, gives ferroxhyte. On slow oxidation by oxygen dissolved in the solution, a ferric oxihydroxide (goethite is the normal hydrolysis product of ferric salt) is nucleated afresh from oxidized Fe^{2+} ions in solution. The $\text{Fe}(\text{OH})_2$ solid on slow oxidation, is no longer directly oxidized, but remains in equilibrium with the solution, supplying fresh Fe^{2+} as they are removed by oxidation and precipitation.

In neutral solution, solid $\text{Fe}(\text{OH})_2$ will be in equilibrium with a high concentration ($\sim 1 \text{ N}$) of Fe^{2+} which on slow oxidation will transform to Fe^{3+} , both ions combining in a ferroso-ferric phase of possible composition $\text{Fe}^{2+} \cdot 2\text{Fe}^{3+}(\text{OH})_4$. This hydroxide must be presumed to convert into magnetite on heating to 100°C in water. If oxidation takes place before dehydration, this green complex must transform to lepidocrocite.

The previously described chemical processes all took place in bulk solution. The effect of confining these reactions in nano-sized voids has been investigated by Mann and Hannington (1988). Iron oxides (in the form of goethite, ferrihydrite and magnetite) in the size range of 2 to 10 nm, have been precipitated in phospholipid vesicles, used as membrane bound compartments enclosing an internal aqueous volume of diameter *ca.* 20 - 30 nm. The vesicles were dispersed in solutions containing Fe^{2+} ions (freshly prepared from $\text{FeCl}_2 \cdot 4\text{H}_2\text{O}$ or occasionally $\text{FeSO}_4 \cdot 7\text{H}_2\text{O}$), Fe^{3+} ions (freshly prepared from FeCl_3 or $\text{Fe}(\text{NO}_3)_3$), or $\text{Fe}^{2+} / \text{Fe}^{3+}$ ions in 1:1 ratio. The ferrous

and ferric ions not encapsulated within the unilamellar vesicles were removed and precipitation of entrapped ferrous or ferric ions was induced by the addition of aqueous NaOH (pH ~ 12) or NH₃ (pH ~ 10.5). A pale yellow colour then appeared developing in intensity over several days.

Precipitation of intravesicular ferric ions after addition of NaOH resulted in the formation of discrete, finely divided spherical or disk-shaped electron-dense particles - although some elongated particles were observed, the size of which after 30 minutes ranged 1.5 to 5 nm - giving on electron diffraction diffuse patterns with d-spacings corresponding to poorly oriented goethite (presence of haemetite or akaganeite, whose presence would have given similar d-spacings was unlikely, as these materials only form at temperatures around 200°C).

Precipitation of intravesicular ferrous ions after the addition of NaOH, resulted in the formation of discrete spherical electron-dense particles (with mean size after 30 minutes of 4.2 nm with NaOH and 2.6 nm with NH₄OH), giving strong electron diffraction patterns corresponding to magnetite.

Finally, precipitation of intravesicular ferrous / ferric ions after addition of NaOH resulted in spherical discrete particles of low electron density identified from electron diffraction patterns as poorly ordered ferrihydrite.

When precipitated under identical starting conditions but in the absence of vesicle, ferric solutions resulted in extended aggregates of ferrihydrite formation, ferrous solutions in acicular needles of both lepidocrocite and goethite, while ferrous / ferric solution gave irregular-shaped 10 to 50 nm magnetite particles.

The difference in structure, morphology, and particle size can be attributed to kinetic control exerted by the vesicle membrane on the rate of OH⁻ diffusion into the intra-vesicular

space, favouring the formation of thermodynamically stable products such as intra-vesicular goethite from ferric solution instead of ferrihydrite, formed under conditions of rapid precipitation. Similarly, magnetite would result from intra-vesicular precipitation of ferrous ions, as the slow oxidation rate resulting from the slow diffusion of OH^- favours the formation of mixed valence oxides rather than the hydrous ferric oxides such as goethite and lepidocrocite which are formed by rapid oxidation in bulk solution. For ferrous / ferric solution, the slow increase in intravesicular OH^- favours the preferential precipitation of the ferrous component such that the required ferrous / ferric activity ratio for magnetite is never attained. In bulk solution, rapid precipitation results in the formation of mixed valence green rust which subsequently transforms to magnetite.

The various experiments reported here, suggest mechanisms for the formation of different iron oxides from aqueous solutions of ferrous (and ferric) ions in alkaline or neutral medium. In alkali medium, a white ferrous hydroxide precipitate generally forms. Upon rapid oxidation $\text{Fe}(\text{OH})_2$ transforms to ferrihydrite or ferrihydrite by solid recrystallisation whereas upon slow oxidation, it supplies ferrous ions, some oxidized in solution as ferric ions which precipitate to form ferric oxihydroxide, or both ions combining to form magnetite. In a neutral medium, ferrous ions in high concentration, oxidize partly to ferric ions, both combining to form green rust, subsequently oxidized to either magnetite (slow oxidation) or lepidocrocite (fast oxidation).

High temperatures generally favour the formation of magnetite by accelerating the dehydration of its precursors. Slower dehydration must be compensated by slower oxidation.

The cations in presence is determinant, since solutions containing SO_4^{2-} seemed to yield

green rust II, oxidizing to magnetite / goethite, while solutions containing Cl^- produced green rust I, which oxidized to magnetite / lepidocrocite.

Finally, enclosing the ferrous ions inside intravesicular space, favours their precipitation as thermodynamically stable compounds due to the low diffusion rate of OH^- through the membranes.

1. 3. References

- Armstrong, R.J., Morrish, A.H., Sawatsky, G.A. (1966) *Phys. Letters* **23**, 414.
- Bate, G. (1975) in *Magnetic Oxides* (D.J. Craik, ed). London: J. Wiley & sons, p. 689.
- Bean, C. P. and Livingston, J. P. (1959) *J. Appl. Phys.*, **30**, 120S.
- Bernal, J.D., Dasgupta, D.R., and Mackay, A.L. (1959) *Clay Min. Bull.*, **4**, 15.
- Bowen, L., De Grave, E., Vandenberghe, R. E. (1993) in *Mössbauer spectroscopy applied to magnetism and material science* (G. J. Long, F. Grandjean, eds.). New York: Plenum Press, p. 115.
- Craik, D.J. (1975) in *Magnetic Oxides* (D.J. Craik, ed). London: J. Wiley & sons, p. 1.
- Crangle, J. (1977) *The Magnetic Properties of Solids*. London: Edward Arnold, Ltd, p. 110.
- Dickson, D.P.E., Reid, N.M.K., Hunt, C., Williams, H.D., ElHito, M. and O'Grady, K. (1993) *J. Magn. Magn. Mater.*, **125**, 345.
- Dormann, J. L. (1981) *Revue Phys. Appl.*, **16**, 275.
- Francombe, M.H. and Rooksky, H.P. (1959) *Clay Min. Bull.*, **4**, 1.
- Kiyama, M. (1974) *Bull. Chem. Soc, Jap.*, **47**, 1646.
- Kündig, W., Hargrove, R.S. (1969) *solid state comm.* **7**, 223.
- Leslie-Pelecky, D.L. and Reike, R.D. (1996) *Chem. Mater.*, **8**, 1770.
- Mann, S. and Hannington, J.P. (1988) *J. Coll. Int. Sci.*, **122**, 326.
- Mørup, S., Topsøe, H., Lipka, J. (1976) *Jour. Phys. - Coll. C6*, **T. 37**, C6-287.
- Pankhurst, Q. A. and Pollard, R. J. (1993) in *Mössbauer spectroscopy applied to magnetism and material science* (G. J. Long, F. Grandjean, eds.). New York: Plenum Press, p. 77.

- Powers, D.A. (1975) *Magnetic Behaviour of Basic Iron (III) Compounds*, Ph.D. Thesis, California Institute of Technology, Pasadena, California.
- Sawatsky, G.A., Coey, J.M.D., Morrish, A.H. (1969) *J. Appl. Phys.* **40**, 1402.
- Schwertmann, U. And Thalmann, H. (1976) *Clay Minerals*, **11**, 189.
- Simmons, G.W. and Leidheiser, H., Jr. (1976) in *Applications of Mössbauer Spectroscopy - volume I* (R.L. Cohen ed.). New York: Academic Press, p. 85.
- Sohoo, R.F. (1960) in *Theory and application of ferrites* (W.L. Everitt ed.). Prentice-Hall.
- Sugimoto, T. And Matijević, E. (1980) *J. Coll. Int. Sci.*, **74**, 227.
- Taylor, R.M. and Schwertmann, U. (1974) *Clay Minerals*, **10**, 299.
- Tamura, Y., Buduan, P.V. and Katsura, T. (1981) *J. Chem. Soc. Dalton Trans.*, 1807.
- Tamura, Y., Ito, K., and Katsura, T. (1983) *J. Chem. Soc. Dalton Trans.*, 189.
- Towe, K.M. and Bradley, W.F. (1967) *J. Coll. Int. Sci.*, **24**, 384.
- Vanderberghe, R.E., De Grave, E., Landuydt, C. and Bowen, L.H. (1990) *Hyperfine Interactions*, **53**, 175.
- Whitesides, G. M., Kazlauskas and R. J., Josephson, L. (1983) *Trends in Biotechnology*, **1(5)**, 144.
- Zachariah, M.R., McMillin, B.K., Shull, R. D. (1995) in *ACS Polymeric Material Science and Engineering*, **13**, Fall meeting 1995, Chicago, 35.
- Ziolo, R.F., Giannelis, E.P., Weinstein, B.A., O'Horo, M.P., Ganguly, B.N., Mehrotra, V., Russell, M.W. and Huffman, D.R. (1992) *Science*, **257**, 219.

CHAPTER II - MATERIALS AND CHARACTERIZATION METHODS: GENERAL DESCRIPTION

2. 1. Materials

2. 1. 1. Bacterial cellulose (BC)

Bacterial cellulose (BC) was synthesised by *Acetobacter Xylinum* as a thin membrane (~ 2 mm) at the surface of the culture medium, in static conditions, or as a suspension of fine pellets, under stirring conditions. The bacterial cellulose gel protects *in vivo* bacteria against virus contamination. The basic element is a 5 - 10 nm wide microfibril with multiple branching.

Each bacterium has at its surface a series of fine pores which excrete the cellulose microfibrils, bunching into slender fibrils of about 50 nm wide and at least 10 μ m long (Yamanaka *et al.*, 1989). Following the cell division, the microfibrils of parent cells will be inherited one-half by each of the daughter cells, forming a branching point on the fibril. The fibril diameter, narrower right after the cell division recovers as the new cell matures. The repetition of this process generates the branching cascade which appears as crosslinks between the fibrils.

The crystallographic form of this cellulose is cellulose I_α, commonly found in vegetable cellulose (the X-ray crystallinity was reported to be ~ 71%, *i.e.* several per cent higher than cotton or wood pulp). The molecular orientation is parallel to the direction of the length of the fibril.

Upon drying, the bacterial cellulose gel membrane forms a parchment whose fibrils can be

directionally oriented parallel to the shrinkage direction or the stretching direction. The Young modulus can then be as high as > 15 GPa across the plane of the parchment, which is much higher than those of other films based on organic polymers (< 10 GPa)¹. This is due to the higher density of interfibrillar hydrogen bonds formed on drying finer fibrils providing a larger contact area.

Due to its unique mechanical behaviour, BC parchment finds applications in acoustic membranes (due to its high Young modulus comparable to aluminium or titanium associated with a lightness, sound propagation speed and internal dispersion comparable to paper). Health care applications are medical bandages, or biological substrates for the culture of mammal cells.

When grown under stirred conditions, the microscopic fibrillar structure of bacterial cellulose remains unchanged, whereas on a macroscopic scale, the fibrils instead of forming a gel membrane, aggregate as a suspension of irregular pellets. These aggregates are due to entanglements of cells and fibrils to form a unit which allows an equilibrium oxygen content throughout the reactor space. Most of the physico-chemical properties are altered under stirring conditions as compared to static conditions (table 2.1). However, the BC prepared in the form of a suspension seems more appropriate for obtaining a uniform chemical treatment, for *in situ* synthesis, as it provides better accessibility of microfibrils to the reactants.

¹Nissan (1976) calculated a modulus of ~ 10 GPa for hydrogen bonded cellulose crystallites.

culture conditions	Static	Stirred
Degree of polymerization	15500	11200
Index of crystallinity (%)	71.0	63.4
Cellulose Iα (%)	73.	61.
Crystallite size (nm)	7.4	6.9
Young Modulus (GPa)	33.3	28.3

Table 2. 1. Structure and physico-chemical properties of bacterial cellulose under static or stirred culture conditions (Watanabe and Yamanaka, 1994).

Bacterial cellulose grown under stirring conditions has applications as a strengthening agent in composite materials, in association with other types of cellulose (*e.g.* cotton lint or wood pulp), carbon fibres, resins or SiC whiskers. The strengthening effect is due to the relatively low cross-section of the fibrils which provide a high density of potential hydrogen bonding resulting in stronger cohesion. Improvement in retention for some additives used in paper-making is yet another application. All of these applications depend on the never-dried state of the purified bacterial cellulose since air-drying of bacterial cellulose leads to irreversible consolidation (hornification). Solvent exchange drying or freeze drying will diminish interfibril hydrogen-bonding (Marchessault, 1977).

2. 1. 2. Lyocell

N-methylmorpholine-N-oxide (NMMO - figure 2.1), was first described as a solvent for cellulose (Johnson, 1969). Its potential for wet-spinning cellulose fibres is described in a patent by Mc Corsley patent. Encouraged by environmental drawbacks related to the viscose process and the promising development of these newer cellulose solvents, systematic search for a new fibre process started in the late 70's. By 1980, NMMO was shown to be the best solvent for that purpose; it offered the advantage of being recyclable at a high level of efficiency, while being able to dissolve cellulose completely without reacting with it or degrading it, the resulting process being less energetically intensive than the viscose route, already less energetically intensive than the synthetics (Wooding, 1993).

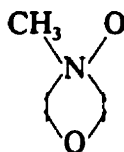


Figure 2. 1. N-methylmorpholine-N-oxide (NMMO).

This process is used by Courtaulds to produce Tencel, a fibre stronger than any other manmade cellulosic, especially when wet, and which processed into yarn and fabrics offers unique properties. The Courtaulds semi-commercial production synthesis, is illustrated in figure 2.2. Dissolving-grade wood-pulp mixed into a paste with NMMO passes through a high temperature dissolving unit to yield a clear viscous solution. This is filtered and spun into dilute NMMO

whereupon the cellulose fibres precipitate. These are washed and dried, and finally baled as staple or tow products as recovery systems concentrate the NMMO to the level required for reuse in dissolution.

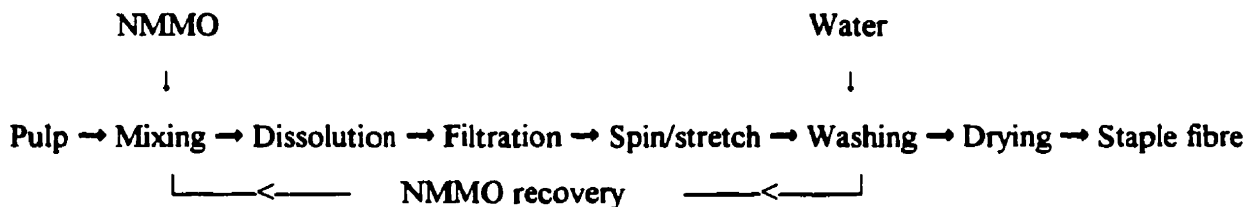


Figure 2. 2. Direct dissolution: Courtaulds Tencel process.

The same principle used in the above process applies for casting Lyocell membranes in a laboratory (Chanzy, 1997 - private communication):

We use the 50% water solution from Aldrich Chemical and with it make a 5% cellulose suspension and fill a round bottom flask which connects to a rotating evaporator system connected to a vacuum source. The evaporator bath should contain silicone oil and usually it is best to work with a 2 litre flask and approximately 100 to 200 cc of solvent. We start the process at 80-100°C and the solution will thicken and eventually a skin will form. This viscous skin should be examined in a polarizing microscope for evidence that all cellulose fibres have dissolved. We keep heating until about 110° then continue heating without vacuum up to 130° for 5 to 10 minutes. The homogeneous solution should be in the bottom of the flask as an amber colour solution ready to be spread on a preheated glass plate and cast to a pure cellulose film in a 65° water bath.

2. 2. Characterization methods

2. 2. 1. Transmission electron microscopy

In a transmission electron microscope (TEM), the electrons produced at the level of the illumination system, reach the fluorescent screen or photographic plate after travelling along the optical axis of the microscope column. Along the way, they interact with the electronic population of the specimen (being absorbed and diffracted) and with the magnetic field produced by several electromagnetic coils (being deflected). These coils may be elements of magnetic lenses, deflection coils or stigmators, themselves organized in optical systems constituting the optics of the TEM (figure 2.3).

Due to its versatility, the TEM provides different using modes, amongst which bright field or dark field imaging (in high (HM) or low (LM) magnification), diffraction and low dose are the most commonly used.

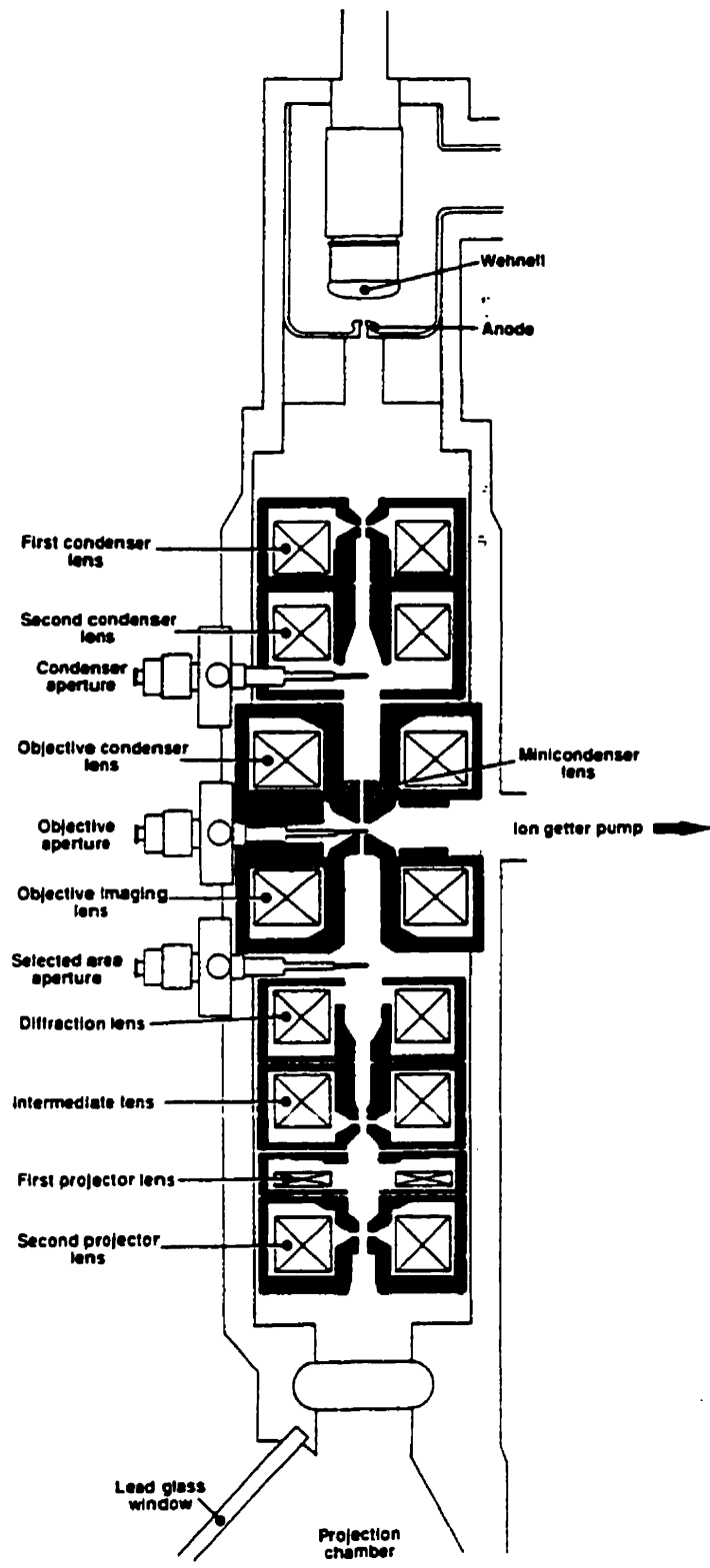


Figure 2. 3. Cross section of the electron optical column.

2. 2. 1. 1. Electron optic elements

Magnetic lenses

A vortex field generated by the current passing through the coils, catches the electrons which pass the lens, deflecting them to the optical axis (figure 2.4). As they escape from the lens field, the electron have been rotated around the axis by $\phi = NI / \sqrt{V} \times 18.6 \times 10^{-2}$ rad (N is the number of turns of the coil, I is the current running through it and V is the high tension of the microscope). Polepieces surrounding the lens coils are used to concentrate the magnetic field. Since the focal length can be changed simply by changing the current, adjustment of the lens system (focussing, magnification...) is possible without any mechanical change.

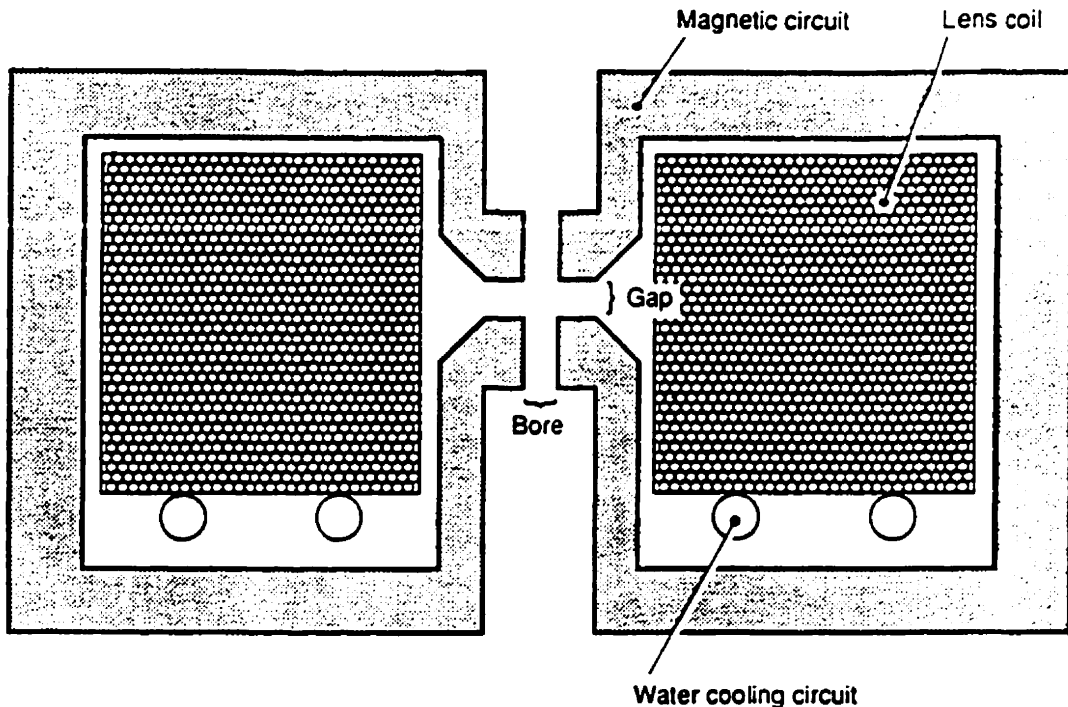


Figure 2. 4. Schematic cross section of an electromagnetic lens.

Deflection coils

To deflect the electron beam, two coils with currents running in the same direction, are positioned on both sides of the beam, producing a magnetic field perpendicular to it (figure 2.5). Using two pairs of coils below each other permits to position the pivot or tilt the electron beam at a point which is not accessible for deflection coils.

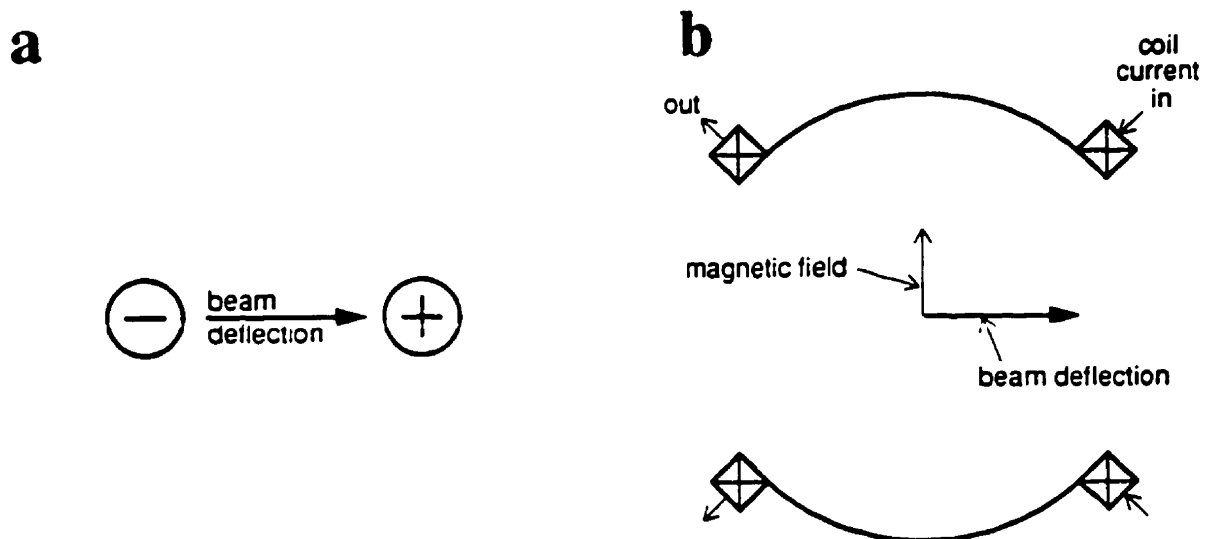


Figure 2. 5. (a) general principle of a beam deflector; (b) actual design of the microscope's deflection system (the currents through the coils are shown by the arrows: in = into the paper, out = out of the paper).

Stigmator

The stigmators press from both opposite sides to the beam, and pull it at both sides in the perpendicular direction. In order to correct the astigmatism in all direction, two sets of four coils (one rotated over 45° with respect to the other) must be used, opposite coils, unlike deflections coils, having a reversed current.

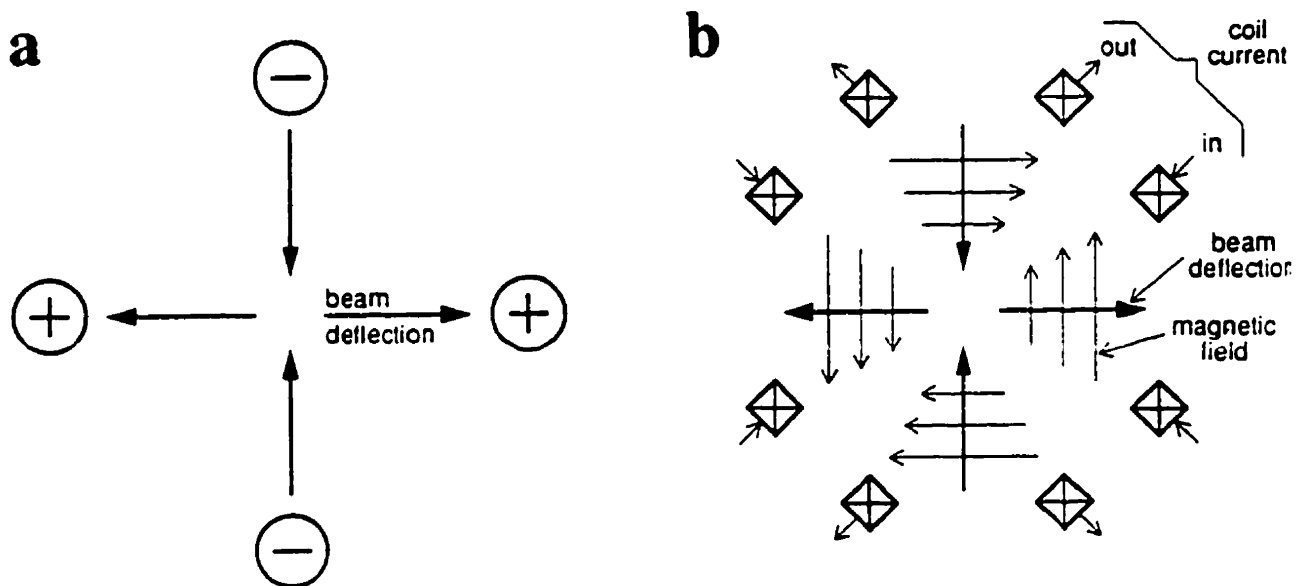


Figure 2. 5. (a) general principle of a stigmator; (b) actual design of the stigmator as used in the microscope (the currents through the coils are shown by the arrows: in = into the paper, out = out of the paper).

2. 2. 1. 2. The optics of a TEM

The illumination system

The electron source is usually a thermionic gun: a tungsten (W), lanthanum-hexaboride (LaB_6) or cerium-hexaboride (CeB_6) hairpin filament is heated just below its melting point, allowing the electrons to be relatively easily pulled out by applying an external electrostatic field (Coulomb force). The filament is put at a negative high tension (cathode), and faced to a plate with a hole put at zero potential (anode), which attracts the electrons from the hot surface of the filament. A third electrode (Wehnelt cylinder), positioned in front of the filament and put at a slightly more negative potential (~ 100 V) deflects the beam to a small cross over (virtual source, ~ 50 to 100 μm across) between Wehnelt and anode (figure 2.6).

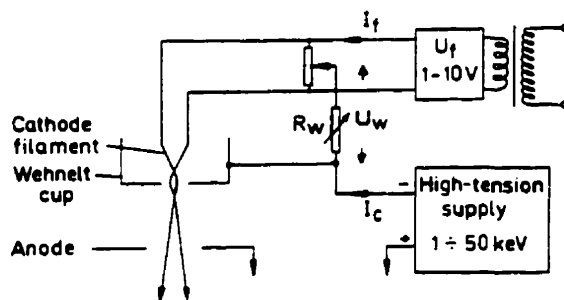


Figure 2. 6. The triode electron-source.

A first condenser lens, C_1 , determines the demagnification (size reduction) of the electron source onto the specimen and thus the spot size. The second condenser, C_2 , determines how strongly the beam is focused on the specimen, varying the intensity of the beam on the viewing screen. An aperture inside the C_2 lens is used as a beam defining aperture.

The objective lens

The objective lens forms the first intermediate image (magnified between 20 and 50 times) of the object, enlarged downward by the imaging lens system. As effects of its errors would also be enlarged, this lens is the most critical in the microscope. The diffraction pattern forms at the back focal plane where the objective diaphragm is positioned, whereas the first intermediate image is formed at "the selected area plane" where the selected area (SA) diaphragm is present.

The objective lens in the Philips' CM series microscopes, consists of two lens coils and two pole pieces on each side of the specimen which although producing a single magnetic field can be thought as two lenses: the pre-field or objective-condenser above the specimen and the objective-imaging field below. The TWIN-lens used in CM series microscopes, use a symmetrical condenser-objective lens design which allows the reduction of the gap between the two objective pole pieces (reducing spherical and chromatic aberrations) while retaining high tilt ability, the slow change in the lens parameters away from the centre, the large diffraction angle and the provision of small spot sizes. The limited spread of the beam inherent to such design is corrected by the insertion of a minicondenser lens into the upper pole piece. This lens is switched "optically" on if a wide field of view and coherent illumination on the specimen is required (microprobe mode) or

switched “optically” off (in fact reversing the current direction running through the lens coil)
 when small spot sizes are required (nanoprobe mode) (figure 2.7).

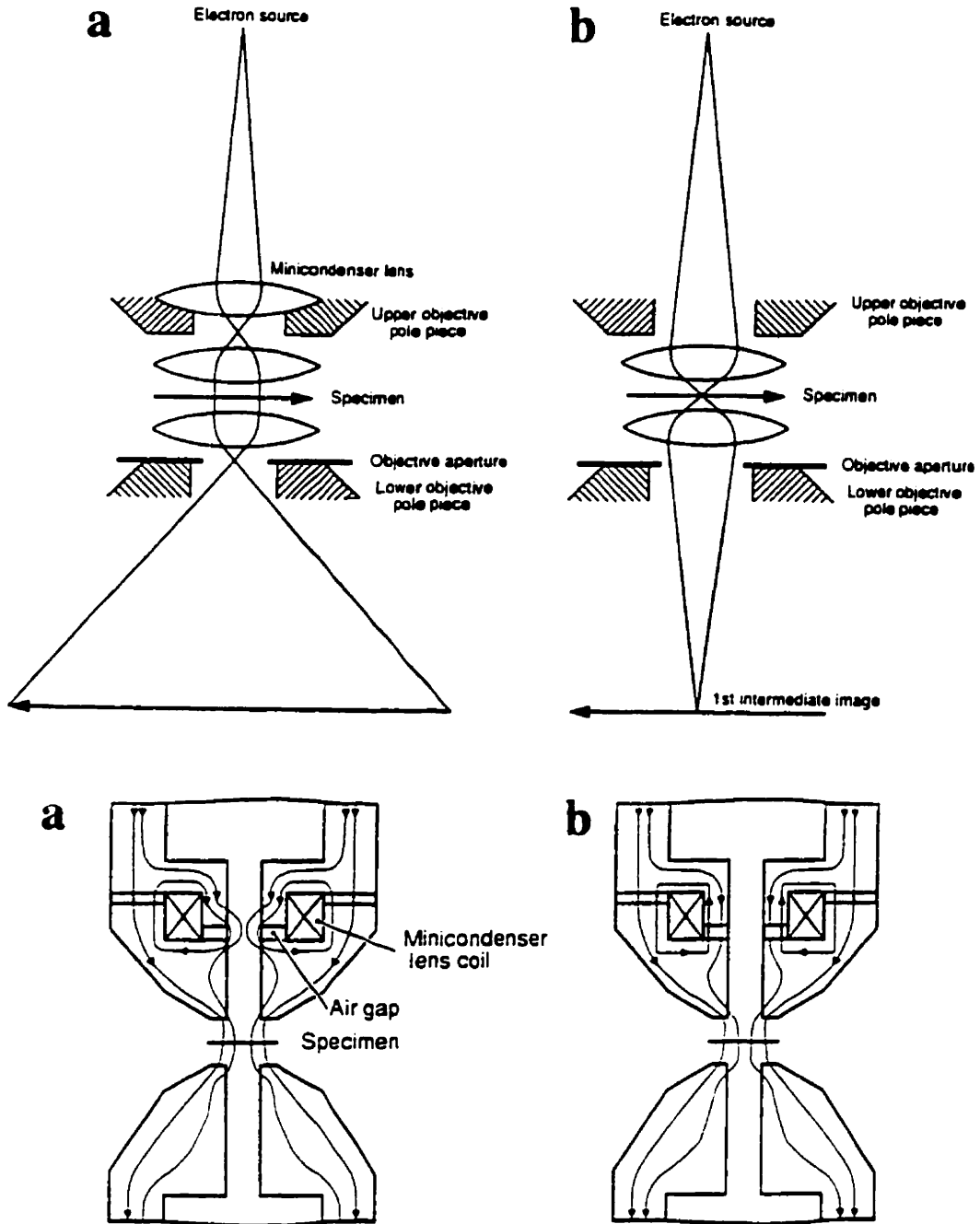


Figure 2. 7. The TWIN lens (a) microprobe and (b) nanoprobe modes.

The imaging lens system

This system includes in addition to the objective lens reviewed in the previous paragraph, a diffraction lens, an intermediate lens, and two projector lenses. Figure 2.8 shows the lens current as a function of the image magnification for a typical CM microscope. General trends are the gradual increase of the strength of the intermediate lens and the - somewhat more erratic - decrease in the first projector lens. The second projector lens is used to focus the final cross-over exactly in the plane of the differential pumping aperture that separate the microscope column vacuum volume from the projection chamber.

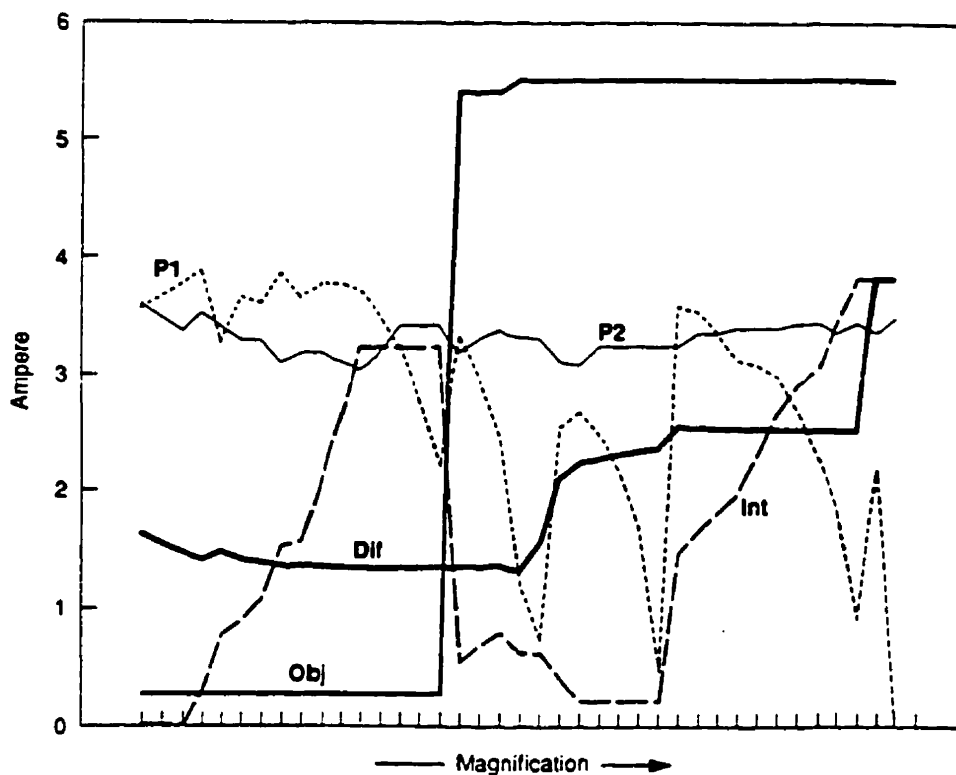


Figure 2. 8. Graph showing the change in the currents through the lenses of the magnification system of a CM20 as a function of magnification.

2. 2. 1. 3. TEM modes

Bright field imaging

In high magnification (HM), the beam made parallel by the mini-condenser illuminates the sample, forming on the back focal plane of the objective lens the diffraction pattern. The objective aperture is then centred on the central spot, to eliminate from the beam the electrons diffracted beyond a certain angle, hence providing a diffraction contrast in addition to the absorption contrast.

In this mode, the object plane of the magnification system is automatically positioned in the SA plane of the objective lens, the focussing being then performed by adjusting the objective lens current in order to position the first intermediate image in that plane.

Whereas in high magnification (HM) mode the objective lens is used for focusing the image, in low magnification (LM) mode, since broad illumination of the specimen is required, the objective lens is nearly switched off and the focussing made by the diffraction lens. Diffraction contrast is now provided by inserting the SA aperture in the SA plane where the diffraction pattern is situated. The function of the objective and diffraction lenses, their associated stigmator and apertures in HM and LM are compared in table 2.2.

	High magnification	Low magnification
Objective lens	Image focus	Diffraction (LAD) focus
Diffraction lens	Diffraction focus	Image focus
Objective aperture	Contrast forming	Area limiting
SA aperture	Area limiting	Contrast forming
Objective stigmator	Image stigmator	Diffraction stigmator
Diffraction stigmator	Diffraction stigmator	Image stigmator

Table 2. 2. Lens and aperture functions in HM and LM.

Diffraction

All electrons which are diffracted over the same angle will be focussed at the same position in the back focal plane of the objective lens. The distance R from the central transmitted spot to a specific diffracted spot is related to a characteristic spacing d between crystallographic planes in the specimen by $d = L\lambda / R$, where L is the camera length and λ , the relativistic electron wave length is calculated from the electron accelerating voltage E by

$$\lambda = h / mv = 12.27 / \sqrt{E \times [1 + 0.978 \times 10^{-6} E]^{-1/2}} \quad (\text{Dorset, 1995}).$$

(i) *Selected area diffraction.* A diffraction pattern can be obtained by illuminating the specimen with a parallel beam (microprobe with over-focussed C_2) and focussing the diffraction lens onto the back focal plane of the objective lens. Introducing the SA aperture in the first

intermediate image in the SA plane allows to limit the diffracting area of the specimen down to $0.4 \mu\text{m}$ (for an objective lens magnification of 25 times and a SA aperture of $10 \mu\text{m}$).

(ii) Micro-diffraction. In microprobe mode, a spot size down to 40 nm can be focused on the specimen by adjusting the C_2 intensity. Only the very small illuminated area will contribute to the diffraction pattern consisting then of broad spots instead of points due to the larger convergence of the incident beam.

(iii) Micro-micro diffraction. In nanoprobe mode, the spot size can be reduced down to 2 nm. The diffraction pattern consists then of large discs.

Dark field imaging

If an aperture is used to stop the transmitted beam, selecting only scattered electrons, a dark field image is obtained. Amongst the advantages of this mode are the simplification of the image by selecting a specific diffraction spot, the contrast improvement and provision of additional information and the aid to the interpretation of diffraction patterns.

A dark field image can be obtained either by displacing the objective aperture to a diffracted spot in the diffraction pattern or tilting the incident beam while keeping the aperture on the optical axis.

Low dose mode

In order to reduce the beam damage on very sensitive materials (*e.g.* negatively stained materials, organic crystals, or frozen sections), the following methods may be used: lower beam intensity by either over-focusing C_2 lens or choosing smaller spotsize and smaller aperture, a TV system being useful to improve the image intensity; lower the specimen temperature by using a cryostat. A Low Dose technique may also be used: the area of interest of the specimen is looked for at low magnification (low intensity - SEARCH state), the focusing, astigmatism corrections and other image optimizations are then performed at high magnification (high intensity) at an off-axis part of the specimen (FOCUS state), and finally a micrograph of the axial area, illuminated only during the exposition time, is taken (EXPOSURE state).

2. 2. 1. 4. Sample preparation

Embedding

The membranes were prepared by successive solvent exchange first with ethanol and propylene oxide, then with mixtures of 25% / 75%, 50% / 50%, 75% / 25%, 100% / 0% (twice) of Spurr resin / propylene oxide. The Spurr resin was prepared from (i) nonenyl succinic anhydride (NSA), (ii) vinylcyclohexene dioxide (VCD), (iii) diglycidyl ether of polypropylene glycol (DER) and (iv) dimethylaminoethanol (DMAE) mixed in that order in ratio of 10:6:26:0.4 respectively. The suspensions were systematically kept in a desiccator in order to keep exposure to

atmospheric moisture to a minimum. The impregnated samples were placed in capsules and the resin was cured overnight in a 70°C oven. The resulting blocks were trimmed with a glass knife and ultrathin sectioning (90 nm thick) was performed using a Riechert Ultracut E microtome equipped with a Jumdi HA1017 diamond knife. The ultrathin sections floated onto water were collected onto carbon-coated grids.

2. 2. 2. Vibrating sample magnetometry

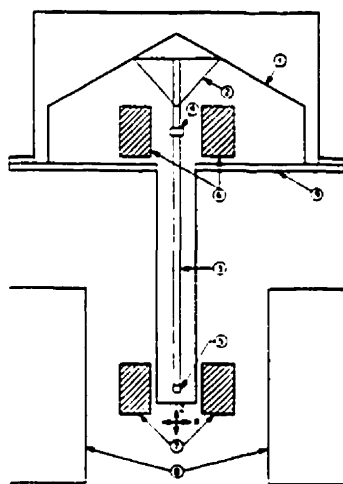


Figure 2. 9. first model of vibrating sample magnetometer. (1) loud speaker transducer, (2) conical paper cup support, (3) drinking straw, (4) reference sample, (5) sample, (6) reference coils, (7) sample coils, (8) magnet poles, (9) metal container (Foner, 1959).

If a material is placed within a uniform magnetic field, a magnetic moment, σ , will be induced. In a VSM, the sample is placed within the pick-up coils, and is made to undergo sinusoidal motion thus resulting in magnetic flux changes which induce a voltage in the pick-up

coils. This voltage E is proportional to the magnetic moment of the sample σ through

$E = \sigma GA 2\pi f \cos(2\pi ft)$, where G is dependant on the detection coil geometry, A is the amplitude and f the frequency of the sinusoidal vibration (Foner, 1996).

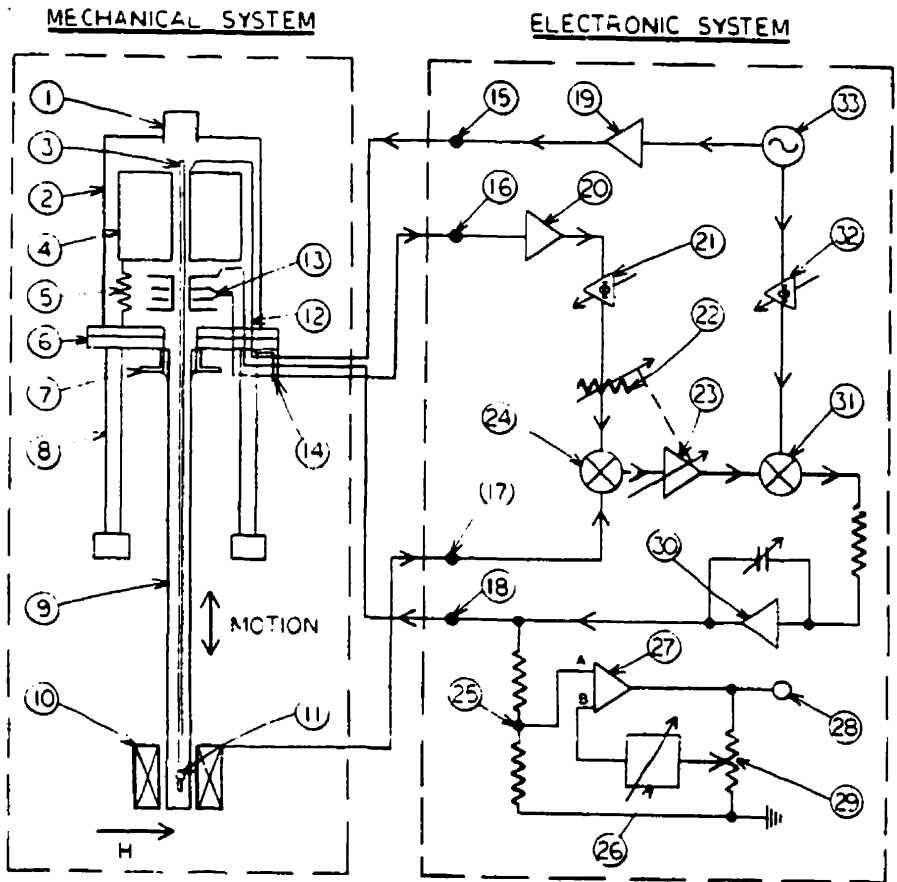


Figure 2. 10. functional diagram of the complete FM-1 system.

The VSM we used (model FM-1, manufactured by PAR under license in US patent No. 2,946,948) is based on the instrument first described by Foner (1959), schematized in figure 2.9.

The complete system (electronic and mechanical portions) is represented figure 2.10. The sample

(11) is suspended by a long vertical rod (3) vibrated vertically by the transducer (4). A vibrating capacitor (13) is made up of two fixed circular metal plates enclosed in two plates attached to rod 3 (figure 2.11).

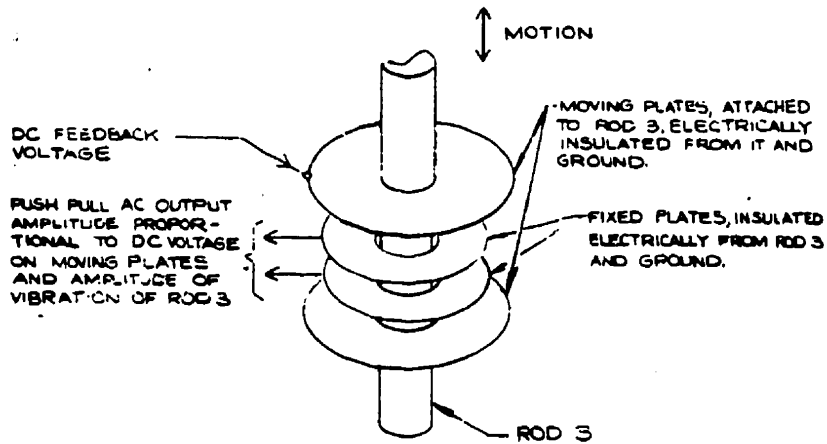


Figure 2. 11. vibrating capacitor assembly.

Both sample (11) and sample pick-up coils (10) are enclosed in an externally generated magnetic field, the sample moving and the coils stationary in that field. An AC signal at vibrating frequency and of amplitude proportional to the magnetic moment of the sample is in result generated in the sample coils and applied to the "sample signal output" (17), while an AC signal (reference signal) generated by the vibrating capacitor at vibrating frequency and of amplitude proportional to the vibration amplitude and the DC voltage applied to the moving plates, is applied to the "reference signal output" (16). The reference signal passes successively through a pre-amplifier (20), a phase shifter (21) and an attenuator (22) before being combined to the sample signal in an adder (24).

The output of the adder is fed via variable gain amplifier 23 to phase-sensitive detector 31 whose output is a DC voltage with amplitude proportional to the amplitude and with polarity

dependant on the phase of the adder output. This DC feedback voltage, fed through lowpass amplifier 30 to the capacitor plate assembly can automatically be adjusted to make the adder output very nearly zero. A fraction of the DC feedback voltage is applied through the divider 25 to input A of chopper-stabilized DC amplifier 27, while inverse feedback is provided at input B via divider 29 and variable DC source 26. When the output in 26 is the same as that of 25, the output of 27 (28) will be at ground. If the DC output of 31, *ie.* the magnetization moment of the sample should change slightly, a proportional change, determined by the setting of 29, will occur at 28 and can be recorded.

The external magnetic field used in the following chapters was within the range -1.5 T to 1.5 T. Throughout the measurement, the field steps were of ~ 50 mT for a range -1 T to 1 T and ~ 20 mT for a range - 0.1 T to 0.1 T. To establish the superparamagnetic character of our sample on the basis of their coercive field these steps are one to two orders of magnitude too high and a less accurate interpolation was used.

The instrument sensitivity given by the manufacturer is 5×10^{-8} J/T (5×10^{-5} emu). The precision actually achieved in our measurements (deduced from the noise level for weakly magnetic samples) was $\sim 10^{-6}$ J/T (5×10^{-2} J/T/kg for a mass of 20 mg). To calibrate the instrument, a nickel flat cylinder ($M_s = 55.4$ J/T/kg) was vibrated parallel to its axis direction.

2. 2. 3. Mössbauer spectroscopy

Since the majority of magnetic materials contain iron as their magnetic element, ^{57}Fe Mössbauer spectroscopy provides an ideal research tool, being a nondestructive and reliable technique that offers high resolution of charge state, ordering temperature, magnetic moment direction, and other parameters.

Mössbauer spectroscopy has become a standard technique to characterise superparamagnetic particles; it offers many advantages over other techniques for measuring their magnetic properties. It probes the solid state at the atomic dimensions so that one observes the statistical sum of the individual isotope environment rather than a bulk average. The data comes in the form of a spectrum rather than a magnitude, thus containing much more information in a form that can be determined in a very precise way. The very sharp energy resolution investigation of the small energy changes coming from hyperfine interactions between the nucleus and its surrounding electrons (Dormann, 1981). Finally, much smaller characteristic time ($\tau_m \sim 10$ ns) than other techniques such as VSM ($\tau_m \sim 1$ s) allow to detect magnetic ordering up to faster relaxation times.

However, Mössbauer spectroscopy cannot replace other techniques from which complementary data can be obtained. Examples are transmission Electron Microscopy (TEM - size, shape, concentration, crystallographic parameters of the particles), X-ray (size, crystallographic parameters), Vibrating Sample Magnetometer (VSM - magnetisation).

2. 2. 3. 1. Theory of Mössbauer spectroscopy

The Mössbauer effect

The Mössbauer effect is the recoil-free emission or absorption of a gamma ray (of energy E_γ) by a nucleus bound in a solid. For free nuclei, the recoil energy lost both during emission and absorption would prevent resonant absorption under normal circumstances and the effect is observable only if both emitting and absorbing nuclei are bound to a solid matrix. The γ -transition energy is then shared between the γ -photon and the lattice vibration phonons. Because of quantisation conditions, a fraction of events f occurs with no change in the lattice vibrations, and the entire transition energy is manifest in the γ -photon energy E_γ . The fraction of recoil-free event f will then depend on,

- the free atom recoil energy, proportional to E_γ^2 ,
- the temperature,
- the vibrational properties of the lattice.

Hence, Mössbauer effect is restricted to certain isotopes and optimized in general for low energy gamma rays associated with nuclei strongly bound in a crystal lattice at low temperatures. The importance of iron bearing material and an almost ideal combination of the ^{57}Fe isotope physical properties for Mössbauer spectroscopy, makes this isotope by far the most widely used.

Mössbauer spectrometer

Mössbauer experimental set-up involves a radioactive source - which contains a radioactive element producing the Mössbauer isotope in an excited state - and an absorber consisting of the material to be investigated - which contains the same isotope in its ground state. For ^{57}Fe isotope, the source is usually radioactive ^{57}Co giving by spontaneous electron capture transition, a metastable state ^{57}Fe which decays to the ground state emitting a gamma ray cascade including the 14.4 KeV gamma ray (figure 2.12).

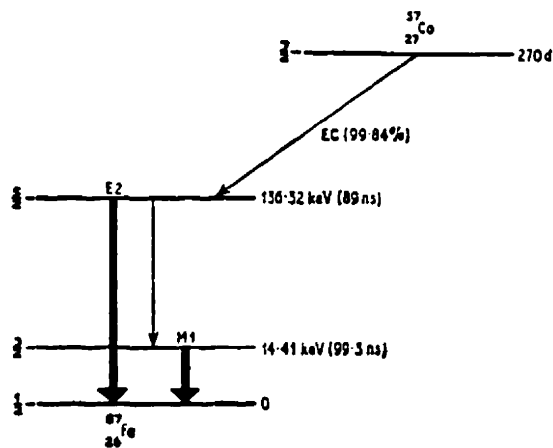


Figure 2. 12. nuclear decay of ^{57}Co showing the transition giving the 14.4 KeV Mössbauer gamma ray (Dickson and Berry, 1986).

Once emitted by the source, the gamma rays pass through the absorber where they may be partially absorbed if their energy matches exactly the nuclear energy level gap in the absorber, then passes to a suitable detector (figure 2.13). By the mean of a transducer, the source is moved

away from or toward the absorber with a velocity of the order of 1 mm/s, giving the gamma ray an energy shift as a result of the first order Doppler effect. In order to obtain an energy scan, the source can be driven to follow an oscillatory motion, usually made at constant acceleration, giving the velocity oscillation a triangular shape.

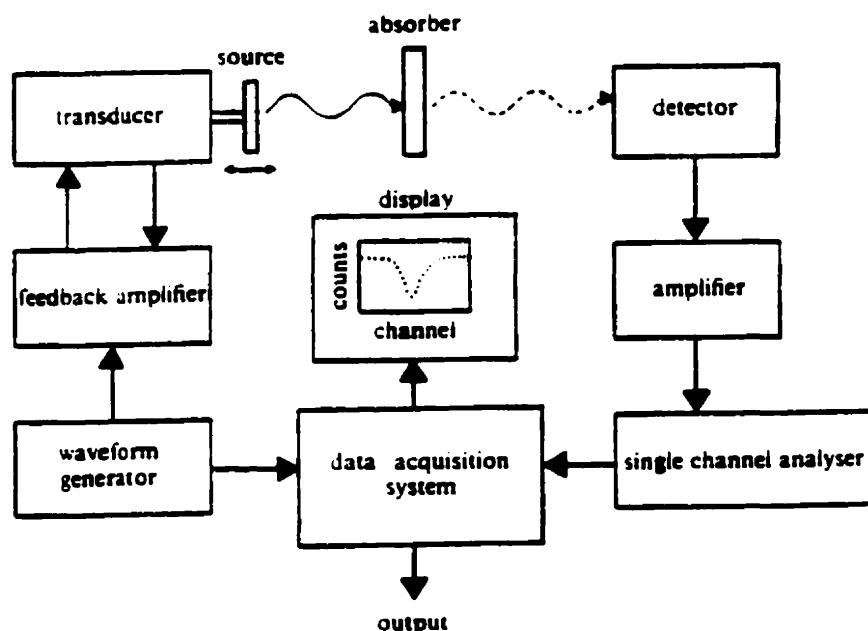


Figure 2. 13. A block diagram of a typical Mössbauer spectrometer (Dickson and Berry,

1986).

Interpretation of the Mössbauer data

A Mössbauer spectrum is characterised by the number, shape, position and relative intensity of the various absorption lines it contains. These features are related to the nature of the hyperfine interactions experienced between the nuclei and the surrounding electrons and their time dependence.

The Hamiltonian for the atom can be written (Greenwood and Gibb, 1971):

$$\mathcal{H} = \mathcal{H}_0 + E_0 + M_1 + E_2 + \dots$$

The first term, E_0 , is the electric monopole (or coulombic) interaction between nucleus and electron. It can be expressed as

$$E_0 = -Ze^2 / \kappa \int \rho_e d\tau / r,$$

with Ze , the charge of the nucleus; κ , the dielectric constant of vacuum; ρ_e , the electronic charge density in the volume element $d\tau$; and r , the radial distance from the nucleus.

The second term, M_1 , is the magnetic dipole hyperfine interaction,

$$M_1 = -\boldsymbol{\mu} \cdot \mathbf{H} = -g \mu_m \mathbf{I} \cdot \mathbf{H},$$

with $\boldsymbol{\mu}$, the nuclear magnetic moment; \mathbf{H} , the magnetic field at the nucleus; \mathbf{I} , the nuclear spin; g , the Landé factor; and μ_m the nuclear magneton.

The third and last term, E_2 , is the electric quadrupole interaction,

$$E_2 = eQ / 2I(2I - 1) \sum_i (\partial^2 V / \partial x_i^2) I_i^2,$$

with Q , the nuclear quadrupole moment; I , the nuclear spin; V the electric potential; I_i , the spin

operators.

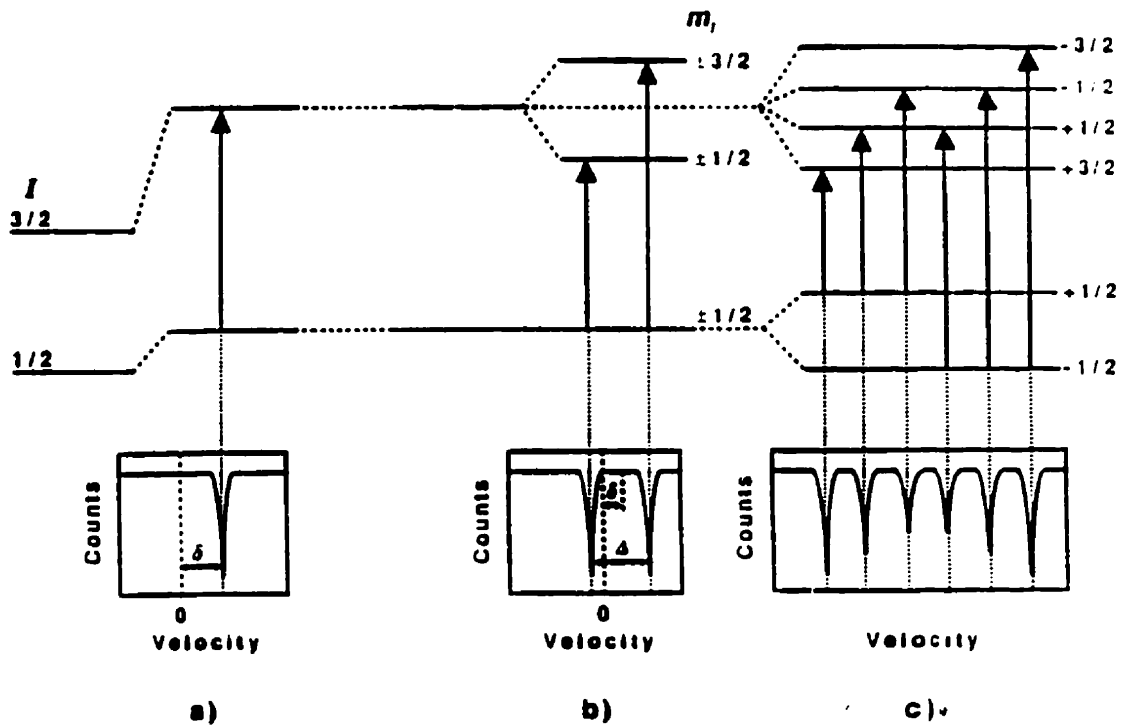


Figure 2. 14. The effects on the nuclear energy levels of ^{57}Fe of (a) the isomer shift, (b) the quadrupole splitting and (c) the magnetic splitting (Dickson and Berry, 1986).

(i) *The isomer shift.* The first interaction, E_0 , results in a shift in the position δ , of the observed resonance lines known as the isomer or chemical shift (figure 2.14). It can be expressed

as

$$\delta = 2\pi/3 Ze^2 [\langle r_e^{-2} \rangle - \langle r_g^{-2} \rangle] \times [|\psi_s(0)|^2 - |\psi_g(0)|^2],$$

where $[\langle r_e^{-2} \rangle - \langle r_g^{-2} \rangle]$ accounts for the difference in the nuclear radius between the nucleus in the

excited and the ground states, and $[|\psi_s(0)|^2 - |\psi_g(0)|^2]$ for the differences between the absorber and source electronic densities (for instance in case the nuclei belongs to different materials). δ is thus function of both nuclear and electronic properties of the system. In practice, the nuclear parameters are constant and in situations where they have already been determined, it is possible to derive quantitative information on the electronic environment of the nucleus from measurement such as the atomic oxidation states or covalency effects and shielding of one set of electron by another.

(ii) *Quadrupole splitting.* A nucleus with a spin quantum number of greater than $I = 1/2$ has a non-spherical charge distribution which if expanded as a series of multipoles contains a quadrupole term. The quadrupole moment Q describing the magnitude of the nucleus charge deformation can interact with an asymmetrical electric field produced by an asymmetrical electron charge distribution which is characterized by an electric field gradient tensor $E_{ij} = -V_{ij} = -(\partial^2 V / \partial x_i \partial x_j)$. The result of this interaction, is a quadrupole splitting of the nuclear energy levels (figure 2.14).

In the case of ^{57}Fe , a single line spectrum results in a two-line spectrum (doublet) with the two lines separated by

$$\Delta = e^2 q Q / 2 \sqrt{1 + \eta^2/3},$$

with $q = V_{zz}/e$; $\eta = (V_{xx} - V_{yy})/V_{zz}$.

Again, a nuclear quantity, the quadrupole moment, and an electronic quantity, the electric field gradient are involved. The quadratic moment being defined for a given nucleus, information

on the electric field gradient affected by the symmetry of the bounding environment and the local structure in the vicinity of the atom can be extracted from the Mössbauer spectra. Access to information relative to the electronic properties of various orbitals, isomerisation phenomena, ligand structure is possible.

(iii) Magnetic splitting. The term M_I in the Hamiltonian, is the nuclear Zeeman effect that results when the nuclear magnetic moment interacts with a magnetic field. This magnetic field can originate either within the atom itself, within the crystal via exchange interactions or as a result of an externally applied magnetic field. The corresponding energy levels are,

$$E_m = -\mu H m_I / I = -g \mu_m H m_I,$$

I being the nuclear spin; m_I , the magnetic quantum number, component of I along the field direction (figure 2.14). For ^{57}Fe , the ground state ($I = 1/2$) and the excited state ($I=3/2$) split into respectively two and four substates, giving rise according to the selection rules to six possible transitions.

The splitting of the spectral lines is directly proportional to the magnetic field experienced by the nucleus which can thus be easily measured. When no external field is applied, the only contribution to that field comes from the magnetic hyperfine field that can be related to the orbital state of the atom. In paramagnetic compounds, the electron spin relaxation is usually rapid (corresponding to time scales $\ll 10$ ns) and results in hyperfine fields having a time average of zero so that no magnetic splitting is seen. When cooperative phenomena such as ferromagnetism

or antiferromagnetism operate, the relaxation rates are effectively slower and a splitting will be recorded.

The magnetic splitting can provide information on the magnetic ordering and structure of magnetically ordered systems, the nature of the magnetic interactions, the size of the magnetic moments on particular atoms and details of the electronic structure of the atom which relate to the hyperfine structure of the Mössbauer atom. Applying an external magnetic field can change significantly the spectrum and be of considerable assistance in its interpretation.

(iv) Time dependent effects. As already mentioned, the vibrational properties of the system affect the recoil-free fraction of the Mössbauer effect, with changes on the line intensity of the spectrum. One must consider also time-dependant changes in the nuclear environment, referred to as relaxation processes, relative to the characteristic times of both the Mössbauer process and the hyperfine interaction. These relaxation processes arise from structural changes in systems, as well as electronic configuration changes such as valence fluctuation (electron hopping), or fluctuation in the orientation of electronic spins (paramagnetism). These time dependence effects affect both the spectral line-shape and the value of the hyperfine Mössbauer parameters.

2. 2. 3. 2. Application of Mössbauer spectroscopy to superparamagnetic systems

The characteristic period to be considered in a Mössbauer measurement can be estimated as (Dormann, 1981):

$$\tau_m \sim \hbar / |g\mu_m H_{\text{hyp}}| \sim 10^{-8} \text{ s.}$$

Magnetic nanoparticles are associated with a relaxation time τ , and the three following cases corresponding to three different spectra are to be considered.

First when $\tau \gg \tau_m$, the spectra will be very similar to the one of the bulk material featuring well defined magnetic multiplet (six peaks in the ^{57}Fe case). However, since the system is now made of interacting particles of different sizes (therefore of different relaxation times), the spectra will feature asymmetrical and broadened line shapes. The small fluctuation of the magnetization around an energy minimum (collective magnetic excitation) may also result in a decrease in the measured hyperfine field:

$$H_{\text{hf}}(V, T) = H_{\text{hf}}(V=\infty, T) \langle \cos \theta \rangle_T,$$

where $H_{\text{hf}}(V=\infty, T)$ is the hyperfine field in a large crystal at the temperature T and $\langle \cos \theta \rangle_T$ is the thermal average of the angle θ between the magnetization direction and the easy direction of magnetization. In the low temperature limit ($KV/kT \gg 1$) it is found that:

$$\langle \cos \theta \rangle_T \sim 1 - kT/2KV.$$

When $\tau \ll \tau_m$, the nuclear hyperfine magnetic field H_{hf} will average to zero and the spectrum will not feature any magnetic splitting. The remaining features will then only be attributable to an eventual quadrupole splitting or an isomer shift.

In the intermediate range, $\tau \sim \tau_m$, complex spectra with broaden lines can be observed. In practice, τ is very sensitive to temperature ($\tau = \tau_0 \exp(KV/ k_B T)$); in many cases only a small fraction of the particles have relaxation times in the critical region ($\tau_m \sim 10$ ns) and the spectra can therefore be considered as consisting of a magnetically split component ($\tau \gg \tau_m$) and a paramagnetic component ($\tau \ll \tau_m$). By comparing the areas of the two components, one can estimate the proportion of particles having relaxation times higher or lower than τ_m . Then using the Arrhenius expression

$$\tau = \tau_0 \exp(KV/ k_B T),$$

a critical volume $V_c = (k_B T/K) \ln (\tau/\tau_0)$ can be determined for several temperatures, leading to an estimate of the volume distribution. The volume determined for equal areas is named the *median volume* and the corresponding temperature, the *mean blocking temperature* $\langle T_B \rangle$.

2. 3. References

Chanzy, H. (1997) personal communication.

de Jong, M. (1987) course on TEM held at the Application Laboratory of Philips Electron Optics in Eindhoven.

Dickson, D.P.E., Berry, F.J. (1986) *Mössbauer Spectroscopy*. London: Cambridge University Press, p. 1.

Dormann, J. L. (1981) *Revue Phys. Appl.*, 16, 275.

Foner, S. (1959) *Rev. Sci. Instrum.*, 30, 548.

Foner, S. (1996) *J. Appl. Phys.*, 79, 4740.

Greenwood, N.N., Gibb, T.C. (1971) *Mössbauer Spectroscopy*. London: Chapman and Hall Ltd, p. 46.

Johnson, D.L. patent: U.S. 3,447,959 (1969) to Eastman Kodak Co..

Mc Corsley patent: U.S. 4,246,221 to Akzona Inc..

Marchessault, R.H., Dubé, M., St. Pierre, J. And Revol, J.F. (1977) Fibre-Water Interactions in Paper-Making, Transactions of the Symposium held at Oxford: Sept. 1977.

Nissan, A.H. (1976) *Macromolecules*, 9, 840.

Otten, M.T. (1993) *Alignment of the Transmission Electron Microscope*, first ed.. Eindhoven: Philips Electron Optics, p. 1.

Watanabe, K., and Yamanaka, S. (1994) *Proceedings of the International Symposium on Fibre Science and Technology*, Yokohama, Japan, p. 445.

Wooding, C.R. (1993) in *Encyclopaedia of Chemical Technology*, fourth edition (Kirk-Othmer

ed.). New York: John Wiley and Sons, vol. 10, p. 717.

Yamanaka, S., Watanabe, K., Kitamura, N., Iguchi, M., Mitsuhachi, S., Nishi, Y. And Uryu, M.

(1989) *J. Mat. Sci.*, **24**, 3141.

CHAPTER III - MAGNETIC MEMBRANES BASED ON BACTERIAL AND MAN-MADE CELLULOSE

3. 1. Introduction

The technique of precipitation of inorganic salts in cellulose fibres to define the microvoids and texture of fibrous cellulose was reviewed by Hock and Mark (1946). Frey-Wyssling (1959) and others (Frey-Wyssling and Mühlethaler, 1965; Belford and Preston, 1957; Belford *et al.*, 1958) made extensive use of the technique in the pre-electron microscope era for ultrastructural studies complementary to x-ray diffraction line-broadening. The method remained unused once transmission electron microscopy became the method of choice for observing the microfibrils and textural organization of cellulosic, chitins, algae, etc. However, the methodology for creating these composites is being revisited as the drive to explore nanocomposite materials expands (Calvert, 1994; St. Pierre *et al.*, 1994).

An approach to the synthesis of ferrites in the cell wall of cellulose fibres started with carboxymethylated pulp which yielded nanocomposite superswollen fibres (Marchessault *et al.*, 1992). These fibres dried to parchment-like membranes with 100 Å size ferrites embedded in the cellulosic matrix. A practical application of this subject is synthesis of superparamagnetic fibres and membranes which only respond magnetically in the presence of a field, do not display remanence and show less colouration than materials based on conventional ferrites (Ziolo *et al.*, 1992). While the carboxymethylated cellulose pulp provided a highly swollen ionic matrix, ongoing studies suggested that neutral cellulose gels would be just as effective a substrate, that is

ion exchange is not necessary for introducing ferrous ions into a cellulose matrix. The dynamics of ferrite synthesis suggest that the role of the ionic matrix is to encourage a diffusion process for the ferrous ions and the initial ion exchange (Ziolo, 1984) is part of this interaction. The subsequent chemistry to generate magnetic iron oxides takes place in the microvoids of the swollen matrix, as in a collection of parallel-linked microreactors with a high surface to volume ratio (Raymond *et al.*, 1994; *ibid*, 1995).

In a previous paper three neutral cellulose gels which were exposed to the ferrite synthesis methodology were described. The treated gels were subsequently examined by transmission electron microscopy combined with magnetic properties evaluation (Raymond *et al.*, 1994; *ibid*, 1995). The three cellulose samples were: alkali swollen tirecord rayon, never dried wet-spun model fibres of cellulose, and never dried but purified membranes of bacterial cellulose. These samples provided controlled levels of swelling and known morphologies for testing the hypothesis that nanocomposite ferrite synthesis in cellulose depends only on the size, shape and distribution of the water domains inside the swollen matrix. As long as diffusional penetration of Fe^{2+} into the swollen matrix is satisfactory, neutral cellulose gels are effective materials for *in situ* synthesis of ferrites. Of the three samples of neutral gels, the model wet-spun fibres and the bacterial cellulose provided products where nanosize ferrites were uniformly spread throughout the swollen substrate. X-ray analysis provided evidence for the presence of at least two different ferrites: maghemite ($\gamma\text{-Fe}_2\text{O}_3$) and magnetite (Fe_3O_4). These ferrites have very similar ferrimagnetic spinel structures, mainly differing in the occupation of the octahedral sites which is only complete for stoichiometric magnetite. These very similar structures make a clean distinction difficult, as the actual stoichiometry can range between the two theoretical limits (Vanderberghe *et al.*, 1990).

Of particular interest was the bacterial cellulose (Raymond *et al.*, 1994; *ibid*, 1995), a highly swollen microfibrillar gel (100:1 water/cellulose ratio) which after *in situ* synthesis of ferrites dries to a magnetic thin film nanocomposite. In the present study, this gel is further characterized in parallel with another gel membrane: Lyocell, a man-made cast film similar to the above mentioned wet-spun fibre, though being coagulated as a membrane rather than a fibre.

3. 2. Experimental section

3. 2. 1. Materials

Bacterial cellulose (BC) membranes from *Acetobacter xylinum*, produced at the surface of the culture medium, were kindly provided by K. Watanabe of Biopolymer Research Co. Ltd, Kanasaki 213, Japan. After washing in distilled water (DW) they were boiled in 4% (w/w) aqueous NaOH to destroy protein followed by another wash to neutrality. These purified gel bacterial celluloses (about 2 mm thick and containing 99% of water by weight) were stored in 50% ethanol. When used, they were solvent exchanged to 100% DW.

Lyocell membranes were cast from solutions of 7.5% dissolving cellulose pulp in N-methylmorpholine-N-oxide (MMO), coagulated in 60°C water, as a uniform thickness membrane (Chanzy *et al.*, 1979). The materials thus obtained were thoroughly washed and used in the water-swollen state to prepare nanocomposites. They were 1 mm thick and contained about 80% water by weight.

The two different gels under consideration, are both made of cellulose. Bacterial cellulose is a native cellulose, having a high degree of crystallinity (~70%) when dried, but forming a very swollen nascent gel. Lyocell is a coagulated solution of cellulose forming a tough membrane when dried, with a degree of crystallinity of 40 to 45%. These parameters are expected to affect the phase, shape, size distribution and concentration of the ferrites yielded by *in situ* synthesis.

3. 2. 2. *In situ* synthesis

Membranes of bacterial cellulose (BCR) and fibres of model filaments were described previously (Raymond *et al.*, 1995). In the present work, other bacterial cellulose membranes (BCS) as well as Lyocell membranes were *in situ* processed to create ferrite nanocomposites, using the following protocol: approximately ten grams of never-dried purified bacterial cellulose (or Lyocell) membranes are dipped in a solution of $\text{FeCl}_2 \cdot 4\text{H}_2\text{O}$ (1 g/100 ml of DW). After a period of one hour, the sample is rinsed and dipped in a fresh solution of NaOH (50 ml at 0.02 M), causing development of a dark-green colour; the suspension is then heated to 65 °C in a water-bath and hydrogen peroxide (10 ml at 1 %) is added dropwise over a period of 15 minutes. The container is then removed from the heat source and the sample is stirred for one hour, followed by DW washing. Up to five cycles of this treatment were performed. In this treatment, the membranes were successively dipped into the different reagents rather than immersed in a single container where a bulk reaction would occur along with the *in situ* synthesis. By this means the focus of the reactions was exclusively inside the membrane.

The chemistry implied in the successive reactions is complex and various factors can affect the process. In particular, Fe^{2+} ions are easily oxidised to Fe^{3+} ions, their respective concentrations determine the yield of the synthesis. In order to have a better control of these parameters, only fresh reagents should be used. Nitrogen was bubbled through the iron chloride solution, to lower the concentration of O_2 . The addition of iron metal, ideally as fine “wool”, has been used to promote the reduction of Fe^{3+} ions ($\text{Fe} + 2\text{Fe}^{3+} \rightarrow 3\text{Fe}^{2+}$) (Ziolo, 1984).

Drying of the processed sample is a crucial step if one desires a tough uniform membrane.

Most of the samples used in this work were dried either on Teflon or on glass (Teflon avoids adhesion whereas glass prevents membrane curling).

3. 2. 3. Transmission Electron Microscopy (TEM)

After solvent exchange to ethanol and then to propylene oxide, the membranes were embedded in Spur resin either as a neverdried gel (Lyocell and BCR) or as a dry parchment (BCS), and ultrathin sectioning was performed with a Reichert Ultracut E microtome equipped with a diamond knife.

Dried Lyocell membranes were ground in DW using a mortar and pestle, then was placed on a TEM grid and allowed to dry.

A Philips CM 200 transmission electron microscope (TEM) operated at 160 kV, or 200 kV was used for imaging by diffraction contrast in the bright field mode and for selected area (SA) diffraction.

3. 2. 4. Magnetic characterisation

The magnetic properties of the *in situ*, treated materials after air drying were examined by vibrating sample magnetometry (VMS) and Mössbauer spectroscopy (MS). For the VMS measurements, approximately 20 mg of sample was vibrated in a magnetic field of up to 1.5 T and the response of the material was plotted as a function of the applied field to yield a magnetization curve. A conventional constant acceleration Mössbauer spectrometer in transmission geometry

using a 1G**q**57Co**Rh** source was used.

3. 3. Results and discussion

With the naked eye, it was possible to distinguish a darker skin at the surface of the processed Lyocell membranes suggesting that ferrites were predominantly forming at the surface. In the case of bacterial cellulose, the membranes showed a more homogeneous colour. Lyocell membranes are probably more resistant to penetration than bacterial cellulose due to the combination of lower swelling and the formation of a skin during the coagulation process.

3. 3. 1. Transmission Electron Microscopy

Micrographs of Lyocell membranes (figure 3.1) are dominated by particles of two different shapes, acicular and equiaxial. Except for some fine grains (~ 1 nm), acicular particles (20 - 100 nm long, with an aspect ratio ~ 4 - 10) were the only particles to be seen after single cycle treatment. From the second cycle on, equiaxial particles are prevalent. Both their size and concentration then increase from the second (5 - 10 nm for the smaller, 15 - 20 nm for the larger) to the third cycle (~ 13 nm for the smaller, 20 - 40 nm for the larger). Electron diffractograms for equiaxial particles from the second and third cycles suggest the presence of magnetite and ferrihydrite ($5\text{Fe}_2\text{O}_3 \cdot 9\text{H}_2\text{O}$). Single crystal diffraction patterns for large elongated particles (~ 500 nm long, ~ 50 nm wide) correspond to diffraction data for $\delta\text{-FeOOH}$ (feroxyhite).

Figure 3. 1a. Electron micrograph of Lyocell membrane after one cycle of the *in situ* process. The bar corresponds to 200 nm.



Figure 3. 1b. Electron micrograph of Lyocell membrane after three cycles of the *in situ* process. The equiaxial particles not observed after one cycle, are present here. The bar corresponds to 500 nm.



31 BK 1
1890

The above observations seem to indicate the occurrence in Lyocell membranes, on the first cycle (figure 3.1a) of feroxyhite in the form of needles, while at this stage, magnetite only appears as seed particles (~ 1 nm) in weak concentration. Feroxyhite was indeed reported as the product of topotactic transformation of ferrous hydroxide precipitates by fast oxidation in strongly alkaline medium (*cf.* section 1.2.2; Bernal *et al.*, 1959). From the second cycle on (figure 3.1b), round particles identified by TEM diffraction as magnetite, appear to the detriment of the needles, suggesting that freshly supplied ferrous ions combine with ferric ions provided by the hydrated ferric oxide phase to form a new phase of mixed valence, magnetite.

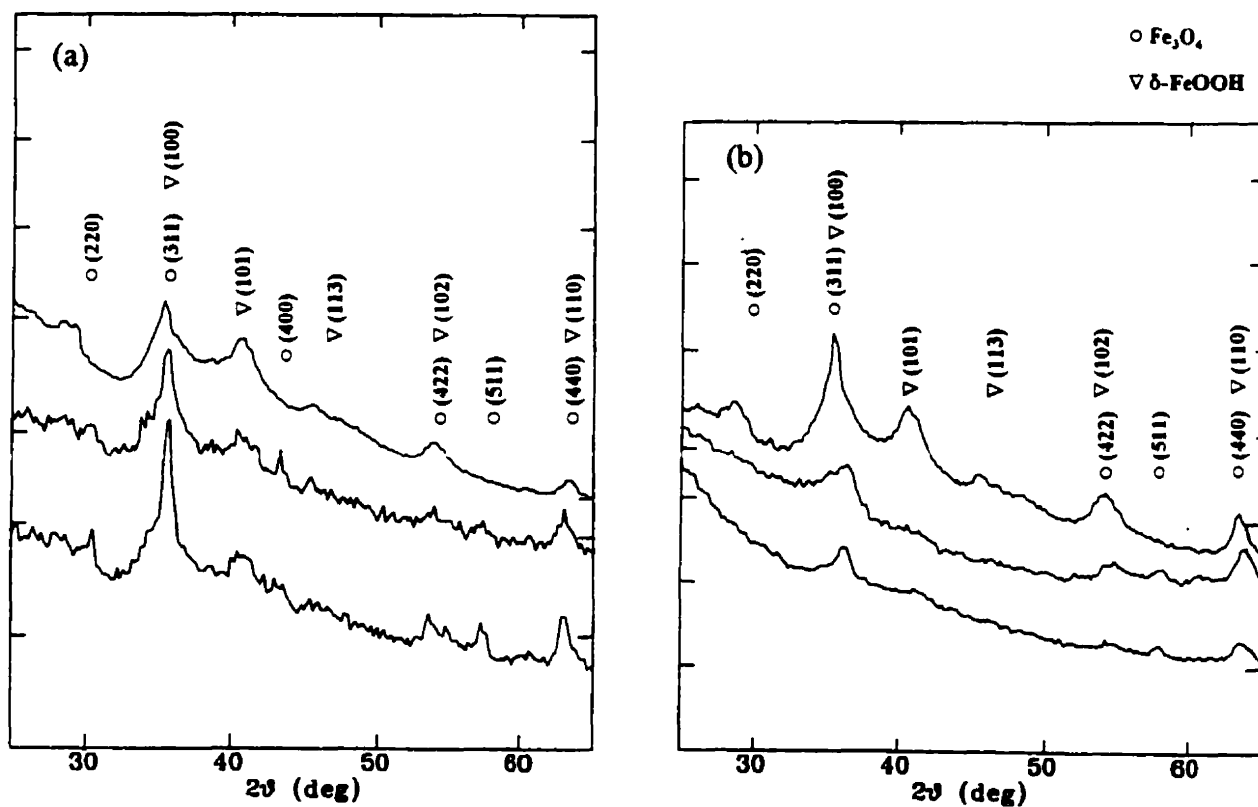
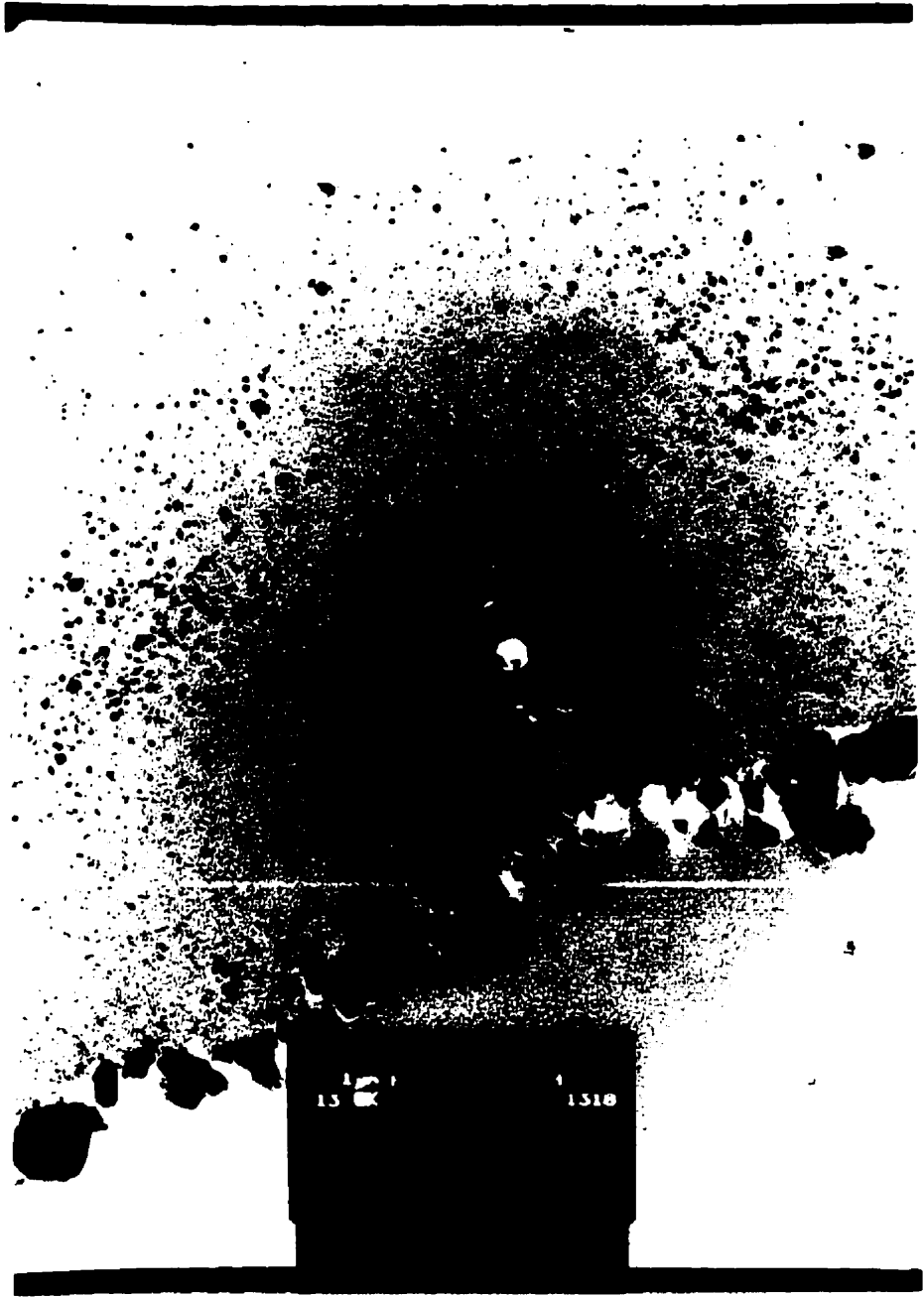


Figure 3. 2. XRD pattern of Lyocell (7.5%) membranes *in situ* treated over one cycle (upper most), two cycles and three cycles (lower most). (a) ground membrane; (b) membrane “as prepared”.

X-ray diffraction (XRD) patterns - using Cu-K α radiation ($\lambda = 1.5418 \text{ \AA}$) - were measured for the Lyocell membranes (figure 3.2) either “as prepared” (as X-rays are absorbed by the cellulose, the pattern is surface dominated) or ground. No significant difference was observed between the two patterns after one cycle attesting the concentration of feroxyhite at the surface. A difference appears after two, and is very clear after three cycles, as a result of the ferrites penetration within the membrane, where magnetite replaces feroxyhite.

The above discussion applies to treatments using *fast oxidation* with peroxide: feroxyhite in that case is produced first, magnetite appearing only after several cycles. Figure 3.3 shows a micrograph of a Lyocell membrane treated this time with *slow oxidation* by contact with atmospheric air. Magnetite appeared here directly after one cycle in the form of large particles (200 to 400 nm) coating the surface, while forming only few fine particles (10 - 15 nm) inside the membrane, with shallow penetration. An indirect formation of magnetite over several cycles therefore improves the loading homogeneity. The absence of fine particles (10 - 15 nm) in the immediate vicinity of the surface (figure 3.3) testifies on the other hand that a surface skin has formed during the film coating process. The accidental presence in this skin of a large hole filled up by a large ferrite aggregate, indicates that the surrounding fine particles (beyond the skin) are accurate replicas of the void spaces provided by the membrane.

Figure 3. 3. Transmission electron micrograph of ultrathin section of a neverdried Lyocell membrane. The ferrites were oxidized by contact with atmospheric air (slow oxidation).



1510

1510

Micrographs of embedded wet bacterial cellulose BCR sections (figure 3.4) show both equiaxial and needlelike particles agglomerated and aligned. The equiaxial particles range in size from about 10 to 15 nm after three cycles and about 20 nm after five, being then more concentrated. The needles are 50 to 200 nm long with an aspect ratio of 10 - 20. Electron diffraction patterns were compatible with reference data for maghemite and lepidocrocite (γ -FeOOH).

The system made of needles encapsulated by round particles seems to replicate the fibrillar structure of the membrane, suggesting therefore that the cellulose fibrils would act as the nucleation site for growing needles which in turn provide a nucleation site for growing round particles. This is in keeping with the idea that a polar substrate is important but not necessarily an ionic one. The polar inner space acts to provide optimal penetration, and subsequent ferrite growth in confined space creates the nanosize ferrites.

In BCR membranes, the needles were identified as lepidocrocite (γ -FeOOH) whereas ferroxihite (δ -FeOOH) was found both in Lyocell (*cf.* above) and in BCS (*cf.* below) membranes. The treatment used to synthesise the BCR membranes (Raymond *et al.*, 1995) was in fact different than the one used here for Lyocell and BCS membranes, in that the ferrous ions present in solution outside the membrane were not removed before addition of NaOH. This might have decreased the pH increasing in turn the free Fe^{2+} concentration inside the membrane. Part of these free Fe^{2+} may be oxidized to Fe^{3+} , both combining to form a ferroso-ferric phase (green rust) which on subsequent oxidation would yield either lepidocrocite (fast oxidation), or magnetite (oxidation slow enough for dehydration to take place) (*cf.* section 1.2.2; Bernal *et al.*, 1959; Taylor and Schwertmann, 1974). Free ferrous ions, freshly supplied on the following cycles would

then be adsorbed on lepidocrocite, forming an intermediate complex, itself transformed to magnetite. This mechanism has been referred as a dissolution-precipitation process (*cf.* section 1.2.2; Tamaura *et al.*, 1983) or dissolution-recrystallisation and would explain the presence of magnetite particles at the surface of lepidocrocite needles.

Sections of dried BCS membranes (Figure 3.5) show the presence of round particles of two characteristic sizes, the smaller (~ 20 nm) being concentrated in the membrane thickness, the larger (~ 50 nm) close to the surface. Elongated particles are also observable, coating the membrane surface and tangled in an open cellulosic fibrillar structure.

Diffraction patterns for these samples featured concentric rings, with d-spacing characteristic of magnetite. Diffraction patterns for the elongated particles gave parameters that could be accurately associated with ferroxihite (δ -FeOOH), the occurrence of which has been reported for similar chemical conditions, *i.e.* rapid oxidation of alkaline ferrous hydroxide suspensions by hydrogen peroxide (Powers, 1975).

The preferential location of the ferroxihite needles at the membrane surface, while round magnetite particles (produced by slow oxidation, at lower pH) are in majority inside the membrane may result from restricted access inside the membrane to oxidizing agents and OH⁻ ions.

Figure 3. 4. Electron micrograph of a never-dried BCR membrane section after three cycles of the *in situ* process. Acicular particles are surrounded by equiaxial particles in a very open texture. The bar corresponds to 200 nm.



Figure 3. 5a. Electron micrograph of a dried BCS membrane section after one cycles of the *in situ* process. Rodlike particles are visible on the surface. The bar corresponds to 1 μm .



Figure 3. 5b. Electron micrograph of a dried BCS membrane section after three cycles of the *in situ* process. Equiaxial particles are larger on the surface than inside the membrane. The bar corresponds to 1 μm .



3.3.2. Vibrating Sample Magnetometry

Vibrating sample magnetometry (VSM) has a measurement timescale of about one second. On that time scale, all samples were found to be superparamagnetic at room temperature, i.e. neither remanence nor coercivity were observed.

Measured magnetisation curves (Figure 3.6) were fitted by superposing three to four Langevin functions, corresponding to a distribution of particle magnetic moments:

$$M = M_s \sum_i \alpha_i L(\mu_i B/kT), \quad (1)$$

where M_s corresponds to the global saturation magnetisation, α_i is the proportion of particle i of magnetic moment μ_i , ranging from 10^{-16} to 10^{-21} J/T; L is the Langevin function:

$$L(x) = \coth x - 1/x. \quad (2)$$

The result of the fit is shown in figure 3.7.

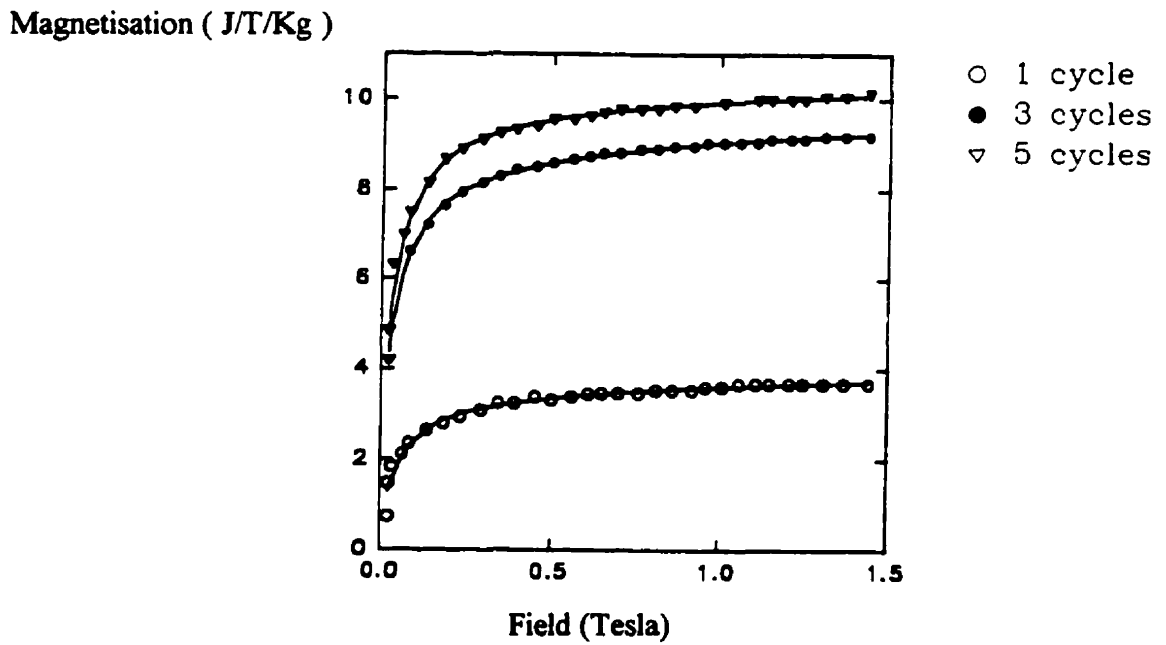
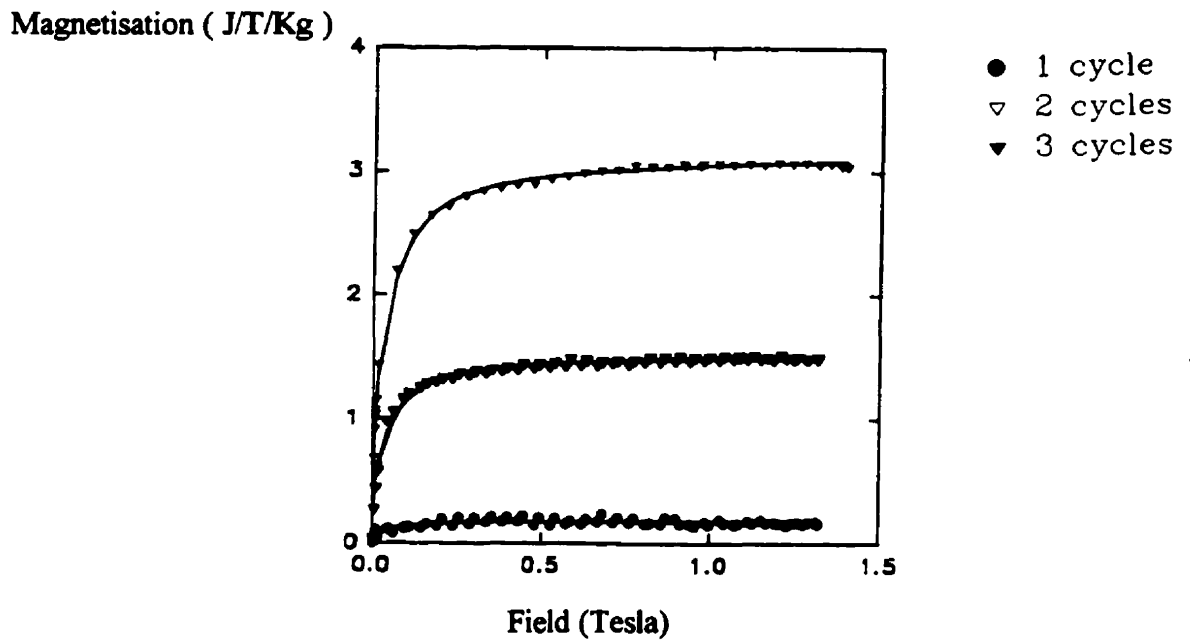


Figure 3. 6. Magnetisation curves measured by VSM for Lyocell (above) and BCR (below) membranes. The fit using equation (1) is represented as a solid line.

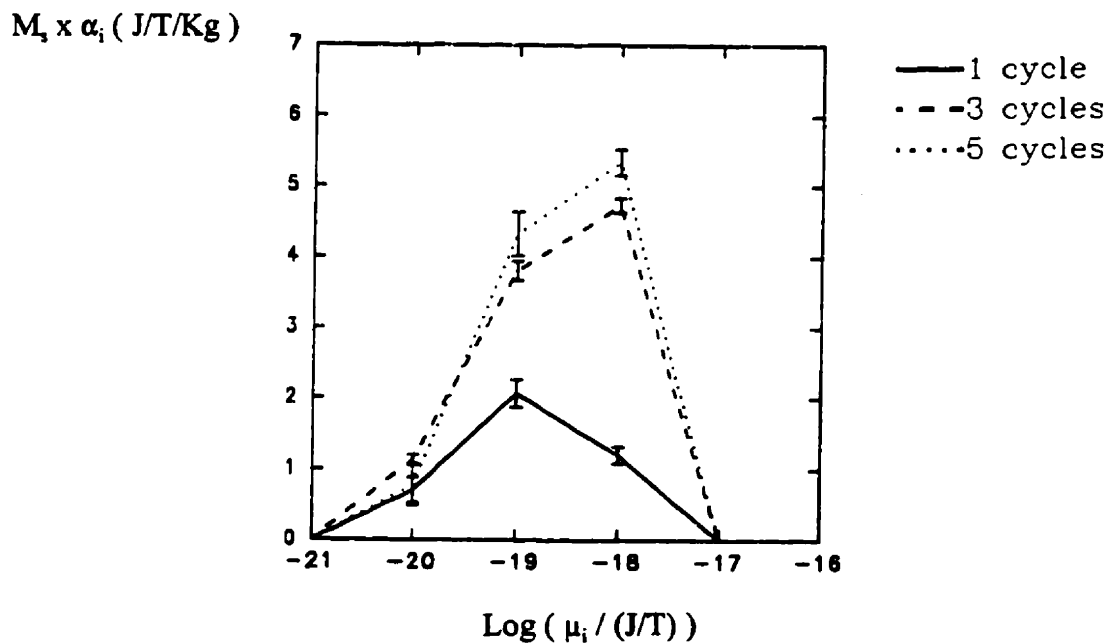
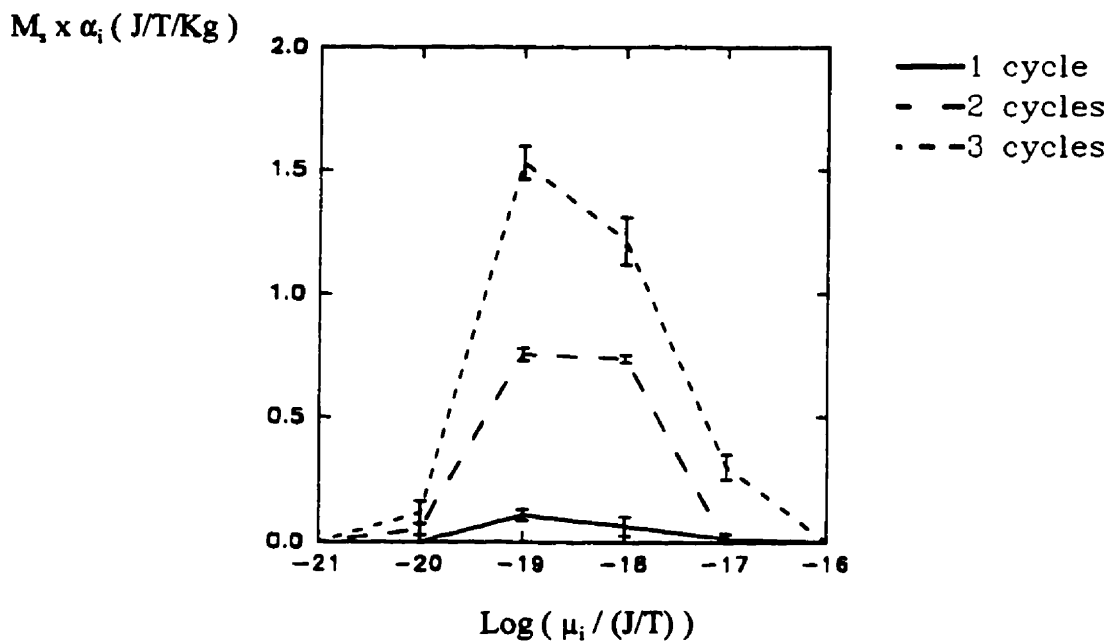


Figure 3. 7. Magnetisation moment distribution deduced from the fit of the magnetisation curves. Top is Lyocell, bottom is bacterial cellulose membrane.

From the magnetic moment distribution figure 7, the volume of the particles V_i can be deduced using

$$\mu_i = m_s V_i, \quad (3)$$

provided that their saturation magnetisation m_s is known. TEM showed the presence of spherical magnetite particles ($m_s \sim 5 \times 10^5 \text{ J/T/m}^3$) and rodlike ferroxihite particles ($m_s \sim 10^5 \text{ J/T/m}^3$). The distribution deduced from the fit (figure 3.7) is relatively broad, resulting from density fluctuations inside the membranes. Lyocell membranes have the broadest distribution, whereas the distribution peak would correspond to spherical magnetite particles $\sim 7 - 15 \text{ nm}$ in diameter or cylindrical ferroxihite particles $\sim 30 - 60 \text{ nm}$ long (aspect ratio of four), comparable to the dimensions found by TEM (*cf.* Section 3.3.1). For BCR membranes, the distribution peak would correspond to magnetite spheres $\sim 7 \text{ nm}$ in diameter or ferroxihite cylinders $\sim 50 \text{ nm}$ long (aspect ratio of ten) after one cycle, and respectively $\sim 15 \text{ nm}$ (magnetite spheres) or $\sim 120 \text{ nm}$ (ferroxihite cylinders) after three to five cycles, again in good agreement with the TEM results.

An estimate of the iron present in the samples was deduced from the fit (table 3.1), based on the assumption that bulk magnetite was the only magnetic component, *i.e.* the global saturation magnetisation M_s would be $122 \text{ J/T/kg}_{\text{Fe}}$ (88 J/T/kg). The iron content derived by this means is considerably less than that measured by atomic absorption.

Sample	weight % Fe	
	VSM	at. abs.
Lyocell		
1 cycle	0.15%	2.07%
2 cycles	1.29%	4.08%
3 cycles	2.58%	6.09%
BCR	VSM	at. abs.
1 cycle	3.35%	18.69%
3 cycles	8.08%	28.83%
5 cycles	8.80%	37.38%
BCS	VSM	at. abs.
1 cycle	0.76%	9.79%
2 cycles	1.24%	20.25%
3 cycles	1.66%	20.91%
4 cycles	4.91%	22.28%

Table 3. 1. Percentage of the sample weight attributable to iron. The first column was deduced from the fit of the magnetisation curves, assuming that the iron was entirely present as magnetite. The iron composition on the last column was determined by digesting a weighed sample in an acid mixture and analysing using atomic absorption.

The discrepancy between the two sets of Table 3.1 data can be explained as follows. First, the above mentioned global saturation magnetisation M_s corresponds to bulk magnetite with no consideration of the finite size or thermal effects usually responsible for a spin canting inside magnetic nanoparticles. The actual saturation magnetisation is hence expected to have lower values (Martinez *et al.* (1996) found a decrease in the saturation magnetisation of maghemite

particles at 4.2K from 88 emu/g to 23 emu/g and 64 emu/g for particle sizes of respectively 15 nm and ~ 40 - 45 nm). Second, iron compounds other than magnetite or maghemite were found in our samples amongst which some are weakly ferrimagnetic (δ -FeOOH or $5\text{Fe}_2\text{O}_3 \cdot 9\text{H}_2\text{O}$ with a saturation magnetisation of ~ 30 - 40 emu/g_{Fe}, *ie.* three to four times smaller than the one used in our estimation) or antiferromagnetic (e.g. lepidocrocite) hence practically not contributing to the global magnetisation.

The gap between the iron content deduced from the fit and the one from atomic absorption (Table 3.1) decreases on cycling for Lyocell membranes, a result expected from the formation of magnetite at the expense of the more weakly magnetic feroxyhite, observed both by TEM and XRD (*cf.* section 3.3.1).

3. 3. 3. Mössbauer spectroscopy

Mössbauer spectra for BCR were reported by L. Raymond *et al.* (1995), while spectra for Lyocell (Figure 3.8) were measured in the present work.

Spectra for Lyocell samples feature a doublet in all cases, meaning that particles below a critical size (*i.e.* for which the blocking temperature is below room temperature) are always present in significant proportions. The corresponding quadrupole splitting of $\Delta \sim 0.75 \pm 0.02$ mm/s can be associated with the contribution of Fe^{3+} ions in octahedral oxygen coordination. It could thus be attributed to the presence of small magnetite particles, feroxyhite or ferrihydrite (Vanderberghe *et al.*, 1990).

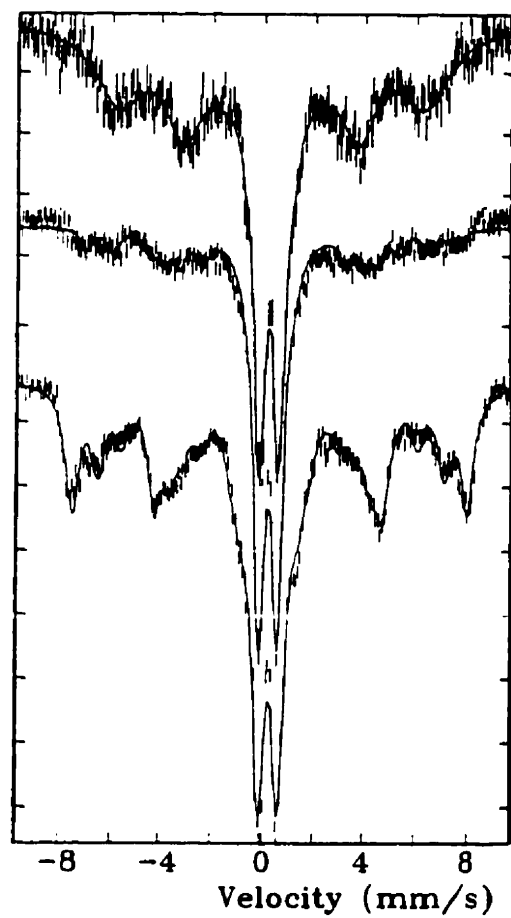


Figure 3. 8. Mössbauer spectra for Lyocell at room temperature. The membranes were *in situ* treated over 1 cycle (uppermost spectrum), 2 cycles and 3 cycles (lowermost spectrum).

The sextet present for the first cycle corresponds to a magnetic hyperfine splitting of $B_{\text{hf}} = 37.3 \pm 0.3$ T that could be assigned to the contribution of ferroxihite (for chemically pure, well crystallised compounds $B_{\text{hf}} = 42.0$ T at room temperature - *cf.* chapter I, table 1.4) found on the corresponding XRD pattern (figure 3.2) and electron micrograph (needles on figure 3.1a). After the second cycle, this sextet is still present, but now superposed on a second sextet with a hyperfine splitting of $B'_{\text{hf}} = 45.2 \pm 0.3$ T. This second sextet becomes predominant after the third cycle, with then a hyperfine splitting of $B'_{\text{hf}} = 48.0 \pm 0.1$ T, and featuring a shape characteristic of maghemite / nonstoichiometric magnetite fine-particle spectra (Martinez *et al.*, 1996).

Similar observations can be made on spectra for bacterial cellulose. For BCR samples (L. Raymond *et al.*, 1995), a doublet is present up to the third cycle, then disappear from the fourth cycle on. The fitting of this doublet was made here, and gave a quadrupole splitting of 0.83 ± 0.02 mm/s, somewhat larger than for Lyocell and attributed to the presence of ferrihydrite (*cf.* chapter I, table 1.4). A magnetic splitting is present on each spectra, showing for the fifth cycle a shape typical of relaxing maghemite particles (*cf.* Lyocell above). The related hyperfine field was 45.5 ± 0.1 T for the third cycle and 46.6 ± 0.1 T for the fifth.

Relaxation processes (*cf.* VSM section) are responsible for a decrease in the hyperfine field with respect to its bulk value:

$$B_{\text{hf}}(V, T) = B_{\text{hf}}(V=\infty, T) \langle \cos\theta \rangle_T, \quad (4)$$

where $B_{\text{hf}}(V=\infty, T)$ corresponds to the hyperfine field in the bulk crystal, at the same temperature,

$\cos\theta$ is the cosine of the angle between the magnetisation direction and the axis of easy magnetisation, and $\langle\cos\theta\rangle_T$ its thermal average near one of the minima (Mørup *et al.*, 1980).

Using the approximation

$$\langle\cos\theta\rangle_T \sim 1 - k_B T/2KV, \quad (5)$$

for $k_B T/KV \ll 1$, a value for KV could be estimated, then using $K \sim 10^4 \text{ J/m}^3$ for magnetite, V could be deduced (Table 3.2). The volumes calculated for the BCR membranes (18 nm after 3 cycles, 20 nm after five cycles) are in good agreement with the respective 10 - 15 nm and ~ 20 nm observed by TEM and the size distribution deduced from the VSM curves, with a maximum at ~ 15 nm. For Lyocell membranes (17 nm after two cycles, 27 nm after three cycles), the agreement is good with the larger sizes observed by TEM (resp. 10 - 15 nm and 20 - 40 nm). The size distribution (Figure 3.7) deduced from the VSM curve includes the two sizes Table 3.2. However, the distribution maximum corresponds to lower sizes (~ 7 nm) in agreement with the persistence of the doublet.

	B (Tesla)	$\langle \cos\theta \rangle$	KV (10^{-20} J)	V (10^{-25} m ³)	D (nm)
Lyocell 2 cycles	45.2 ± 0.3	0.92	2.6	26	17.1 ± 0.4
Lyocell 3 cycles	48.0 ± 0.1	0.98	10.4	104	26.0 ± 0.8
BCR 3 cycles	45.5 ± 0.1	0.93	3.0	30	17.5 ± 0.2
BCR 5 cycles	46.6 ± 0.1	0.95	4.1	41	19.8 ± 0.3

Table 3. 2. Hyperfine fields measured on the Mössbauer spectra for the sextet related to magnetite (the bulk value is 49.1 T at RT - *cf.* chapter I, table 1.4). The average particle volume was deduced using equations (4) and (5). The uncertainty on D was estimated from the uncertainty on the measure of B.

3. 4. Conclusions

The work presented in this chapter attempted to correlate a quantitative physical characterisation and a chemical optimisation. The *in situ* synthesis produced particles of two distinct phases and morphologies: needle-like ferroxihite (δ -FeOOH) after one cycle, concentrated at the membrane surface and spherical magnetite (Fe_3O_4) after several cycles, dispersed within the membrane.

The results obtained, provide direction in order to focus the yield of *in situ* synthesis on superparamagnetic maghemite or magnetite of determined size. The determining role of the microscopic texture of the substrate as well as the effect of its inner space has been examined. Of the two gel cellulosic substrates used, bacterial cellulose and Lyocell, the former gave a higher yield and more uniform loading of ferrites.

Bacterial cellulose gels can be synthesized in a stirred tank to yield a suspension of swollen fibrillar pellets (section 2.1.1; Watanabe and Yamanaka, 1994). In such a configuration, we expect to enhance the efficiency and homogeneity (narrower size distribution) of our synthesis because a membranous surface is absent. Once the *in situ* synthesis is achieved, the fibrillar pellets in suspension can be used as soft beads or can be deposited on a porous substrate for assembling parchment-like nanocomposite membranes.

3. 5. References

- Belford, D.S. and Preston, R.D (1957) *Nature*, **180**, 1081.
- Belford, D.S., Myer, A. And Preston, R.D. (1958) *Nature*, **181**, 1516.
- Bernal, J.D., Dasgupta, D.R., and Mackay, A.L. (1959) *Clay Min. Bull.*, **4**, 15.
- Bowen, L., De Grave, E., Vandenberghe, R. E. (1993) in *Mössbauer spectroscopy applied to magnetism and material science* (G. J. Long, F. Grandjean, eds.). New York: Plenum Press, p. 115.
- Calvert, P. (1994) *Material Science and Engineering*, **C1**, 69.
- Chanzy, H., Dubé, M. and Marchessault, R.H. (1979) *J. Polymer Sci.: Polymer Letters Ed.*, **17**, 219-226.
- Frey-Wyssling, A. (1959) *Die Pflanzliche Zellwand*. Berlin: Springer - Verlag, p. 221.
- Frey-Wyssling, A. and Mühlethaler, K. (1965) in *Ultracellular Plant Cytology*. Amsterdam: Elsevier Publishing Co., p. 309
- Hock, C. W. and Mark, H. (1946) in *Cellulose* (E. Ott. ed.). New York: Interscience Publishers Inc., p. 346.
- Marchessault, R.H., Ricard, S. And Rioux, P. (1992) *Carbohydr. Res.*, **224**, 133.
- Martinez, B., Roig, A., Obradors, X., Molins, E., Rouanet, A. And Monty, C. (1996) *J. Appl. Phys.*, **79(5)**, 2580.
- Mørup, S., Dumesic, J.A. and Topsøe, H. (1980) in *Application of Mössbauer Spectroscopy*, Vol II (R.L. Cohen ed.). New York: Academic Press, p. 1.
- Powers, D.A. (1975) *Magnetic Behaviour of Basic Iron (III) Compounds*, Ph.D. Thesis,

California Institute of Technology, Pasadena, California.

Raymond, L., Revol, J-F., Ryan, D.H. and Marchessault, R.H. (1994) *Chem. Mat.*, **6**, 149.

Raymond, L., Revol, J-F., Ryan, D.H. and Marchessault, R.H. (1995) *Polymer*, **36**, 5035

St. Pierre, T.G., Sipos, P., Chan, P., Chua-anusorn, W., Bauchspiess, K.R., and Webb, J. (1994) in *Nanophase Materials: Synthesis-Properties-Applications* (G. C. Hadjiipanyis and R.W. Siegel eds.). Dordrecht: Kluwer, p. 49.

Taylor, R.M. and Schwertmann, U. (1974) *Clay Minerals*, **10**, 299.

Tamura, Y., Ito, K., and Katsura, T. (1983) *J. Chem. Soc. Dalton Trans.*, 189.

Vanderberghe, R.E., De Grave, E., Landuydt, C. and Bowen, L.H. (1990) *Hyperfine Interactions*, **53**, 175.

Winnik, F.M., Chemistry Dept., Mc Master Univ., Hamilton, Ont., private communication

Watanabe, K., and Yamanaka, S. (1994) *Proceedings of the International Symposium on Fibre Science and Technology*, Yokohama, Japan, p. 445.

Ziolo, R.F. (1984) Xerox Corporation, U.S. Patent 4 474 866.

Ziolo, R.F., Giannelis, E.P., Weinstein, B.A., O'Horo, M.P., Ganguly, B.N., Mehrotra, V., Russell, M.W. and Huffman, D.R. (1992) *Science*, **257**, 219.

CHAPTER IV - MAGNETIC MEMBRANES MADE FROM BACTERIAL CELLULOSE FIBRILLAR SUSPENSIONS

4. 1. Introduction

Bacterial cellulose (BC) can be grown as a microfibrillar suspension or as a gelatinous membrane depending on whether the culture medium is stirred or static (*cf.* section 2.1.1). A BC membrane is inhomogeneous by nature and in the presence of chemically active reagent, will have its surface directly exposed to the reagents with no spatial constraints while access to the membrane interior will depend on diffusion through the surface skin and into the interfibrillar space. The reaction is constrained to a finite volume determined by the inner morphology of the membrane; the space constraint allows a rough particle size control of *in situ* produced ferrites while slow diffusion decreases the oxidation rate favouring dehydrated iron oxides (magnetite and maghemite) precipitation (*cf.* chapter III).

In case of a microfibrillar suspension, the reagents flow homogeneously throughout the reactor, hence only the chemical reaction conditions control the ferrite size. The resulting product is formed under more uniform conditions and can be used to form a homogeneous membrane by means of paper-making techniques *i.e.* drainage of the suspension on a screen.

4. 2. Experimental section

4. 2. 1. Materials

Bacterial cellulose obtained from *Acetobacter Xylinum* prepared in stirred culture and subsequently purified (*cf.* section 2.1.1), was provided by Monsanto (Nutrasweet-Kelco Division, San Diego CA.) under the name *Cellulon*. The “as received” material was a fibrous paste made of 1 mm diameter loose pellet aggregates of BC microfibrils in about 85% water by weight. The paste can be homogenized by treatment with a vigorous ultrasound dispersing apparatus but this procedure was not used in these experiments.

4. 2. 2. *In situ* synthesis

Two experiment sets were run. On a *first set*, two samples were prepared: *sample (i)*, for which the whole synthesis took place in a single container, and *sample (ii)*, for which the adsorption saturation of Fe^{2+} and the reaction with NaOH took place in separate containers, the transfer between the two being made after a centrifugation step discarding the non-adsorbed Fe^{2+} ions.

For both samples, 10 g of the Cellulon paste were dispersed in 100 ml distilled water (DW), bringing the cellulose content to ~ 1.5% of the total weight. Nitrogen bubbling (15 minutes) eliminated dissolved oxygen. 10 g of $\text{FeCl}_2 \cdot 4\text{H}_2\text{O}$ was added to the suspension, raising the Fe^{2+} concentration to 0.5 mol/l. The suspension was aged (30 minutes) only in case of sample

(ii) for thorough adsorption of Fe^{2+} to take place before centrifugation.

NaOH was used to precipitate the ferrous hydroxide. For sample (i), following the adsorption of Fe^{2+} , the OH^- concentration was increased in the suspension to 1 mol/l. For sample (ii), the suspension was first centrifuged, and redispersed in a solution containing 1 mol/l of NaOH. The suspension was thereafter heated up (to 65°C after 30 min for sample (i) - to 75°C after 5 min for sample (ii)), and once this temperature reached, exposed to atmospheric air for approximately 4 hours to be oxidized.

For a *second set*, a standard (std.) treatment was defined as follows. BC suspensions were gently dispersed into DW, the cellulose content being set to 0.5% of the total weight. After bubbling N_2 gas 15 minutes through the suspension to remove dissolved oxygen, crystals of $\text{FeCl}_2 \cdot 4\text{H}_2\text{O}$ were added to bring the initial Fe^{2+} concentration ($[\text{Fe}^{2+}]_{\text{init}}$) to 0.1 mol/l (*ie.* 10 times lower than in the first set). After two hours of aging (instead of 30 minutes in the first set for the centrifuged sample), the sample was centrifuged for a few minutes and redispersed into a solution of NaOH (concentration: 0.1 mol/l). Two hours after, the suspension was brought close to 80°C, exposed to atmospheric air to be oxidized for a period of two hours. The sample was then centrifuged, dispersed into DW, centrifuged a second time, to be finally dispersed in absolute ethanol.

Several samples were treated in conditions where one and only one parameter was changed with respect to its standard value: (i) the $[\text{Fe}^{2+}]_{\text{init}}$ changed from 0.1 mol/l to 0.01 mol/l (low concentration) or 1.0 mol/l (high concentration), (ii) the aging time in $\text{FeCl}_2 \cdot 4\text{H}_2\text{O}$, raised from 2 hours to four hours, (iii) the $[\text{NaOH}]$ changed from 0.1 mol/l to 0.01 mol/l (low

concentration) and 1.0 mol/l (high concentration), (iv) the reaction time in NaOH before oxidation, decreased from 2 hours to 5 minutes, and finally, (v) the oxidation temperature, set once at room temperature (RT) instead of 80°C.

Part of the suspension was poured on a paper filter and dried in an oven at 70°C. The dried sample was a fine sheet easily detached from the filter paper.

***In situ* synthesis procedure for BC microfibrillar suspension**

- A. First set**
1. *Sample preparation* - 1.5% cellulose gently dispersed into nitrogen saturated distilled water (DW/N₂).
 2. *Aging in FeCl₂·4H₂O* - concentration: 0.5 mol/l
- aging time: 5 min for sample (i),
30 min for sample (ii).
 3. *Centrifugation* - no centrifugation for sample (i),
- one centrifugation for sample (ii) for one min (supernatant Fe²⁺ discarded - ~ 1/4 of the total volume remains).
 4. *Reaction with NaOH* - concentration: 1 mol/l,
- reaction time: 30 min for sample (i),
5 min for sample (ii),
- added to the initial suspension for sample (i),
- prepared in a new container in which sample (ii) is redispersed after centrifugation.
 5. *Oxidation* - stirred in presence of atmospheric air,
- temperature: 65 - 75°C,
- oxidation time: 3 to 6 hours.
 6. *Final step* - both samples are stored in absolute ethanol.

- B. Second set**
1. *Sample preparation* - 0.5% cellulose dispersed into DW/N₂.
 2. *Aging in FeCl₃, 4H₂O* - concentrations: 0.01 mol/l,
0.1 mol/l (standard),
1.0 mol/l,
- aging time: 2 hours (std.),
4 hours for one sample otherwise treated under std. cond..
 3. *Centrifugation* - all samples are centrifuged once for one min (supernatant Fe²⁺ discarded - ~ 1/4 of the total volume remains).
 4. *Reaction with NaOH* - concentrations: 0.01 mol/l,
0.1 mol/l (std.),
1.0 mol/l,
- reaction time: 2 hours (std.),
5 min for one sample otherwise treated under std. cond..
- prepared in a new container in which samples are redispersed after centrifugation.
 5. *Oxidation* - stirred in presence of atmospheric air,
- temperature: ~ 80°C (std.),
room temperature for one sample otherwise treated under std. cond..
- oxidation time: 2 hours.
 6. *Final step* - all samples are centrifuged, redispersed in DW/N₂, centrifuged and redispersed in absolute ethanol,
- dried at 70°C on filter paper.

4. 2. 3. X-ray diffraction (XRD)

1 cm² of the dried sample was mounted on a glass slide by the mean of a double sided tape. X-ray diffraction patterns were obtained using a powder diffractometer in reflexion. Cu-K α radiation ($\lambda = 1.5418 \text{ \AA}$) was used. A crystalline size (D) was estimated from the half height broadening (HHB) of the one or two most intense peaks (at diffraction angle 2θ) using the Sherrer-Debye expression

$$\text{HHB} = 54 \lambda / D \cos (2\theta/2).$$

4. 2. 4. Transmission Electron Microscopy (TEM)

A drop of each ethanol suspension of *in situ* product was deposited and allowed to dry on a carbon coated copper grid. A Philips CM 200 transmission electron microscope (TEM) operated at 200 kV was used for imaging by diffraction contrast and for selected area (SA) diffraction.

4. 2. 5. Magnetic characterisation

The magnetic properties of the *in situ*, treated materials after air drying were examined by vibrating sample magnetometry (VMS). Approximately 20 mg of the dried membrane was rolled and vibrated perpendicular to a magnetic field of up to 1.5 T. The response of the material was

plotted as a function of the applied field to yield a magnetization curve.

4. 3. Results and discussion

4. 3. 1. Macroscopic aspect

The colours taken by the different samples throughout the synthesis process are summarized in table 4. 1; the final colours (figure 4. 1) correspond to varying mixtures of Fe_3O_4 (black / dark brown) / FeOOH (yellow / rusty).

Solutions after oxidation were usually strongly alkaline ($\text{pH} > 12$) except for treatments where $[\text{NaOH}]$ was low or $[\text{Fe}^{2+}]_{\text{init}}$ was high, the pH being then slightly acid ($\sim 5-6$).

On drying, the suspension gave tough sheets, easily removed from the paper filter, except the one treated with high NaOH concentration which yielded a very brittle sheet on drying.

Figure 4. 1. Colour taken by the different samples after the whole *in situ* process (second set).

Air dried bacterial cellulose suspension *in situ* treated

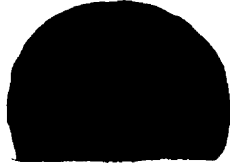
high [Fe²⁺] 2 hours



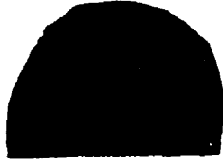
int. [Fe²⁺] 2 hours



int. [Fe²⁺] 4 hours



low [Fe²⁺] 2 hours



Air dried bacterial cellulose suspension *in situ* treated

high [NaOH]



int. [NaOH]

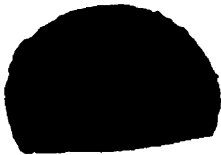


low [NaOH]



Air dried bacterial cellulose suspension *in situ* treated

5 minutes in NaOH / oxidation at 80°C



2 hours in NaOH / oxidation at 80°C



2 hours in NaOH / oxidation at RT



Air dried bacterial cellulose suspension *in situ* treated

high [NaOH] 2 hours



int. [NaOH] 2 hours



int. [NaOH] 5 minutes



First set	1.	2.	3.	4.	5.	6.
Sample (i)	white	pale green	-	whitish-green pH ~ 8	grey pH ~ 6	black
Sample (ii)	white	pale green pH ~ 4	-	dark-green pH > 12	dark grey	black
second set	1.	2.	3.	4.	5.	6.
high [Fe ²⁺] _{int}	white	pale green	pale yellow	dark blue-grey	dark grey	dark brown pH ~ 5
int. [Fe ²⁺] _{int}	"	"	"	cold-grey	-	brown pH > 12
low [Fe ²⁺] _{int}	"	"	"	worm-grey	-	yellow pH > 12
4 hrs in Fe ²⁺	"	"	"	dark green	very dark grey	black pH > 12
high [OH ⁻]	"	"	"	yellowish-grey pH > 12	dark grey	brown
int. [OH ⁻]	"	"	"	grey pH > 12	"	dark brown
low [OH ⁻]	"	"	"	blue-grey pH ~ 6	"	dark brown
5 mn in NaOH	"	"	"	-	-	pale brown
oxidation at RT	"	"	"	-	brown	rusty brown

Table 4. 1. Colours observed during *in situ* process. Steps are: 1. sample in DW; 2. aging in FeCl₂·4H₂O; 3. centrifugation; 4. reaction with NaOH; 5. oxidation; 6. end. Presumed colour correspondence: white = cellulose; pale green = Fe(OH)₂ + green rust; grey = Fe(OH)₂ + Fe₃O₄; blue grey = green rust + Fe₃O₄; pale yellow = Fe(OH)₂ + FeOOH; yellow / rusty = FeOOH; dark brown / black = Fe₃O₄.

4. 3. 2. X-ray diffraction

Three characteristic peaks are systematically present at low angles in all powder diagrams, including the one for a non-treated (blank) cellulose membrane (not presented). These peaks are attributed to the presence of crystalline cellulose I, corresponding from lower to higher 2θ to the (110), (1 $\bar{1}$ 0) and (010) reflexions. The peak of highest intensity, corresponding to $2\theta \sim 22.8^\circ$, was chosen as a reference for the intensity (I_{ref}) of all diffraction peaks. For the first set (figure 4.2), a subspectra including narrow peaks is attributed to the presence of NaCl.

Peaks associated with magnetite are clearly defined for this set. The half-height broadening (HHB) indicates crystalline sizes of ~ 30 nm to 40 nm (sample (i)) and ~ 90 nm to 300 nm (sample (ii)).

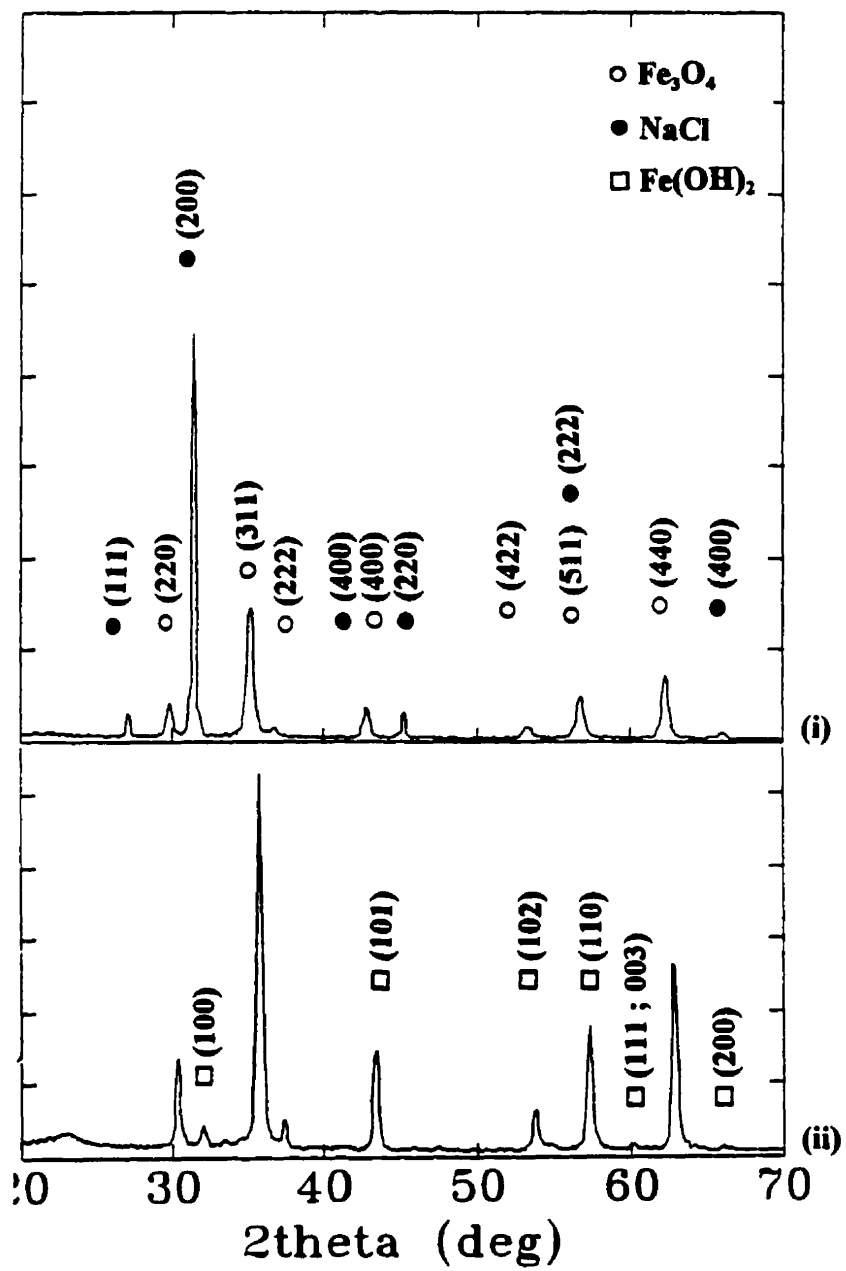
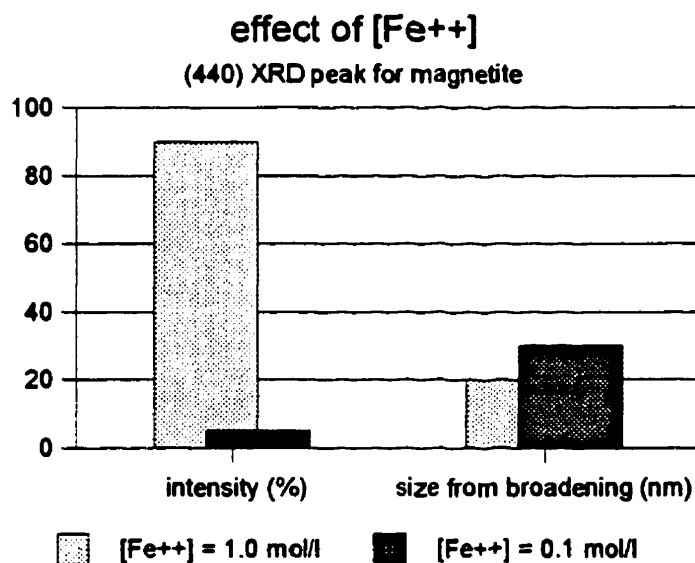


Figure 4. 2. XRD patterns for the first set; (i) non-centrifuged, (ii) centrifuged.

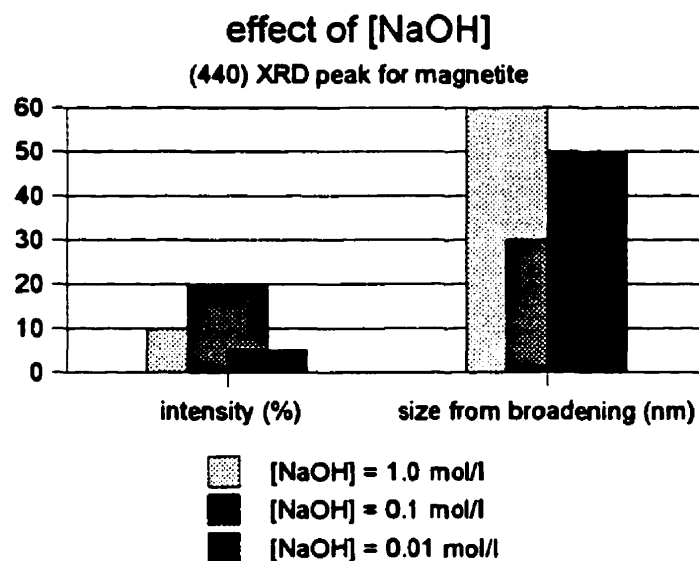
For the second set, peaks of various intensity associated with the presence of magnetite can be distinguished for all treated sample diagrams (figure 4.3), except for the one oxidized at RT.

The most intense peaks related to magnetite were measured for the sample treated with the highest $[Fe^{2+}]_{init}$ (1.0 mol/l) - $I(440)/I_{reference} \sim 90\%$ - and for the sample aged for four hours instead of two in ferrous chloride - $I(440)/I_{reference} \sim 70\%$. The crystalline sizes calculated from the HHB were respectively ~ 20 nm and 50 nm in the (440) direction.

The effect of the initial ferrous ion concentration (for $[Fe^{2+}]_{init} = 0.1$ mol/l and 1.0 mol/l) on the (440) XRD peak for magnetite is summarized opposite (for low $[Fe^{2+}]_{init}$, only the cellulosic substrate contributes significantly to the spectra).



Ageing the sample five minutes instead of two hours in NaOH before the heating and oxidation phase, did not have any significant incidence on the XRD spectra, while the NaOH concentration was found to affect both the magnetite crystalline size and concentration. The corresponding peaks were broader (indicating smaller crystalline size) and at least to two times higher for an intermediate [NaOH] (0.1 mol/l) with respect to extreme [NaOH]'s.



Peaks associated with the presence of feroxyhite generally appear on diagrams measured for samples treated with intermediate (NaOH and $\text{FeCl}_2 \cdot 4\text{H}_2\text{O}$) concentrations (0.1 mol/l) and with high [NaOH] (1.0 mol/l). When the $[\text{Fe}^{2+}]_{\text{init}}$ is set to 1.0 mol/l, crystals of lepidocrocite seem to replace the feroxyhite.

Presence of other compounds such as NaOH / $\text{NaOH} \cdot \text{H}_2\text{O}$ (oxidation at room temperature or high NaOH concentration) was also deduced from the diffraction diagrams.

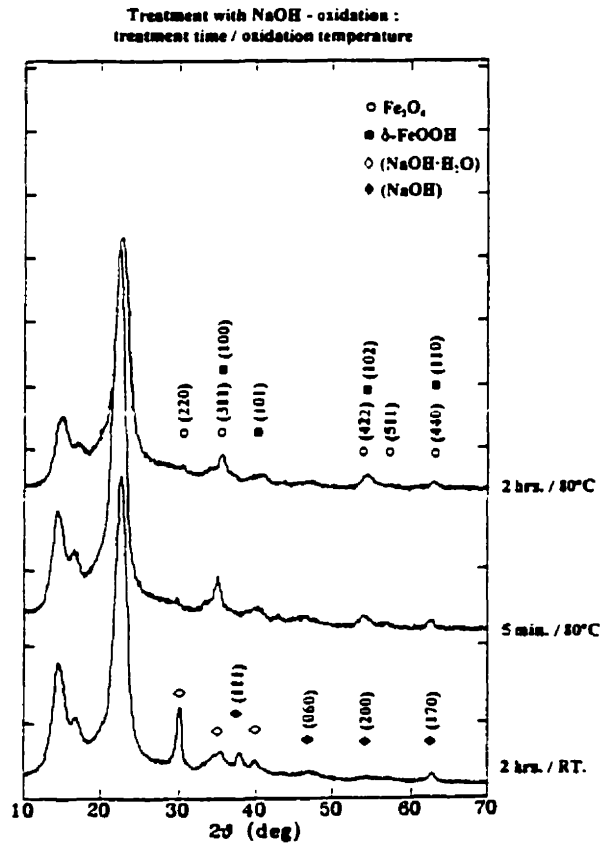
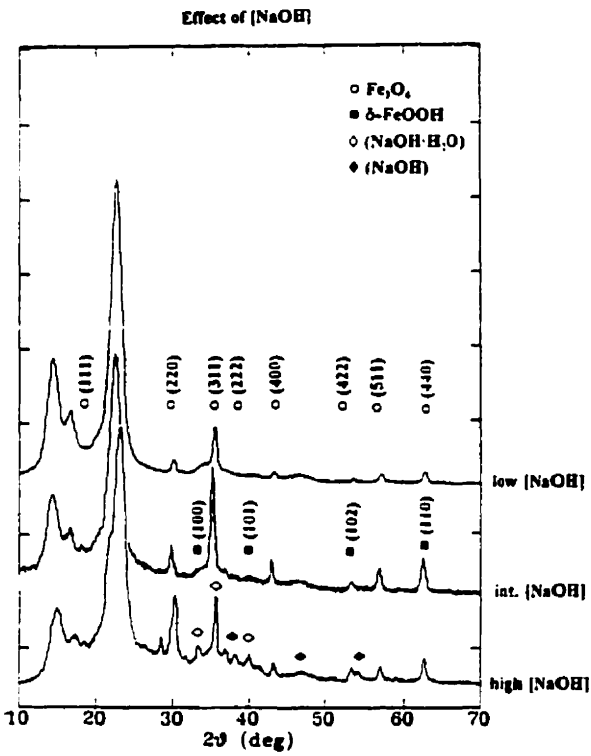
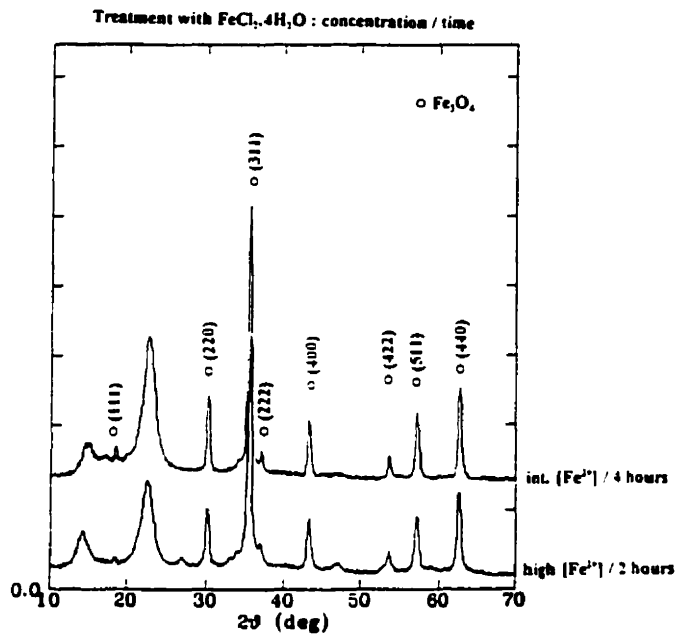
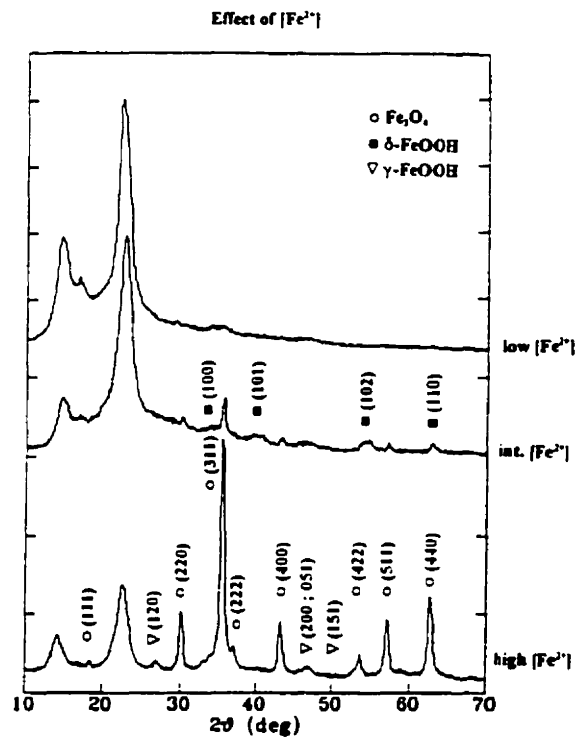


Figure 4. 3. XRD pattern for the second set.

4. 3. 3. Transmission Electron Microscopy

First set

Transmission electron micrographs for the first set, show the presence inside the samples (i) (figure 4.4), of hexagonal plates on the edge of which, needles (~ 100 to 200 nm long) are aligned. Low contrasted ragged plates apparently made of lath stuck side by side are also seen. Diffraction patterns for these complexes reveal the presence of lepidocrocite. On the other hand, polyhedral particles (generally cubic) where dimensions varied from 50 to 100 nm were discernible; their diffraction pattern correspond to magnetite.

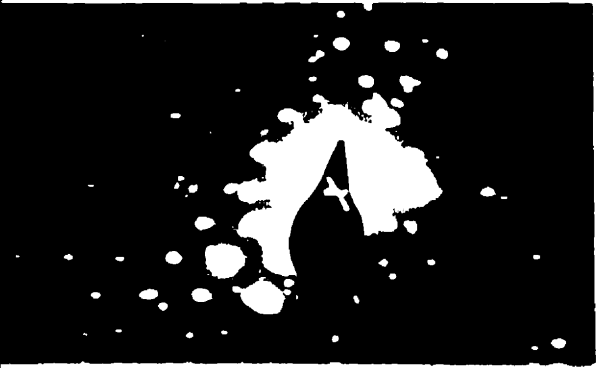
Micrographs of sample (ii) (figure 4.5), show the presence of larger polyhedral particles (~ 200 nm to 500 nm in size) along with needles ranging from ~ 50 nm to ~ 250 nm, hexagonal plates (~ 100 to 500 nm) and very fine seed particles (~ 10 nm), observable along the fibrillar network. The square particles give single crystal diffraction patterns associated with magnetite.

In this first set of experiments, the centrifugation resulted in a decrease of the $[\text{Fe}^{2+}]$ concentration between the non-centrifuged sample (i) and the centrifuged sample (ii) by approximately a factor of 4, resulting in an increase of $[\text{OH}^-]_{\text{ex}} = [\text{NaOH}] - 2[\text{Fe}^{2+}]$ from ~ 0 to 0.75 mol/l. The resulting magnetite particles were found respectively to be ~ 50 nm (sample (i)) and ~ 200 nm (sample (ii)) in size. These results are to be compared with the works by Sugimoto *et al.* (1980) on similar treatments which yielded at low $[\text{OH}^-]_{\text{ex}}$ very small particles (~ 10 nm) and at higher $[\text{OH}^-]_{\text{ex}}$ (0.3 mol/l) larger cubic particles (~ 100 nm) grown by direct crystallisation.

Figure 4. 4. Transmission electron micrograph for the first set, sample (i).



Figure 4. 5. (a) transmission electron micrograph for the first set, sample (ii). (b) diffraction pattern of a square particle. (c) simulated diffraction pattern for a magnetite single crystal.



(b)

MAGNETITE 222 422 511
 111 311
 0 200 400

(c)

Second set

In the second set, *seed particles* are generally observed with a mean size of 10 nm, except in case of low $[\text{Fe}^{2+}]_{\text{init}}$ (< 10 nm - figure 4.6) and high $[\text{Fe}^{2+}]_{\text{init}}$ (~ 30 nm - figure 4.7). These particles are inclined to aggregate into lumps of varying compactness (usually 100 - 500 nm in size - ~ 40 nm for low $[\text{Fe}^{2+}]_{\text{init}}$). Samples having the darkest hue when observed with the naked eye (dark brown to black) are found to be the host of *polyhedral particles* (50 - 100 nm in dimension). These two species (seed and polyhedral particles) gave diffraction patterns corresponding to *magnetite*.

Needles (ellipsoidal longitudinal section, ~ 100 nm x 20 nm in size) as well as *rods* (rectangular longitudinal section, ~ 100 nm x 50 nm in size) are also present in various proportions, eventually simultaneously. These particles were identified by electron diffraction as *feroxyhite*.

Platelets of round shapes, apparently becoming hexagonal as they grew in size, are observable with dimensions ~ 50 - 200 nm. Their electron diffraction pattern was found compatible with *feroxyhite* diffraction data (figure 4.12). Rods may be tilted platelets and indeed both were found predominant simultaneously in samples for which the XRD peaks associated with *feroxyhite* were of the highest intensities.

Translucid laths 100 to 400 nm in size (case of high $[\text{Fe}^{2+}]_{\text{init}}$) and dark lumps ~ 400 nm in size (case of low $[\text{Fe}^{2+}]_{\text{init}} = 0.01 \text{ mol/l}$) were identified by electron diffraction as *lepidocrocite* (figure 4.6). Finally, *spotted translucid plates* ~ 200 nm in size gave diffraction patterns compatible with *akaganeite* crystalline parameters (figure 4.13).

The initial concentration in Fe^{2+} beside controlling the mean size of the seed particles (growing from below 10 nm to about 30 nm), also affects their size distribution, broad for extreme concentrations (figure 4.6 and figure 4.8), while relatively narrow for intermediate concentration (figure 4.7). The polyhedral particles were only observed for the two highest concentrations. Although the larger magnetite particles are seen at high concentration, their broad distribution may be responsible for the slightly lower size deduced from the broadening of the corresponding XRD peaks (*cf.* section 4.3.2).

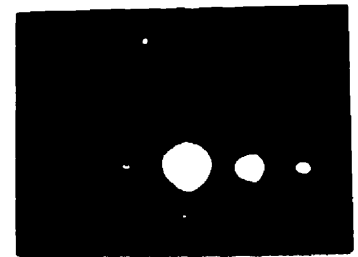
The influence of $[\text{NaOH}]$ can be summarized as follows. $[\text{NaOH}] = 0.01 \text{ mol/l}$ (figure 4.10) yields seed particles similar to the $[\text{Fe}^{2+}]_{\text{init}} = 1.0 \text{ mol/l}$ case, with however lower median size (15 nm instead of 30 nm) and less aggregation. No other species were observed. $[\text{NaOH}] = 0.1 \text{ mol/l}$ product (figure 4.11) is similar to $[\text{Fe}^{2+}]_{\text{init}} = 0.1 \text{ mol/l}$ (*cf.* above). At $[\text{NaOH}] = 1.0 \text{ mol/l}$ (figure 4.12), platelets / rods and spotted translucent plates supplant both polyhedra and needles. The polyhedra are $\sim 200 \text{ nm}$ in size while they were $\sim 50 \text{ nm}$ for $[\text{NaOH}] = 0.1 \text{ mol/l}$, while the respective $[\text{OH}^-]_{\text{ss}}$ are 0.8 mol/l and $\sim 0 \text{ mol/l}$, still in agreement with Sugimoto *et al.* (1980) results (*cf.* discussion for the first set). The amount of iron introduced in the synthesis process is found to determine the size and concentration of the resulting species while the kind of phases in presence rather depends on the ratio $[\text{NaOH}] / [\text{Fe}^{2+}]_{\text{init}}$. These observations are consistent with previous results on oxidation of $\text{Fe}(\text{OH})_2$ precipitates as a function of the ratio $R = 2[\text{NaOH}] / [\text{Fe}^{2+}]_{\text{init}}$ (Kiyama, 1974 - *cf.* next section).

Oxidation at room temperature gave similar results than low $[\text{NaOH}]$, with however less aggregation and some needles present. Finally the sample treated four hours in ferrous chloride (figure 4.8) contains cubic particles of two homogeneous sizes, the larger particles ($\sim 70 \text{ nm}$)

being gathered, the smaller (~20 nm) scattered.

The micrograph figure 4.16 shows a treated suspension at low magnification: the location of the grown ferrites along the fibril further demonstrates their function as nucleation site.

Figure 4. 6. (a) transmission electron micrograph for the second set, low $[\text{Fe}^{2+}]$. (b) the diffraction pattern of the dark lump on the top-left corner (arrow on (a)). (c) simulated diffraction pattern for a lepidocrocite single crystal.



(b)

LEPIDOCROCITE

431	231	31	231	431
400	200	0	200	400
431	231	31	231	431

(c)

Figure 4. 7. Transmission electron micrograph for the second set; intermediate [Fe²⁺].



38 8X 1401

Figure 4. 8. Transmission electron micrograph for the second set; high $[\text{Fe}^{2+}]$.



00000000
00 00

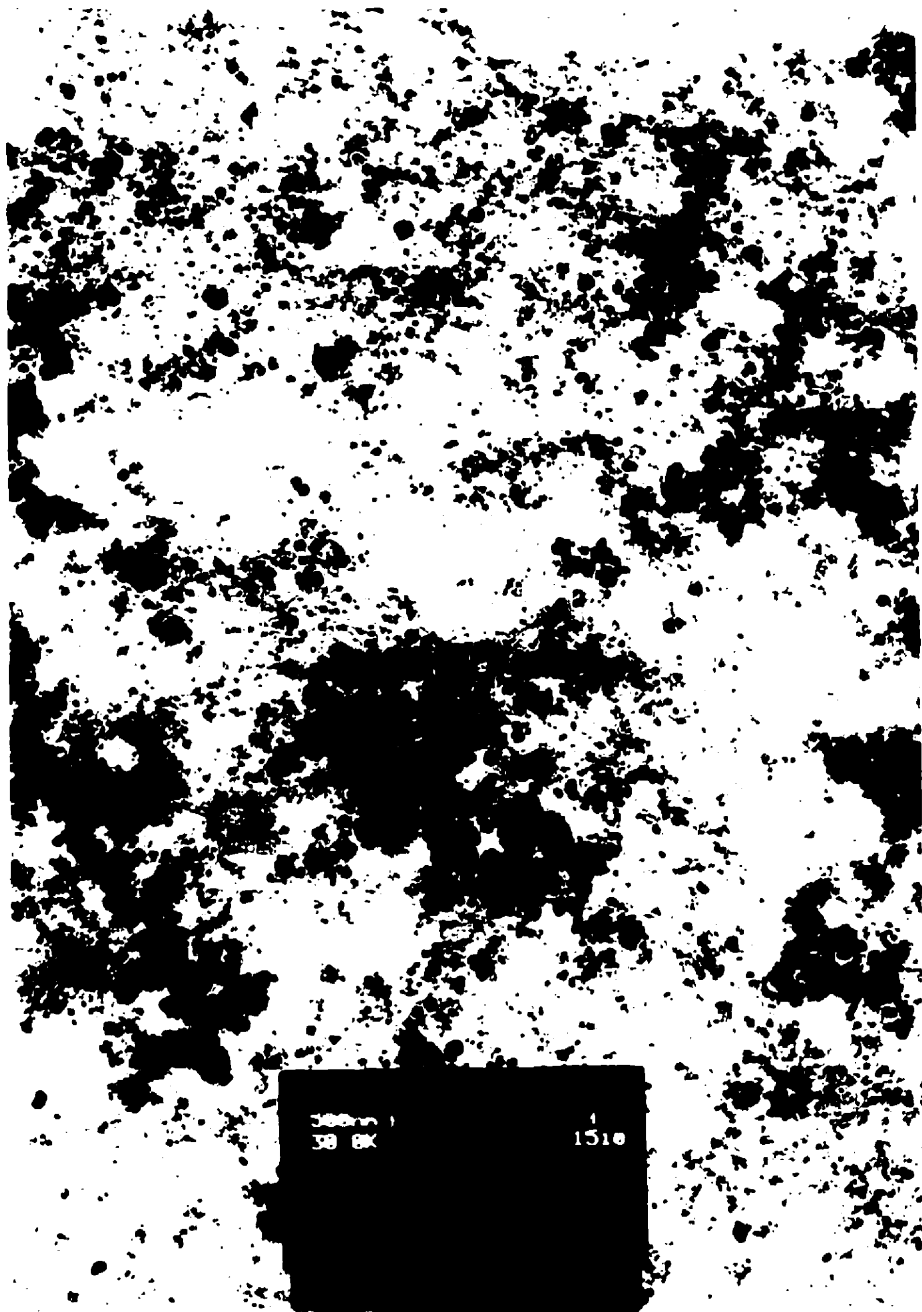
1457

Figure 4. 9. Transmission electron micrograph for the second set; intermediate $[\text{Fe}^{2+}]$, treaded in ferrous chloride extended from two to four hours.



22 BK 1329

Figure 4. 10. Transmission electron micrograph for the second set; low [NaOH].



366m)
38 BX

1510

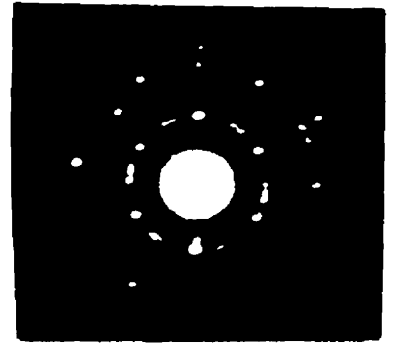
Figure 4. 11. Transmission electron micrograph for the second set; intermediate [NaOH].



0000 in
30 PK

1516

Figure 4. 12. (a) transmission electron micrograph for the second set, high [NaOH]. (b) diffraction pattern of a platelet (arrow on (a)). (c) simulated diffraction pattern for a ferroxhite single crystal.



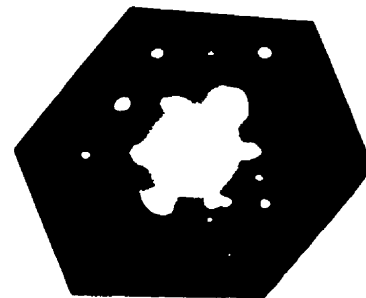
(b)

FERROXYHITE

		130	330
		20	220
	110	110	310
200	0	200	
310	110	110	
	220	20	
330	130		

(c)

Figure 4. 13. (a) transmission electron micrograph for the second set, two hours treatment in NaOH, oxidation at 80°C. (b) diffraction pattern of a translucent plate (arrow on (a)). (c) simulated diffraction pattern for an akaganeite single crystal.



(b)

AKAGANEITE

921 521 121 321 721

800 400 0 400 800

721 321 121 521 921

(c)

Figure 4. 14. Transmission electron micrograph for the second set; five minutes treatment in NaOH, oxidation at 80°C.



38 BK 1426

Figure 4. 15. Transmission electron micrograph for the second set; two hours treatment in NaOH, oxidation at room temperature.



Sample
ID

15.06

Figure 4. 16. Transmission electron micrograph of a treated suspension. The grown ferrites are clearly localized along the cellulose fibrils.



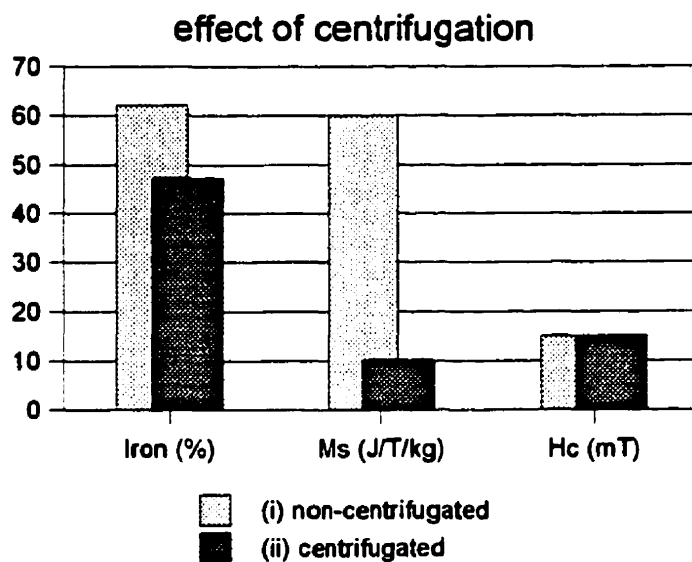
4/10
78x

1464

4. 3. 4. Vibrating Sample Magnetometry (VSM)

The magnetization was measured as a function of an applied magnetic field in the range $|H_{app}| < 1.5$ T (figure 4.17). The magnetization curve measured for commercial magnetite (made of elongated particles of approximately 250 nm in length), saturates at 80 J/T/kg (lower than the 84 J/T/Kg reported table 4.2 for however larger particles). The curve measured for sample (i) features a similar shape (as determined by the initial susceptibility at low fields, and the slope at the approach to saturation at high fields) however saturating at 60 J/T/kg. The coercivity was also lower, possibly owing to a lower shape anisotropy.

The magnetization curve measured for sample (ii), features a lower initial susceptibility along with a higher slope at the approach to saturation, indicating the presence of lower magnetic moments. However, the magnetite particles were found to be larger than sample (i) both by XRD and TEM. The iron content of sample (ii), was measured by atomic absorption as 47.52%. If all iron was present as bulk magnetite, the measured saturation magnetization (10.2 J/T/kg) would correspond to an iron content of only 10%. Therefore, aside from its contribution to the formation of large cubic magnetite particles, iron in sample (ii) must be present in significant proportion in the form of compound of either smaller sizes or lower saturation magnetization (such as feroxyhite and ferrihydrite). Remanence

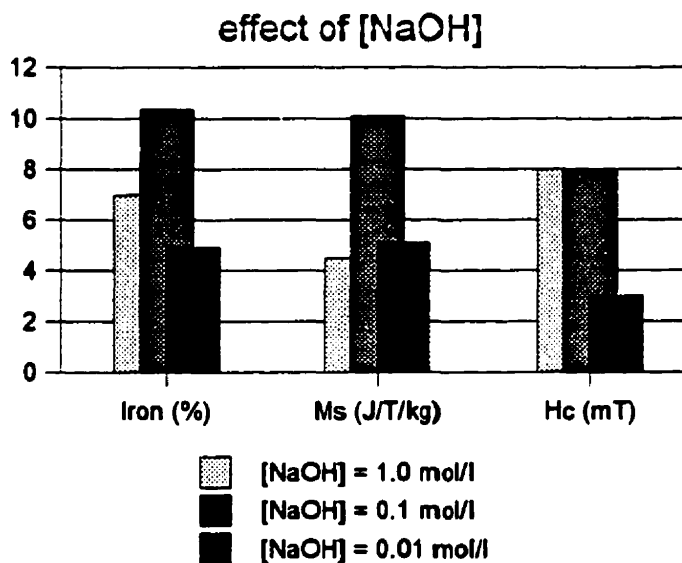
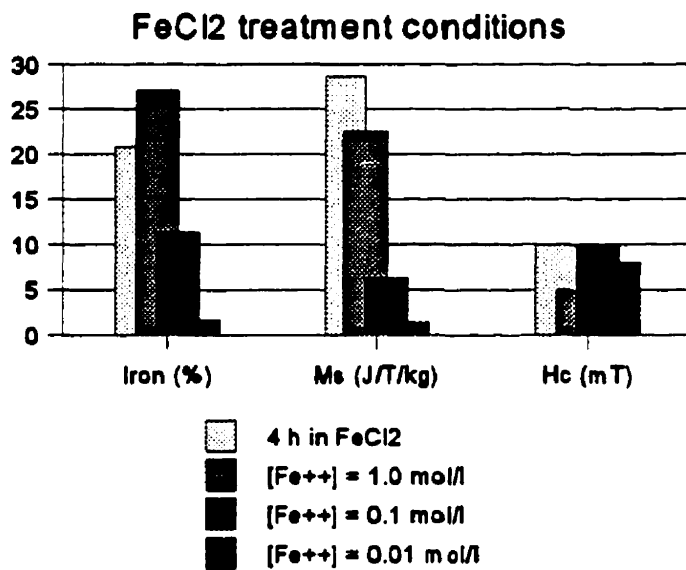


and coercivity were found similar for the two samples.

The magnetization measured for the second set ranges from 28.7 J/T/kg (four hour aging in FeCl₂·4H₂O) and 22.5 J/T/kg (high [Fe²⁺]_{init}) to 2.08 J/T/kg (oxidation at RT) and 1.4 J/T/kg (low [Fe²⁺]_{init}).

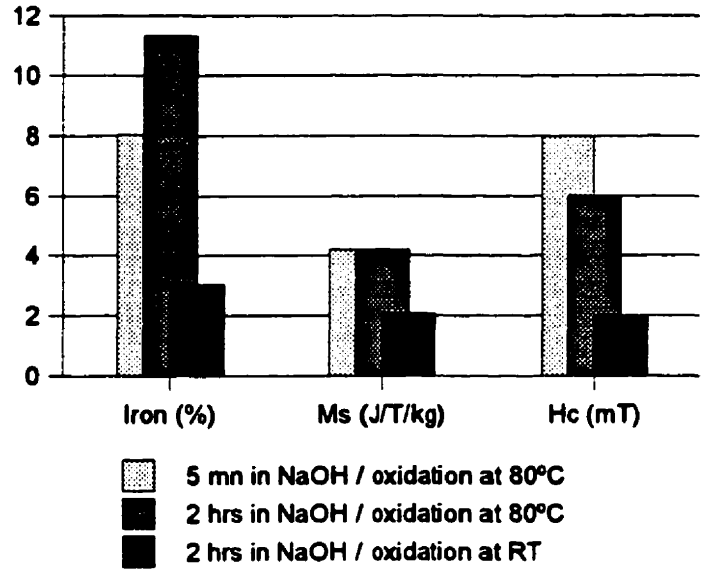
Increasing the ferrous ion concentration by a factor of ten ([Fe²⁺]_{init} = 0.01 - 0.1 - 1 mol/l) leads to a factor four increase in the saturation magnetization (M_s = 1.4 - 6.2 - 22.5 J/T/kg). Doubling the aging time in FeCl₂ approximately doubles the iron content and multiply the saturation magnetization by ~ 5 with no significant effect on the coercivity.

When the variable is the NaOH concentration, the highest saturation magnetization along with the lowest remanence and coercivity are found for the intermediate concentration.



Increasing the reaction time in NaOH

before oxidation increases the iron content with no effect on the saturation magnetization. This additional iron may in consequence be involved in non-magnetic compounds. A slight decrease in coercivity for a long exposure to NaOH is attributed to a restricted agglomeration hence magnetic interaction between the seed particles.



Kiyama (1974) defines the molar ratio $R = 2[\text{OH}^-] / [\text{Fe}^{2+}]$. This ratio has been varied in our second set of experiments by changing either the ferrous ion or hydroxyl ion concentrations. For $R \sim 20$, $R \sim 2$ and $R \sim .2$, the synthesis proceeded respectively through the formation of mixtures of $\text{Fe}(\text{OH})_2 / \text{FeOOH} / \text{Fe}_3\text{O}_4$, $\text{Fe}(\text{OH})_2 / \text{Fe}_3\text{O}_4$ and green rust / Fe_3O_4 whose oxidation resulted in mixtures of $\text{Fe}_3\text{O}_4 / \text{FeOOH}$ in varying proportions. The magnetite preponderance is favoured at the lowest R with the increase of the inherent magnetization saturation. Longer aging times in FeCl_2 before precipitation by NaOH also favoured the magnetite preponderance and increased the saturation magnetization, indicating the slow diffusion / adsorption rate of the ferrous ions in the cellulose fibrillar network. Increasing the supplied amount of iron ($[\text{Fe}^{2+}]_{\text{init}} = 0.1 \text{ mol/l}$ to 1.0 mol/l) at constant R (~ 20) was also found to increase both the iron content (5% to 27% respectively) and saturation magnetization (10 J/T/kg to 22 J/T/kg respectively).

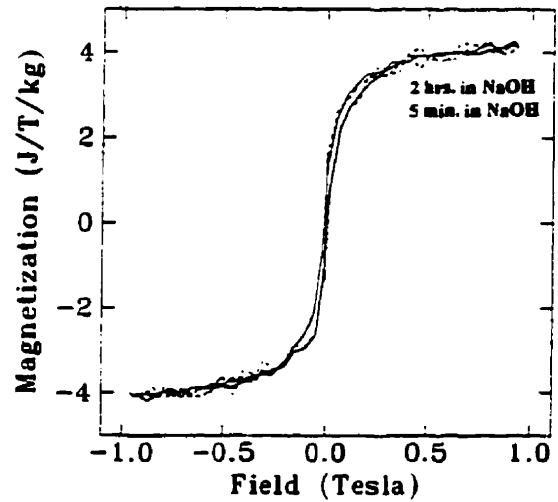
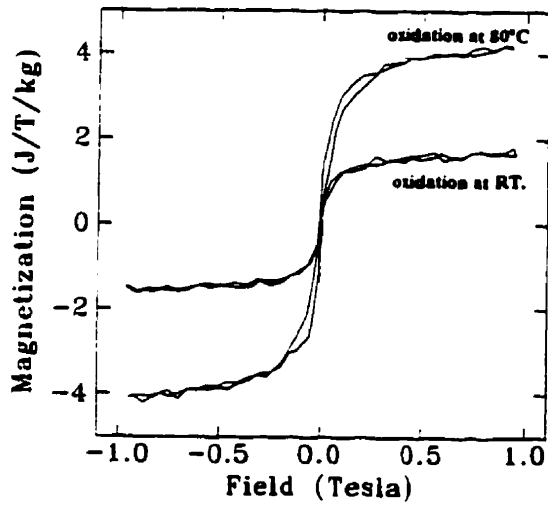
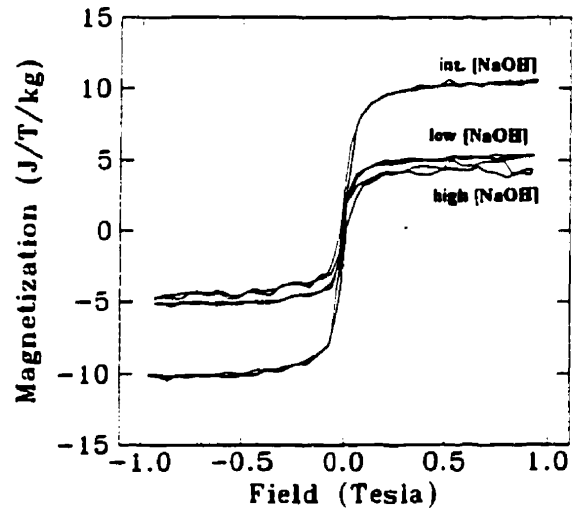
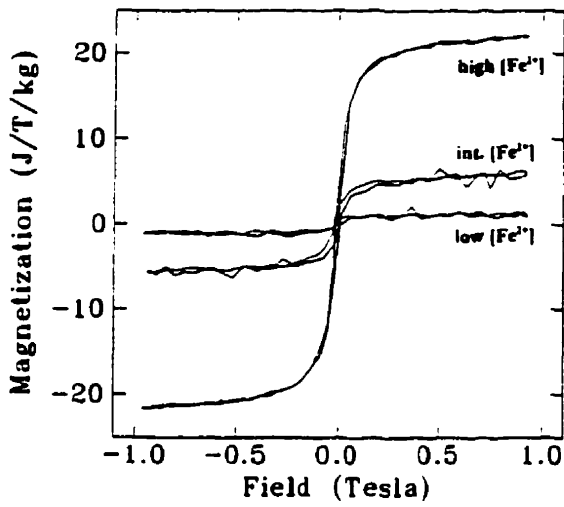
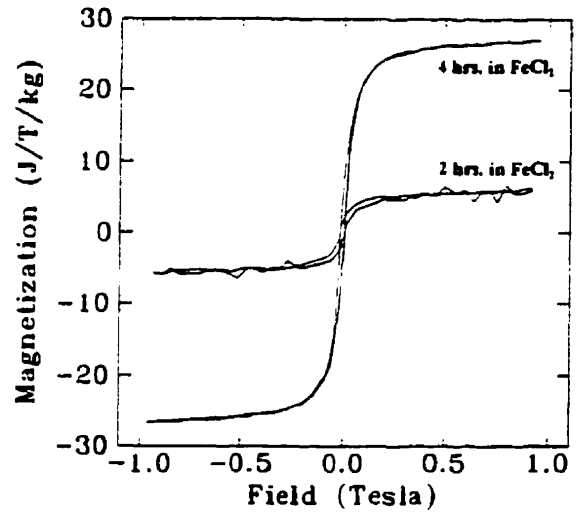
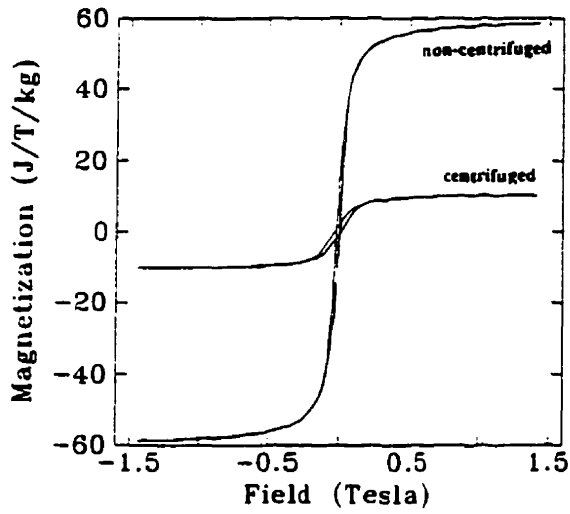


Figure 4. 17. Magnetisation curves measured by VSM.

4. 4. Conclusion

This study was dedicated to the synthesis of iron oxides in bacterial cellulose suspensions with the purpose of creating uniform magnetic cellulosic membranes. The iron oxides were produced by aerial oxidation of $\text{Fe}(\text{OH})_2$ / green rust precipitated from ferrous chloride by NaOH, under different conditions. Centrifugation was used to discard the non adsorbed ferrous ions and concentrate the ferrous hydroxide precipitation (and subsequent ferrite crystallisation) within the substrate.

Both magnetite content and saturation magnetization increased for lower $R (= 2[\text{OH}^-] / [\text{Fe}^{2+}])$ and longer time in FeCl_2 . The concentration of hydroxyl ions in solution was found to affect the size and morphology of the magnetite particles. Furthermore, increasing the reaction time with NaOH before oxidation, from 5 minutes to 2 hours, first restricted the primary particle aggregation, secondly increased the iron content with limited effect on the magnetic properties. The oxidation temperature and rate must be respectively high and slow (aerial oxidation instead of reaction with peroxide) to allow dehydration of the ferrous hydroxide or the green rust precipitate before oxidation, a necessary condition for magnetite to supplant FeOOH .

Using bacterial cellulose in the form of a fibrillar suspension rather than a gel membrane as substrate for the *in situ* synthesis improved the particle distribution homogeneity (eventually further improved by a preliminary treatment promoting the BC pellets' disentanglement). Thus, homogeneous magnetic membranes containing magnetite particles both monodisperse and insignificantly contaminated by other iron compounds could be produced. However, the magnetic behaviour of such particles as due to their excessive size was ferrimagnetic rather than superparamagnetic at RT.

CONCLUSION

The object of this thesis was a better understanding of the mechanisms implied in the *in situ* synthesis of ferrites within a cellulosic substrate and the extensive characterization of the product of this synthesis. In fact, conditions for the production of magnetic cellulosic membranes *homogeneously* and *significantly* loaded with *magnetite* particles of *controlled dimension* has been achieved.

The experimental part of this study was realised in two stages: first the *in situ* synthesis of the magnetic membranes, secondly their physical characterization. The experimental parameters available in the synthesis stage were of two order: *physical* parameters related to the *specific morphology* and the *swollen state* of the different substrates; *chemical* parameters such as concentration of the various reagents, *time of reaction* (diffusion, adsorption, precipitation, oxidation...), *agent* and *temperature of oxidation*. The techniques used in the characterization stage were x-ray diffraction, transmission electron microscopy, vibrating sample magnetometry and Mössbauer spectroscopy.

The role played by the cellulose fibrils as a site for the nucleation of the growing ferrites was demonstrated: the ferrous ions diffuse within the fibrillar network where they are adsorbed on the cellulose hydroxyl groups. The diffusion rate determined by the swollen state, as well as the hydroxyl group density are consequently determinant for the synthesis product.

The surface effect was clearly established; it is responsible for inhomogeneity of two kinds: on the one hand, inhomogeneity in size and concentration for particles of the same nature,

on the other hand, inhomogeneity in phase, corresponding to different degrees of dehydration, resulting from different oxidation rates. Realising several cycles of treatment (provision of fresh ferrous ions followed by a new oxidation) on the same substrate, reduces these inhomogeneities, promoting simultaneously the penetration and dehydration of the produced ferrites.

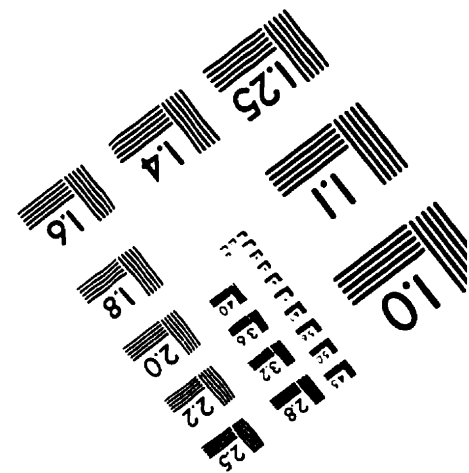
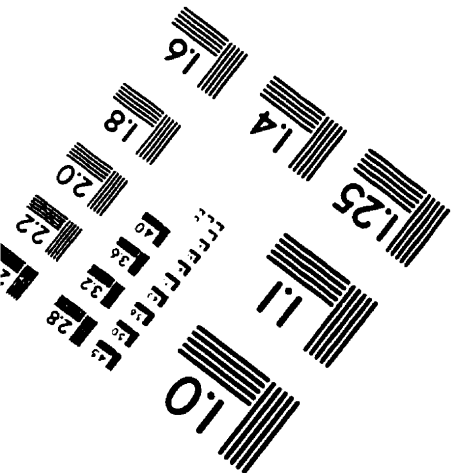
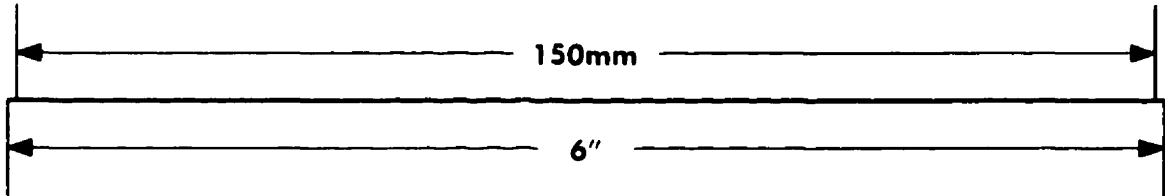
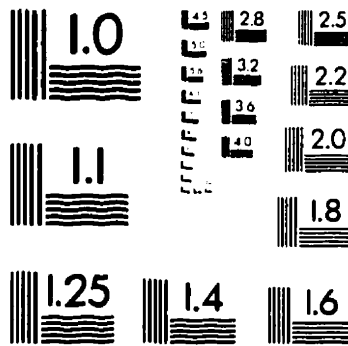
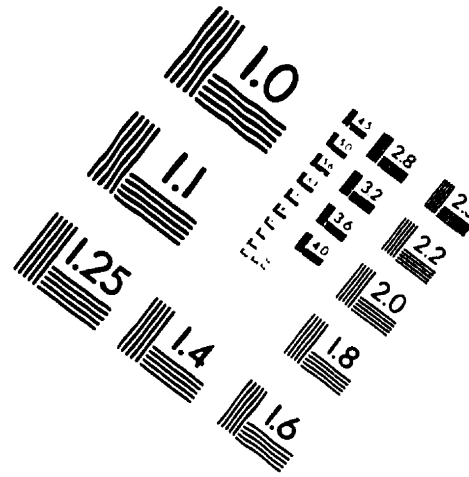
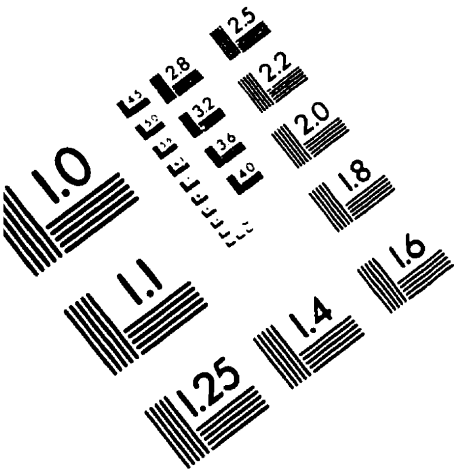
Four parameters were considered for the *in situ* synthesis optimisation. The *homogeneity* issue was addressed by using a substrate in the form of a fibrillar suspension, subsequently cast and assembled as a membrane. The goal was achieved however with loss of the size control provided by the membranous substrates by the space constraint.

This space constraint exerts a direct control on the *ferrite dimensions* provided that the confining space is small enough. In the case of excessively large or even free space, the iron concentration (eventually controlled by the diffusion rate) conjugated with the hydroxyl group density, becomes the determinant factor. The effect of the excess concentration of hydroxyl ions in solution on the particle size has furthermore being confirmed.

The *quantitative* optimisation of the ferrite loading requires in case of constrained space a sufficient swelling state, and is in the general case function of the ferrous ions concentration and adsorption time.

Finally, in order to focus the synthesis on the *exclusive production of magnetite*, the overriding of the oxidation slowness together with the requirement of high temperature has been further confirmed.

IMAGE EVALUATION TEST TARGET (QA-3)



APPLIED IMAGE, Inc
 1653 East Main Street
 Rochester, NY 14609 USA
 Phone: 716/482-0300
 Fax: 716/288-5989

© 1993, Applied Image, Inc., All Rights Reserved